UNIVERSITY OF CALIFORNIA
RIVERSIDE

Understanding Local-Scale Fault Interaction Through Seismological Observation and Numerical Earthquake Simulation

A Dissertation submitted in partial satisfaction
of the requirements for the degree of

Doctor of Philosophy

in

Geological Sciences

by

Kayla Ann Kroll

March 2016

Dissertation Committee:

Dr. James H. Dieterich, Chairperson
Dr. Keith B. Richards-Dinger
Dr. Elizabeth S. Cochran

The Dissertation of Kayla Ann Kroll is approved:

Committee Chairperson

University of California, Riverside

Acknowledgments

There are no words to describe how deeply indebted I am to the wonderful group of advisors and mentors I have had on this journey. I have been given the most wonderful opportunity to work with some of the most renowned scientists in our field, who have all contributed any success I will have, but more importantly, who have all become my friends and colleagues, who've always treated me like an equal collaborator rather than just a student. I have truly had a very unique graduate student experience.

First, I am very grateful to Jim Dieterich, who has never treated me as anything but a colleague, despite the great disparity between us. Jim, thank you for agreeing to advise another student just before your retirement and teaching me how to be a thorough and meticulous investigator. I have always appreciated your enthusiasm for science, passion for discovery, and willingness to explore uncharted waters. The stories of your adventures aren't too bad either. Thank you for guiding me through this obstacle course called graduate school and trying to show me the world through your eyes. Finally, thank you for being my friend, someone I could count on (especially when I couldn't walk!)

There is one person who has single-handedly taught me more than any other person, class, or textbook. Anybody who has worked with him knows that Keith Richards-Dinger is one of the most brilliant people they have ever met. Keith, I cant imagine where I would be if it hadn't been for your constant support and willingness to help (with all things, related to science or not). You have shaped that way I conduct research, explain ideas, and honestly, how I think about the world. Not only are you beyond proficient at everything you attempt, but you are level-headed and open-minded. Thank you for being

the person I could talk to.

I am also very grateful to have met and worked with Elizabeth Cochran, who was my original graduate advisor. Elizabeth, you have always believed in me - right from the start. You have always been supportive, you were tough on me when I deserved it, and never settled for less than the best. Thank you for all your encouragement!

To the most amazing group of friends and family a woman could ask for. Thank you to my parents, Mom and Deb, and my sisters Jara and Marchelle, for being my constant support system. The four of you will always be my heroes, my loving family.

To Jason Enneking, you have made these last months, the craziest of my life, bearable. You are my calm at the center of the storm, the rock I lean on, the silly kid I laugh with. I love you and I cant wait to spend the rest of my life with you (and Fort Squarepants!).

To Harmony Colella, Chad Severson, Joe Collette, Laura Bilenker, Joanna Oseguera, Sara Henry, Megan Rohrsson, Rob Ellis, Mike Floyd, Jason McMillian, Jacqui Gilchrist, Julian Lozos, Allie Hutchison, James Burnham, Philip Meeker, Chris Rollins, Amir Allam, and Jerlyn Swiatlowski - you have all made this voyage so much fun!

Finally, to Jascha Polet, if it weren't for you, I'd never have considered becoming a seismologist.

ABSTRACT OF THE DISSERTATION

Understanding Local-Scale Fault Interaction Through Seismological Observation and Numerical Earthquake Simulation

by

Kayla Ann Kroll

Doctor of Philosophy, Graduate Program in Geological Sciences
University of California, Riverside, March 2016
Dr. James H. Dieterich, Chairperson

A number of outstanding questions in earthquake physics revolve around understanding the relationships among local-scale stress changes, fault interactions (i.e. how stresses are transferred) and earthquake response to stress changes. Here, I employ seismological observations and numerical simulation tools to investigate how stress changes from a mainshock, or by fluid injection, can either aid or hinder further earthquake activity. Chapter 2.2 couples Coulomb stress change models with rate- and state-dependent friction to model the time-dependent evolution of complex aftershock activity following the 2010 El Mayor-Cucapah earthquake. Part III focuses on numerical simulations of earthquake sequences with the multi-cycle earthquake simulator, RSQSim. I use RSQSim in two applications; 1) multi-cycle simulation of processes that controlling earthquake rupture along parallel, but discontinuous, offset faults (Chapter 3), and 2) investigation of relationships between injection of fluids into the subsurface and the characteristics of the resulting induced seismicity (Chapter 4).

Results presented in Chapter 2.2 demonstrate that both increases and decreases in

seismicity rate are correlated with regions of positive and negative Coulomb stress change, respectively. We show that the stress shadow effect can be delayed in time when two faulting populations are active within the same region. In Chapter 3, we show that the pre-rupture stress distribution on faults governs the location of rupture re-nucleation on the receiver fault strand. Additionally, through analysis of long-term multi-cycle simulations, we find that ruptures can jump larger offsets more frequently when source and receiver fault ruptures are delayed in time. Results presented in Chapter 4 demonstrate that induced earthquake sequences are sensitive to the constitutive parameters, a and b, of the rate-state formulation. Finally, we find the rate of induced earthquakes decreases for increasing values of hydraulic diffusivity.

Contents

List of Figures

List of Tables

Part I

Introduction

Chapter 1

Introduction

1.1 Summary of Projects

Contained in this thesis are a collection of studies that investigate the local-scale fault interactions through the use of seismological observations and numerical simulation of earthquakes. Each of these topics couples measurement of stress transfer related to slip on a fault during an earthquake and the application of the laboratory-derived rate- and state-dependent frictional formulation (Section 1.2) to explain the time-dependent behavior of earthquake sequences. These projects include how aftershocks are triggered and suppressed (Chapter 2.2), how earthquake ruptures propagate across fault stepovers (Chapter 3), and how pore-fluid pressure perturbations induce earthquake sequences (Chapter 4).

In Chapter 2.2, we discuss the relationship between static stress changes imparted by displacements along faults during earthquakes and the accompanying changes in the rate of seismicity; a fundamental research goal in earthquake physics. Theoretically, fault displacement leads to stress increases and decreases in the surrounding rock volume. Many

authors have shown that the positive stress changes caused by a mainshock lead to an increase in the number of aftershocks. However, the correlation between stress decreases and seismic quiescence has been less frequently observed. Here, we present a compelling example of the correlation between static stress changes and their effect on subsequent seismicity rates.

In Chapters 3 and 4 in Part III we use numerical simulations of earthquakes to investigate: 1) how earthquake rupture across fault stepovers is affected by stress heterogeneities at the time of earthquake rupture, and by time-dependent failure (Chapter 3), and 2) the seismic response to pore-fluid pressure changes caused by fluid injection (Chapter 4). We employ RSQSim, a 3D physics-based boundary element earthquake simulator that implements the rate- and state-dependent frictional formulation which strongly affects the spatio-temporal clustering of seismicity. Use of the rate-and state-dependent frictional formulation allows RSQSim to simulate several types of earthquake slip phenomena including traditional stick-slip earthquakes, fault creep, tremor, slow slip earthquakes, and afterslip. Additionally, the rate-state effects give rise to earthquake clustering effects such as aftershock and foreshock activity. The computational efficiency of RSQSim allows for system-scale multi-cycle earthquake simulations over thousands of years from which statistically significant characterizations of fault interaction can be drawn (Section 1.3).

In Chapter 3, we compare properties of earthquake rupture in long-term simulations with RSQSim with those from fully dynamic earthquake rupture models. In RSQSim, the stresses along faults evolve naturally over time due to fault interaction. We show that earthquake ruptures are highly sensitive to the initial stress field. We also determine the

probability that earthquakes will rupture across fault stepovers of varying offsets. We document the state of stress on faults before every earthquake that successfully ruptures across the stepover. Finally, in cases where earthquakes do not rupture both fault segments as a part of the same event, we determine the probability that the second fault will rupture after a short time delay that ranges from minutes to years.

Chapter 4 focuses on simulating seismic sequences induced by pore-fluid pressure changes related to the injection of fluids into the subsurface. While it has long been known that fluid injection causes earthquakes, the topic has received renewed attention in recent years due to the nearly exponential increase in the number of earthquakes in the Central and Eastern United States since 2009 (Ellsworth, 2013). The increased rate of seismicity has been associated with the disposal of waste-water recovered during oil and gas production. Of particular scientific interest, is the fact that the majority of waste-water disposal wells are not correlated with induced seismicity. Here, we use RSQSim to investigate the relationship between induced seismicity sequences and several properties that include, 1) reservoir characteristics, 2) pre-existing stress conditions on the fault, and 3) the rate-state parameters of faults.

1.2 Rate- and State-Dependent Friction

Original studies of the force due to friction date back as far as Leonardo da Vinci during the 15^{th} century and were supported by only a handful of studies until the last 100 years. In the most general sense, early laboratory studies showed that the force of friction is linearly proportional to the normal force acting perpendicular to the sliding surface, and

that friction is independent of the area of the sliding surface. In this framework, the shear stress (τ), parallel to a sliding surface, is related to the normal stress (σ) simply by friction, μ;

$$\tau = \mu\sigma, \tag{1.1}$$

where μ was thought to be constant. However, modern laboratory experiments of friction reveal that, not only is the force of friction not constant, but it is profoundly affected by weak dependencies on both the slip rate and the state, which is interpreted as the age of contacts between the sliding surfaces (Marone, 1998). The constitutive relationship describing the rate- and state-dependence of friction was first introduced by Dieterich (1978, 1979, 1981), and expanded on by (Ruina, 1983; Rice, 1983a,b). These investigators were interested in the repeated stick-slip failure observed during the earthquake cycle. Dieterich (1979); Ruina (1983) demonstrate that the rate- and state-dependent constitutive law of friction successfully describes nearly the full range of fault slip phenomena from earthquake nucleation to interseismic behavior (Marone, 1998).

Laboratory analyses of rock friction were conducted in a series of experiments including the so-called "slide-hold-slide" test and velocity step tests. In the former, samples are subjected to constant loading rates where sliding is interrupted for a specified amount of time. In the latter case, the loading rate was varied in a series of steps. These experiments led to the discovery that static friction, that is, the friction along a surface *just before* sliding, increases with the logarithm of the hold time. Alternatively, the force of friction *during* sliding, known as the dynamic friction, decreases with increasing slip speed. These concepts are related in the development of the rate- and state-dependent constitutive law

of friction given by;

$$\mu = \mu_0 + a \ln \left(\frac{V}{V^*} \right) + b \ln \left(\frac{V^* \theta}{D_c} \right), \tag{1.2}$$

where a and b are the constitutive parameters that describe the material, D_c is the characteristic slip distance over which the state variable (θ) evolves, τ and σ are the shear and normal stresses, μ_0 is the steady-state coefficient of friction at the reference slip speed, V^*, and V is slip speed during frictional sliding. A state-evolution equation is required in order to fully describe the evolution of state with slip, time, and changes of normal stress. Several state-evolution laws have been proposed, including the aging and slip laws. The aging law (Dieterich, 1979) assumes that θ will evolve with time even if the surfaces are not sliding, whereas the slip law (Ruina, 1983) assumes that θ will evolve only during slip. In the following work, we use a form of the aging law that incorporates the normal stress dependencies of θ give by;

$$\dot{\theta} = 1 - \frac{\theta V}{D_c} - \alpha \left(\frac{\theta \dot{\sigma}}{b \sigma} \right), \tag{1.3}$$

where α is the constant with values between 0 and the nominal coefficient of friction that controls the strength of the normal stress dependence (Linker and Dieterich, 1992). From Equation 1.3 at constant normal stress, state evolves to a constant steady-state value ($\theta_{ss} = D_c/V$). Hence, from Equation 1.2, μ becomes;

$$\mu_{ss} = \mu_0 + (a - b) \ln \left(\frac{V}{V^*} \right) \tag{1.4}$$

Note that when $a > b$ in this relationship, friction increases with sliding rate, whereas rate-weakening conditions arise with $a < b$. Rate-weakening is a necessary condition for

unstable slip.

The rate-state constitutive law has been used to model all types of earthquake slip phenomena (Marone, 1998). These applications include preseismic slip, earthquake nucleation (Dieterich, 1992), coseismic rupture (Tse and Rice, 1986; Ryan and Oglesby, 2014), afterslip (Marone et al., 1991; Wennerberg and Sharp, 1997), fault creep (Sleep, 1995; Barbot et al., 2009), non-volcanic tremor (Cochran et al., 2013), and slow slip events (Colella et al., 2011, 2012) . Because the rate-state formulation contains the time-dependent evolution of the state term, θ, this formulation also gives rise to the time-dependent clustering behavior characteristic of earthquake sequences including aftershock and foreshock activity.

In Chapter 2.2, we employ the earthquake rate equations developed by Dieterich (1994) to model the time-dependent evolution of an aftershock sequence. The earthquake rate is given by;

$$R = \frac{r}{\gamma \dot{S}_r} \tag{1.5}$$

where R is the earthquake rate, r is the reference seismicity rate at the Coulomb stressing rate, $\dot{S}_r$ and γ is a variable that evolves by;

$$d\gamma = \frac{1}{a\sigma}[dt - \gamma dS] \tag{1.6}$$

where a is the rate-state constitutive parameter, and σ is the normal stress. The earthquake rate following a stress step (ΔS), assuming a constant stressing rate is given by,

$$R(t) = \frac{1}{\frac{\eta}{\dot{S}} + \left(\frac{1}{r} - \frac{\eta}{\dot{S}}\right) \exp\left(\frac{-\dot{S}t}{a\sigma}\right)} \tag{1.7}$$

where η is the ratio of the reference stressing rate, $\dot{S}_r$ to the reference background seismicity rate, r; (*i.e.* $\eta = \dot{S}_r/\mathrm{r}$).

1.3 Simulating Earthquakes with RSQSim

Included in this volume are two chapters that use a numerical modeling approach to investigate the relationship between the evolution of stress along faults and the resulting seismicity (Chapters 3 & 4). We use RSQSim, a 3D, quasi-dynamic boundary element earthquake simulator that employs the rate- and state-dependent frictional formulation. RSQSim is capable of simulating multiple types of earthquake slip phenomena including stick-slip, slow slip, tremor, creep, and afterslip and generates synthetic catalogs of $> 10^6$ earthquakes with characteristics similar to observed seismicity (Richards-Dinger and Dieterich, 2012; Tullis et al., 2012). In each simulation, earthquake slip speed is assumed to be constant and is set as an input parameter, but earthquakes spontaneously nucleate and all other earthquake rupture parameters including extent of slip, rupture propagation speed, and final slip distribution are deterministic. Single-event RSQSim results have been validated against those of fully dynamic rupture models to ensure accurate implementation of computational approximations to elastodynamics (Dieterich and Richards-Dinger, 2010; Richards-Dinger and Dieterich, 2012). For example, comparisons between RSQSim and Dyna3D show similar time histories, stress changes, and total slips for single-event ruptures on a planar fault (Dieterich and Richards-Dinger, 2010; Richards-Dinger and Dieterich, 2012).

Input requirements for RSQSim include a fault model comprised of rectangular

or triangular fault elements, a long-term average slip rate, starting values of the shear and normal stresses, and the constitutive parameters of the rate-state formulation for every fault element (Equation 1.2). RSQSim employs the aging form of the state-evolution law which includes the normal stress dependence of θ given by Equation 1.3. In RSQSim, the frictional parameters may be uniform or they may vary from element to element depending on the goal of the simulation (default values used in this study are based on laboratory estimates and are listed in Table 1.1).

Prior to a simulation, a one-time "backslip" calculation is performed to determine normal stressing rates needed to drive the long-term forward slip at some assigned slip-rate. This consists of slipping all the faults backwards at their long-term average slip rate. Thus, backslip includes all sources of stress that control fault slip rates (*i.e.* tectonic loading, off-fault or viscoelastic deformation, fault stress interactions) (Savage, 1983; Tullis et al., 2012; Richards-Dinger and Dieterich, 2012). Faults are represented as a collection of elastic dislocation sources. The changes in shear and normal stress at the center of all elements i due to slip of element j are given by;

$$\dot{\tau}_i = \mathbf{K}^{\tau}_{ij} V_j + \dot{\tau}^{tect}_i, \tag{1.8}$$

and

$$\dot{\sigma}_i = \mathbf{K}^{\sigma}_{ij} V_j + \dot{\sigma}^{tect}_i, \tag{1.9}$$

where $\dot{\tau}^{tect}_i$ and $\dot{\sigma}^{tect}_i$ are constant external stressing rates from the backslip calculation, summed over all indices, and $\mathbf{K}^{\tau}$ and $\mathbf{K}^{\sigma}$ stiffness matrices given by the Green's function for a homogeneous elastic half-space (Okada, 1992).

During a simulation, earthquake nucleation must occur spontaneously within a

single element. Therefore, to generate stick-slip behavior, the stiffness of each element, K, must be small with respect to the critical stiffness [$K_c = \frac{\sigma(b-a)}{D_c}$]. Assuming $K_c = \frac{\Delta\tau}{d}$ and $\Delta\tau = \frac{G\eta d}{L}$, the critical length (radius) for nucleation is related to the stiffness and the characteristic slip distance such that $L_c = \frac{G\eta D_c}{\sigma(b-a)}$ (Dieterich, 1992), where d is slip, G is the shear modulus (e.g. 30 GPa) and η is a constant related to the geometry of the slipping element (e.g. 1.05 for rectangular elements). Given the default values of σ, D_c, and the constitutive parameters $(b-a)$ listed in table 1.1, $2\mathrm{L}_c = 1.26$ m. Since computation time roughly scales by the square of the number of elements and models with 10^4 to 10^6 elements are computationally feasible, element sizes generally vary between $20\mathrm{L}_c$ and $1000\mathrm{L}_c$ depending on the geographical size of the fault model.

Parameter	Value
a	0.01
b	0.015
D_c	10 μm
τ_0	60 MPa
σ_0	100 MPa
μ_0	0.6
θ	$2 \cdot 10^8$ sec
V^*	10^{-6} m/s
V^{EQ}	1 m/s

Table 1.1: Default parameter values in RSQSim.

To increase computational efficiency, RSQSim makes approximations that permit use of analytic solutions for the evolution of stress, slip speed, and the state variable, θ (for a comprehensive explanation, see Richards-Dinger and Dieterich (2012)). In summary, RSQSim uses event-driven time-steps that are much faster than time-stepping at discrete intervals. The earthquake cycle is broken up into three states (not to be confused with the state variable, θ); State 0 - Healing, State 1 - Nucleation, and State 2 - Seismic Rupture. An element is in State 0 when shear stress is below steady-state frictional stress given by;

$$\tau^{SS} = \sigma \left[\mu_0 + (a - b) \ln \frac{V}{V_0} \right], \tag{1.10}$$

or equivalently;

$$\tau^{SS} = \sigma \left[\mu_0 + (b - a) \ln \frac{\theta V}{D_c} \right], \tag{1.11}$$

Elements in State 0 are considered locked and stress is not transferred to other elements in the model. During State 0, the $\frac{\theta V}{D_c}$ term is very small and fault elements are considered to be locked, therefore θ evolves by;

$$\dot{\theta} = 1 - \alpha \frac{\theta \dot{\sigma}}{b\sigma}, \tag{1.12}$$

Elements transition to State 1 when the applied shear stress is greater than the steady-state shear stress. For an element in State 1, the evolution of θ is approximated by;

$$\dot{\theta} \approx \frac{\theta V}{D_c} - \alpha \frac{\theta \dot{\sigma}}{b\sigma}, \tag{1.13}$$

where θ decreases until the seismic slip speed, V^{EQ}, is reached and the element transitions to State 2. Slip on elements during the nucleation phase is ignored because it is considered to be small compared to slip during seismic rupture. During States 0 and 1,

RSQSim uses a quasi-static approximation so the frictional shear stress is simply equal to the applied shear stress. However, this approximation is no longer valid as slip speeds accelerate toward seismic velocities. Therefore, RSQSim employs a quasi-dynamic representation of gross dynamics of the earthquake source in the formulation of V^{EQ} in State 2, which is related to elastic shear impedance and the local driving stress. This approach is a first-order approximation to the dynamical time scales and slip rates during co-seismic rupture. V^{EQ} is given by;

$$V^{EQ} = \frac{2\beta\Delta\tau}{G} \tag{1.14}$$

Equation 1.14 is based on analytical slip speed solutions of Dieterich (2007). Once an element transitions to State 2, the slip speed is held constant until the element reverts back to State 0, when the applied shear stress drops below steady-state. Stress from slip on every jth element in State 2 is transferred to every other ith element in the model by adding the external stresses (on the ith element) to the product of slip (on the jth element) and the element stiffness (between the ith and jth element) such that;

$$\dot{\tau}_i = \dot{\tau}_i \pm K^{\tau}_{ij} V^{EQ}_j, \tag{1.15}$$

and

$$\dot{\sigma}_i = \dot{\sigma}_i \pm K^{\sigma}_{ij} V^{EQ}_j, \tag{1.16}$$

Equations 1.15 and 1.16 apply to both State 1 to State 2 transitions by addition of the second term, and to State 2 to State 0 by the subtraction of the second term.

Two further approximations of elastodynamics are made in RSQSim to enable rupture propagation (1), and to control the shape of the slip pulse (2). 1) Rupture propagation is aided by the reduction of the rate-coefficient (a), and 2) a dynamic overshoot

parameter controls the shape the the slip pulse (*i.e.* either crack-like or pulse-like). Stress concentrations at the edges of the elements are poorly resolved due to the large element size and because stress changes are only computed at the center of each element, therefore it is unrealistically difficult for ruptures to propagate. RSQSim reduces the value of the rate-coefficient, a (Eq. 1.2), in the neighborhood of all elements in State 2 which decreases the time to instability and allows rupture to propagate more naturally. Lastly, RSQSim implements a stress overshoot factor, s, similar to that of the dynamic overshoot of sliding friction common to fully dynamic models. The stress overshoot factor scales the steady-state shear stress such that an element will stay in State 2 longer for small values of s (based on Eq. 12 and 13 in Richards-Dinger and Dieterich (2012)). For homogeneous initial conditions in single-event simulations, this causes elements to quickly switch between locked and sliding states, which approximates continuous slip in crack-like ruptures. If s is large, rate-state healing effects quickly cause elements to revert to State 0 and never fail again, similar to pulse-like ruptures. For multi-cycle simulations common with RSQSim, heterogeneous stresses lead to more pulse-like ruptures, even for small s values.

Part II

Seismological Observation of Earthquake Triggering and Migration

Chapter 2

Observations of Seismicity Rate Changes in the Yuha Desert, California

2.1 Introduction to Earthquake Triggering and Suppression

The ability to identify regions susceptible to earthquake triggering and quiescence is critical for estimates of seismic hazard following large earthquakes. Earthquakes modify the stress field in two ways; 1) permanent, or static, stress changes associated with displacement along the fault surface and 2) transient, oscillatory, dynamic stress changes caused by the passage of seismic waves. While static stress changes decay rapidly with distance away from the mainshock rupture, dynamic stresses are transmitted over thousands of kilometers. Both types of stresses have been shown to trigger earthquakes within several rupture

dimensions from a mainshock (Hill et al., 1993; Kilb et al., 2000; Freed, 2005; Toda et al., 2012). There is a general agreement within the scientific community that dynamic stresses, rather than static, are responsible for earthquake triggering at teleseismic distances (Belardinelli et al., 1999; Cotton and Coutant, 1997; Gomberg et al., 2003; Kilb et al., 2000; Felzer and Brodsky, 2005), with noteable cases of teleseismic triggering following the 1992 Landers and 2002 Denali earthquakes (Hill et al., 1993; Kilb et al., 2000; Gomberg et al., 2003).

Whether earthquakes are triggered by static or dynamic stress changes in the near-field is a topic of vigorous debate. This controversy arises because both types of stress changes are active within a 1-2 fault dimensions from a mainshock and are of similar magnitude. Some authors [*i.e.* (Felzer et al., 2002; Felzer and Brodsky, 2005)] argue that dynamic stress changes play a more prominent role than that of static stress changes in the triggering of earthquakes at all distances. Felzer and Brodsky (2005) explain that effects such as the asymmetric distribution of aftershocks in the direction of rupture directivity are caused by near-field dynamic rather than static stress transfer. Proponents of near-field static stress triggering search for regions of seismic quiescence in shadow zones to assert that the permanent static stress changes dominate over dynamic stresses, and therefore, are the primary mechanism for earthquake triggering/suppression in the near-field (Stein, 1999; Freed, 2005; Toda et al., 2005).

Generally, investigations of the effects of stress changes on earthquake rates employ the simple Coulomb failure criterion to identify geographical regions surrounding a mainshock where aftershock activity would be expected to be enhanced or suppressed by static

stress changes (Stein, 1999; Freed, 2005). In the simplest form, the change in Coulomb failure stress (ΔCFS) is give by,

$$\Delta CFS = \Delta\tau + \mu(\Delta\sigma + \Delta P) \tag{2.1}$$

where ΔP is the pore fluid pressure change, μ is the coefficient of friction (which ranges from 0 to 1), $\Delta\tau$ and $\Delta\sigma$ are the shear and normal stress changes, respectively. In this form, $\Delta\tau$ is positive in the direction of fault slip and $\Delta\sigma$ is positive in extension. Failure is encouraged for increased shear or decreased normal stresses (increased extension). The Coulomb failure hypothesis suggest the earthquake rate increases in regions of positive ΔCFS (*i.e.* triggering zones) and is suppressed in negative stress change lobes (*i.e.* shadow zones) (Stein, 1999).

Several studies have shown enhanced seismicity correlated with regions of positive ΔCFS (Stein et al., 1994; Toda et al., 1997; Stein, 1999; Toda and Stein, 2002, 2003; Ma and Chan, 2005; Toda and Matsumura, 2006; Toda et al., 2011; Sevilgen et al., 2012; Toda et al., 2012; Meng et al., 2013; Meng and Peng, 2014; Sarkarinejad and Ansari, 2014). Because the irregular slip distribution and fault geometry are generally not accounted for in Coulomb modeling (Freed, 2005), the best correlations between seismicity rate increases in Coulomb triggering zones are seen a few kilometers from the mainshock. Unfortunately, few studies have definitively correlated seismicity rate decreases with regions of negative ΔCFS (Toda and Stein, 2002; Ma and Chan, 2005; Toda et al., 2012; Maccaferri et al., 2013). Therefore, a consensus on the importance of static versus dynamic triggering in the near-field has yet to form.

The process of searching for correlations between seismicity rate changes and

Coulomb stress changes involves a number of steps and requires a large number of well located earthquakes before and after a mainshock. In general, the analysis can be separated into two parts, 1) mapping the spatial distributions of Coulomb stress changes, and 2) computing seismicity rates in regions of increased or decreased Coulomb stress. A short summary of the processing steps involved in this analysis are itemized (in terms of simple versus complex assumptions) and discussed below (steps $A-C$ relate to item 1, and $C-D$ are related to item 2);

A) Knowledge of the earthquake source: (*i.e.* source (mainshock) fault orientation, pattern of slip, and slip vector). In the simplest of circumstances, a moment tensor solution can provide the fault orientation, and slip direction. Average slip across the entire rupture plane can be computed from estimates of seismic moment. For a more thorough analysis, a slip inversion or finite fault model can provide more realistic results.

B) Knowledge of the receiver faults: It is important to note that the resulting spatial pattern of Coulomb stress change is highly dependent upon the orientation of planes onto which the stresses are resolved. One can assume receiver faults of various orientations *i*) the same orientation of the mainshock rupture, *ii*) the optimally oriented faults, *iii*) optimally oriented strike-slip (or thrust, or normal) faults, *iv*) receiver fault orientation based on mapped faults in the local area, or *v*) the nodal plane orientations from focal mechanism solutions (although, it is important to consider the uncertainties associated with focal mechanism determination, as well).

C) Friction and depth: Coulomb stress changes vary as a function of depth and the coefficient of friction, therefore it is important to determine how sensitive the Coulomb

stress change results are to systematic variations in these parameters.

D) Subdivision of the earthquake catalog: Earthquakes can be subdivided by geographical regions associated positive and negative stress changes. This process may be complicated due to the fact that many geographical regions commonly exhibit earthquakes from more than one faulting style (*i.e.* strike-slip, normal, reverse faults). As previously mentioned, the location of the positive and negative stress change lobes will vary depending on the receiver fault orientation, so simply subdividing the earthquake catalog by stress change regions defined by one faulting type may result in a catalog with a mix of focal mechanisms. This will likely effect the earthquake rates, so it is important to ensure that events within each group have focal mechanisms consistent with the orientation of the receiver faults, if possible.

E) Computation of earthquake rates: compute earthquake rates for each of the subdivided catalogs individually. Because the rate curves can be rather noisy, even after smoothing, it may be more clear/advantageous to compute the cumulative number of events, in addition to the rate.

Many studies have successfully demonstrated the effects of static stress transfer in an earthquake sequence by coupling a Coulomb stress transfer model with the rate-state earthquake rate formulation (Dieterich, 1994). Coupled Coulomb rate-state models explain the time-dependent behavior of seismicity sequences such as the immediate increase in seismicity rate following a positive stress step, Omori-like decay of aftershock sequences, or migration away from a fault with time (Toda and Stein, 2003; Toda et al., 2005, 2012; Cattania et al., 2015).

To date, the most convincing observation of seismic quiescence in a stress shadow occurred following the 1992 Landers earthquake (Toda et al., 2012). The quality and detail of the earthquake catalog, both before and after the Landers earthquake, greatly clarified their results. Their assessments of earthquake rate changes were based on a precisely located earthquake catalog complete to M$\sim$1.5. Additionally, the high rate of background seismicity (in this case, aftershocks of the 1992 Joshua Tree earthquake) allow for a statistically significant estimate of the seismicity rate decrease in the stress shadow zones of the Landers earthquake (Toda et al., 2012).

A global search for stress shadows led Mallman and Parsons (2008) to suggest a new method to elucidate the role of static stress changes in the near-field region with multiple styles of faulting. Mallman and Parsons (2008) propose a new definition of a static stress shadow, following (Reasenberg and Simpson, 1992), who suggest that the 1906 San Francisco earthquake generated a static stress shadow on receiver faults oriented parallel to the mainshock rupture, but a static stress increase on thrust faults oriented similar to that of the 1989 Loma Preita event. By their definition, stress shadows can be identified based on decreases in seismicity rate for a given faulting regime (Mallman and Parsons, 2008). For the 1906-Loma Prieta example, strike-slip events would be inhibited, whereas thrust events would be encouraged.

In Chapter 2.2, we combine the methods described in this section (*i.e.* Coulomb stress transfer, the rate-state earthquake rate formulation, and the Mallman and Parsons (2008) definition of a stress shadow) and present a definitive observations of seismic quiescence related to negative static stress change.

2.2 Delayed Seismicity Rate Changes Controlled by Static Stress Transfer

2.2.1 Abstract

A fundamental goal of research in earthquake physics is to establish a quantitative relationship between changes in stress and the occurrence of earthquakes. The Coulomb failure stress (CFS) hypothesis together with the rate-state formulation for seismicity rates is generally quite successful at predicting aftershock rates in areas where CFS increases following a mainshock (Toda and Stein, 2002, 2003; Toda et al., 2012; Segou and Parsons, 2014). However, the expected reduction or shutdown of seismicity in regions of CFS decrease (often referred to as the stress shadow effect) is problematic in that shutdowns are less-frequently observed and often appear to be delayed by days to months following the mainshock stress perturbation (Jaumé and Sykes, 1996; Harris and Simpson, 1996; Wyss and Wiemer, 2000; Toda and Stein, 2002, 2003; Woessner et al., 2004; Daniel et al., 2006; Toda et al., 2012). Here, we report seismicity rate increases and decreases following the 15 June 2010 M5.72 Ocotillo earthquake in the Yuha Desert, California that correlate with regions of positive and negative CFS change (ΔCFS). We demonstrate, for the first time, that the delayed stress shadow effect can be modeled by projecting the coseismic stress changes onto two populations of faults, wherein the stress changes promote failure on faults of one orientation, while suppressing activity on the other.

2.2.2 Introduction

CFS theory states that earthquakes are instantaneously encouraged or suppressed by coseismic increases or decreases of CFS, respectively. The Coulomb failure stress is given by,

$$CFS = \tau + \mu(\sigma - p) \tag{2.2}$$

where τ is shear stress, σ is the normal stress, p is the pore fluid pressure and μ is the coefficient of friction. In this study we hold p constant - hence, increases in τ and/or decreases in σ can lead to earthquake triggering by $+\Delta CFS$, whereas -τ and/or $+\sigma$ may result in seismic quiescence due to $-\Delta CFS$. Geographical regions of $+\Delta CFS$ and $-\Delta CFS$ known as stress triggering and shadow zones, respectively, are determined by projecting the instantaneous stress changes onto receiver faults (King et al., 1994; Toda et al., 2011), assuming constant pore pressure. Because CFS depends on both the fault plane and slip vector orientations, in areas of complex faulting, the stress changes from a mainshock may induce $+\Delta CFS$ for one fault orientation, while causing $-\Delta CFS$ for a different receiver fault orientation. For example, it was noted that in the 75 years following the 1906 San Francisco earthquake, strike-slip events were inhibited due to $-\Delta CFS$ on that receiver, while thrust events such as the 1989 Loma Prieta event were promoted by $+\Delta CFS$ (Reasenberg and Simpson, 1992).

While numerous observations have correlated earthquake triggering and elevated seismicity rates with regions of $+\Delta CFS$ (Stein and Lisowski, 1983; Stein et al., 1994; Pollitz and Sacks, 1997; Stein et al., 1997; Parsons and Dreger, 2000; Lin and Stein, 2004; Toda et al., 2011), observations of seismic quiescence in stress shadow regions are more

controversial (Marsan and Nalbant, 2005; Mallman and Zoback, 2007; Toda et al., 2012) with some studies failing to show a correlation between seismic quiescence and stress shadows (Felzer and Brodsky, 2005; Mallman and Zoback, 2007). Furthermore, in many instances, the stress shadow effect is not observed immediately following an earthquake rupture, but appears to be delayed by days to months (Jaumé and Sykes, 1996; Harris and Simpson, 1996; Wyss and Wiemer, 2000; Toda and Stein, 2002, 2003; Woessner et al., 2004; Daniel et al., 2006; Toda et al., 2012). Such time-dependent effects can not be explained with CFS theory alone and require a more advanced analysis.

2.2.3 Data

We examine seismicity rate changes in the Yuha Desert, California related to the 4 April 2010 M_w 7.2 El Mayor-Cucapah (EMC) earthquake and subsequent 15 June 2010, M_w5.7 Ocotillo (OCO) aftershock. The EMC ruptured northwestward in the Gulf of California arresting just south of the Yuha Desert, California where it elevated seismicity rates along predominately NW and NE trending right- and left-lateral conjugate strike-slip faults, and east trending normal faults (Kroll et al., 2013) (Supplementary Figures 1 & 2). We use a relocated earthquake catalogue with focal mechanism solutions (Yang et al., 2012) to determine the effect of the OCO event on the decaying EMC aftershock sequence. The catalogue contains 5582 events in the Yuha Desert ($M_c = 1.5 < M_L < 5.72$) between 4 April 2010 and 31 December 2010. Of these we consider the subset of 4421 events that have consistent focal mechanisms for faulting type (*i.e.* both nodal planes indicate the same faulting type). This dataset contains 2852 strike-slip, 1201 normal, and 368 reverse faulting earthquakes.

2.2.4 Coulomb Stress Modeling

To investigate the relationship between ΔCFS and the time-dependent rates of earthquake activity, we couple a CFS change model with the seismicity rate equations (see Appendix) from the rate- and state-dependent formulation for fault friction (Dieterich, 1994) to model changes in aftershock rates as a function of time in the Yuha Desert. Our approach involves a number of steps. First we identify geographic regions of ΔCFS in response to OCO using Coulomb V3.3 (King et al., 1994; Toda et al., 2011) for the two dominant faulting types in the Yuha Desert. Next we subdivide the seismicity catalog into groups based on their location within a triggering or shadow zone. Ideally, selection of geographic regions of positive and negative stress change and subsequently grouping of aftershocks within each region would result in the selection only of earthquakes that ruptured a fault plane similar to that of the receiver fault used in the Coulomb modeling. However, it is common, especially in regions of complex fault geometry, for aftershocks to rupture on different fault types (*i.e.* normal as opposed to strike-slip fault). This may lead to the grouping of aftershocks with stress changes of both signs, even though they are located in a region of positive $+\Delta CFS$ for the given receiver fault orientation. For this reason, we first group aftershocks by geographic region and then further subdivided that population based on the sign of the ΔCFS resolved on each event's focal mechanism. Finally, we compare the observed earthquake rate after the EMC event to that predicted by the Omori aftershock decay law to determine the effect of static stress transfer induced by the OCO event on the EMC aftershock sequence.

We use the gCMT moment tensor solution and the distribution of aftershock lo-

cations along the mainshock rupture plane to estimate the source fault characteristic of the OCO event. This source fault was then used to model Coulomb stress changes on the two receiver fault orientation. These include northeast trending left-lateral strike-slip faults and east-trending normal receiver faults (Figure 2.1). For strike-slip receiver faults, we use the fault orientation that is consistent with the average strike of NE trending, left-lateral faults in the eastern Yuha Desert that exhibited surface slip related to the EMC event (Rymer et al., 2011) and a vertical dip as suggested by the seismicity (Kroll et al., 2013). For normal receiver faults, we use the average normal faulting nodal plane orientation from the focal mechanism catalogue (Yang et al., 2012) because few normal offsets were observed in the field following the EMC event (Figure 2.1b). Results for both receiver fault types indicate a stress shadow zone in the eastern Yuha Desert and a triggering zone to the south of the OCO source fault plane. Note that the region directly west of the OCO source fault lies in a stress shadow for left-lateral receiver faults and in a triggering zone for normal receiver faults. See Supplementary Figures 3 & 4 for alternate receiver fault solutions. We use the Coulomb stress change results for left-lateral receiver faults (Figure 2.1a) in our analysis of seismicity rate changes as this is consistent with the most prevalent style of faulting.

We group earthquakes based on their location within the geographical regions of positive or negative stress change which are labeled in Figure 2.1a as the eastern and western shadow zones, regions I and III, respectively, and the south-southwest triggering zone, region II. Next, we compute the Coulomb stress change on the nodal plane of each event's focal mechanism. Within each of the three earthquake catalogs, less than 20% of events within each region have a stress change that of the opposite sign as the region in which it lies.

For example, Region I (a stress shadowed zone for northeast left-lateral receivers) of the 1800 events examined, ∼300 have $+\Delta CFS$ despite the fact that this region lies in a stress shadow zone. 236 of the 300 earthquakes that occur in Region I with $+\Delta CFS$ are east trending right-lateral strike-slip events that fall into a stress triggering zone after OCO when the Coulomb stress change is resolved onto that receiver fault orientation (Supplementary Figure 5).

According to CFS theory, seismicity rates should increase or decrease instantaneously for populations of events with $+\Delta CFS$ or $-\Delta CFS$, respectively. To quantify the effect of static stress changes imparted by the OCO event on the EMC aftershock sequence, we first fit the aftershock rate in the time period between the EMC and OCO (5 April and 15 June 2010; unless otherwise noted) with the modified Omori-Utsu aftershock decay law given by;

$$R = \frac{K}{(c+t)^{-p}} \tag{2.3}$$

where K and c are constants, t is time, and p is the variable exponent of the power law decay. We use the maximum-likelihood method (Ogata, 1981) to invert for the parameters Equation 2.3. We then compare the observed seismicity rates after OCO to the rate predicted by the Omori-Utsu aftershock decay law. Deviations of the observed earthquake rate from that predicted by the Omori decay law after OCO give a measure of the effect of the coseismic static stress change imparted by OCO on the EMC aftershock sequence.

Figure 2.2a shows how all aftershock were originally grouped by regions of positive or negative Coulomb stress change, and then further subdivided on the basis of the stress change resolved individually onto each event's focal mechanism. Figures 2.2b - g, show the

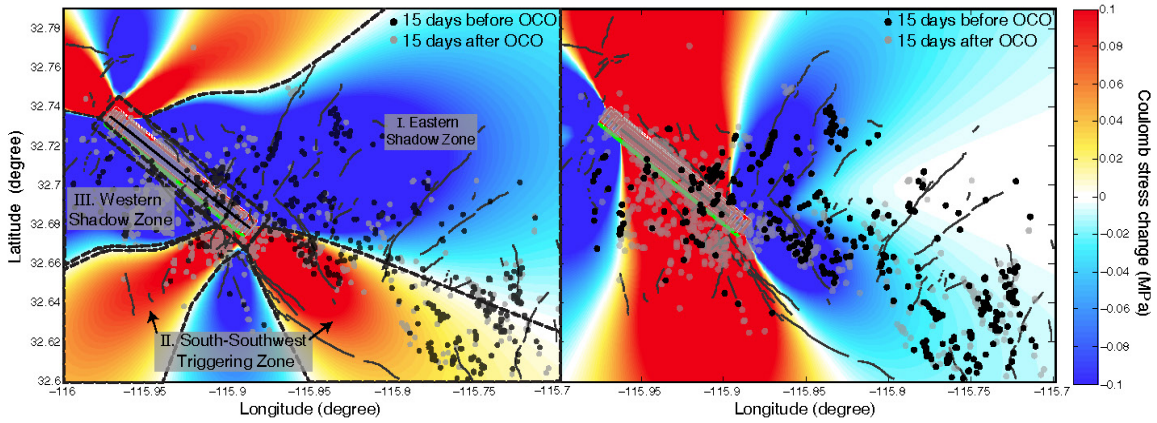

Figure 2.1: ΔCFS imparted by the OCO event in the Yuha Desert. ΔCFS is computed at 5 km depth assuming a of $\mu = 0.5$ on a planar source fault (strike 313°, dip = 84°, rake = 173°, from the gCMT catalog) with 0.23 m of net slip, tapered towards the fault tips. Left) ΔCFS for northeast trending left-lateral receiver faults (strike = 20°, dip = 90°, and rake = 0°). Right) ΔCFS for east trending normal receiver faults (right; strike = 85°, dip = 46°, and rake = -101°). Seismicity 15 days prior to (black) and 15 days following (grey) the OCO event show an increase in seismicity rate in triggering regions for left-lateral (S-SW Yuha Desert) and for normal (western Yuha Desert) receiver faults. A seismicity shutdown occurs in the stress shadow Region I for left-lateral receiver faults.

relationship between the observed event rate for each of the six populations of events, and the decay predicted by fitting an Omori decay curve to the the observed seismicity in each population between the time of the EMC and OCO events (unless otherwise noted). For events with positive stress changes (*i.e.* Figures 2.2b , d, and f), we expect the seismicity rate to increase after the time of the OCO event. Conversely, for events with negative stress change (Figures 2.2c, e, and g), we expect the rate of the observed seismicity to decrease below the predicted rate after the OCO event. In Region I (Eastern Shadow Zone), seismicity rates only slightly increase above the decaying aftershock activity of the EMC for events with $+\Delta CFS$ (Figure 2.2b). Region II (South-Southwest Triggering Zone) includes several M>4 events with their own aftershock sequences, such as a M4.5 that occurred 44 days after the EMC (Figure 2.2a). This event and the OCO notably increase the rate of

activity in Region II, above the decaying EMC sequence (Figure 2.2d). Earthquake rates remain elevated in Region I and II for ∼60 days, and both distributions exhibit an Omori-like decay. The seismicity rate abruptly decreases immediately following the OCO for events with $-\Delta CFS$ in Region I (Figure 2.2c), due to the stress shadow effect, consistent with CFS theory. The seismicity rate decrease after the OCO event for events with $-\Delta CFS$ in Region II is quite subtle due to the combined effect of the EMC and the M4.5 event. However, the slope of the observed number of events is smaller than of the predicted Omori decay after the EMC, which suggests a decrease in the earthquake rate.

In the stress shadowed, Region III there is an immediate increase in the rate of events following OCO, that abruptly decays to less than the predicted rate ∼23 days later for events with $+\Delta CFS$ (Figure 2.2f), again consistent with the Coulomb failure hypothesis. The abrupt shutdown in seismic activity following this is an interesting effect that we will return to later. Intriguingly, this same pattern persists even for events with $-\Delta CFS$ (Figure 2.2g). The immediate increase in the number of events for earthquakes with $-\Delta CFS$ on their focal mechanisms is not consistent with a simple implementation of Coulomb stress model. However, as shown in Figure 2.1b, this area is a region of positive stress change for normal receiver faults. Based on the complexity of faulting in the Yuha Desert and the inherent uncertainty of focal mechanism analysis, we propose that the delayed stress shadow effect in Region III arises because this population of events is composed of both normal faulting earthquakes for which ΔCFS is positive and strike-slip earthquakes for which ΔCFS is negative.

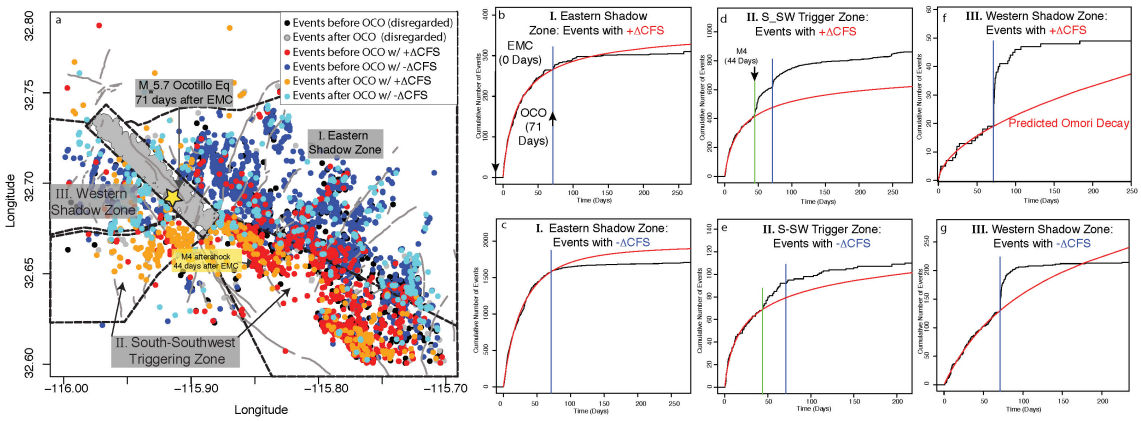

Figure 2.2: All earthquakes with focal mechanism solutions between 4 April and 31 December 2010 and cumulative number of event curve for three regions; eastern and western shadow zones, and a south-southwest trigger zone defined based on the zero ΔCFS region separating the lobes for left-lateral receiver faults Figure 2.1(left). Events are colored by the sign of the ΔCFS on both nodal planes. Event in the near-source region [(gray circles (∼2.5 km wide by 13 km long)] are disregarded as the stress distribution is poorly constrained and highly variable due unresolvable geometrical complexities, slip heterogeneity, and short wavelength fault topography on the fault surface (King et al., 1994; Freed, 2005). Events where one nodal plane has a positive and the other a negative ΔCFS are considered ambiguous and are also disregarded (gray - off fault events). Lighter colors represent events that occurred after OCO. Cumulative number of events (b-f) are shown in black and the rates predicted by the Omori decay law are given in red (fit between 0 and 71 days, unless otherwise noted). The OCO event is marked by the blue vertical line at 71 days following the EMC at 0 days. (c). A M4 aftershock occurs 44 days following EMC (green line) in Region II generates it own aftershock sequence. Here, the rate predicted by the Omori decay law is fit to the data between 0 and 44 days.

2.2.5 Modeling Time-dependent Seismicity Rate Changes

To understand the time-dependent changes in seismicity rate, we use the seismicity rate equations from the rate- and state-dependent frictional formulation (Dieterich, 1994) that incorporates ΔCFS to model earthquake rates assuming two faulting populations in each region. This method has been employed to explain how perturbations in the stress field give rise to clock advances or delays in the time to nucleation of earthquakes (Dieterich, 1992, 1994; Gomberg et al., 1998). Several studies have coupled the earthquake rate equations (Dieterich, 1994) with ΔCFS models to explain the time-dependent response of seismicity to a stress step (Toda and Stein, 2002, 2003; Segou and Parsons, 2014), including a 2.5 day delayed stress shadow effect in a narrow magnitude band following the 1992 M_w7.3 Landers earthquake (Toda et al., 2012).

A simple example of earthquake rates from two fault populations (Figure 2.3) demonstrates the delayed stress shadow effect (Dieterich, 1994). In this example, both populations of faults (A and B) respond to a positive stress step at t = 0, and then population A (red) experiences a second positive stress step at t = 71 days, whereas population B (blue) undergoes a negative stress change also at t = 71 days. The weighted sum of earthquake rates from both populations of fault types (orange) shows the delay in the stress shadow effect. More explicitly, after a positive stress step (population A), the earthquake rate decays by Omori's law, to the background rate after time period, t_a, the aftershock duration [$t_a = a\sigma/\dot{S}_r$, where a is the constitutive parameter in the rate-state equations, σ is the normal stress, and $\dot{S}_r$ is the reference stressing rate]. The recovery time following a negative stress step (population B) has a different form given by, $t_e = t_a exp(a\sigma/\Delta CFS)$, and is longer than

t_a. For seismicity distributions that respond to both $+\Delta CFS$ and $-\Delta CFS$, the difference of the recovery time (after negative stress steps) and the decay time (after positive stress steps) (*i.e.* t_e - t_a) causes an apparent delay in the stress shadow effect, shown by the orange curve in Figure 2.3. Although this concept has been previously proposed by (Mallman and Parsons, 2008; Toda et al., 2012) and shown theoretically by (Dieterich, 1994; Helmstetter and Shaw, 2006; Dieterich, 2007)], here we present perhaps the most definitive observation of a delayed seismic stress shadow effect over all earthquake magnitudes caused by the varied response of different fault types to an applied stress step.

In modeling seismicity rates in regions I, II, and III, a weighted least-squares approach is used to estimate the free parameters of the seismicity rate equations, t_a, $a\sigma$, ΔCFS_p, ΔCFS_n, u, and w (see Appendix section: eqs. 2.4, 2.5, and 2.6). We assume an initially elevated rate of seismicity due to stress changes ($\pm$ 0.2-0.5 MPa) induced by the EMC and an average background seismicity rate of 58 events/year (Region I) and 2.6 events/year (Regions II and III), measured from seismicity that occurred in the Yuha Desert between Jan 1981 and the EMC (Hauksson et al., 2012). Initial $+\Delta CFS$, and $-\Delta CFS$ values for the OCO event are based on those from the ΔCFS models for this event (Figure 2.1a) and are allowed to vary only minimally in the modeling process. The predicted earthquake rates are calculated for each population individually. As in the example in Figure 2.3, the rate is computed for population A assuming a positive stress step at t = 0 and 71 days, the time of the EMC and OCO events, respectively. The rate for population B is computed assuming a positive stress step at t = 0 (EMC) and a negative stress step at 71 days (OCO). Populations A and B are then combined by a weighted sum of the

rate contribution from each population (Figure 2.3; see Appendix for more details). This adds an additional weighting parameter, WF_p for events with $+\Delta CFS$; [it follows that the population of events with $-\Delta CFS$ are given by WF_n = (1-WF_p)]. For Region II, the M_w4 event is also modeled using the same procedure, where a third stress step is added. The best-fitting rate-stateseismicity models for each region and the list of best-fitting parameters are presented in Figure 2.4.

2.2.6 Discussion

The best-fitting seismicity rate models (Figure 2.4) invoke the earthquake rate solutions for logarithmic stressing history in which the stressing rate following the OCO event increases by the logarithm of time (Methods section; eqs. 2.6). Continuing time-dependent post-seismic deformation is evident from the analysis of four interoferograms collected between 16 April and 8 October 2010 (Supplementary Figure 6; C. Rollins personal communication) that is concentrated along the OCO and east branch of the Laguna Salada fault and that increases with time. Here, we compute the rate given a logarithmic stressing history that begins at the time of the OCO event through the duration of the computation. Therefore, these modeled earthquake rates (Figure 2.4) do not recover to background seismicity rates. Eq. 2.6 (in Methods) incorporates the effect of post-seismic deformation mechanisms such as afterslip, poroelastic rebound, or viscoelastic relaxation that elevate aftershock production on logarithmic time scales (Kirby and Kronenberg, 1987; Freed and Lin, 1998; Peltzer et al., 1998; Freed and Lin, 2002; Hearn et al., 2002; Perfettini and Avouac, 2004). In a natural system, logarithmic stressing conditions may arise from

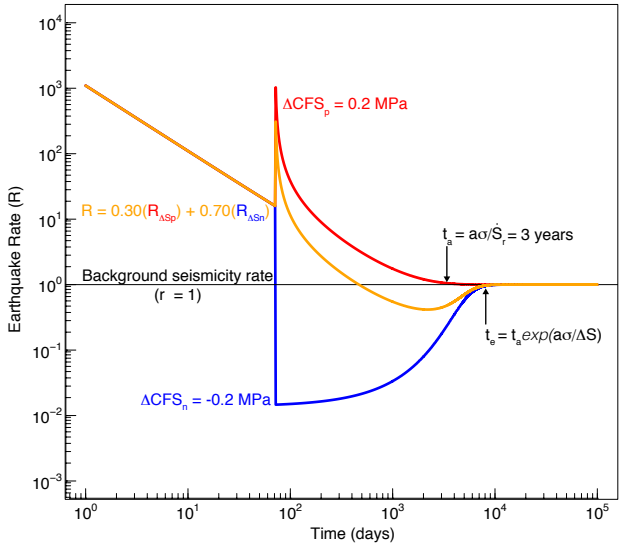

Figure 2.3: Seismicity rate model for a +0.5 MPa stress step at t = 0, followed by either a +0.2 MPa (red) or -0.2 MPa (blue) stress step at t = 71 days. Seismicity rate for a negative stress step (blue) recovers to background rates at time t_e, significantly longer than t_a, the aftershock duration following a positive stress step (red). The delayed stress shadow effect on seismicity rates arises when two populations with different fault types experience stress steps of opposite sign. The weighted sum of the earthquake rates for both populations is given by the orange curve.

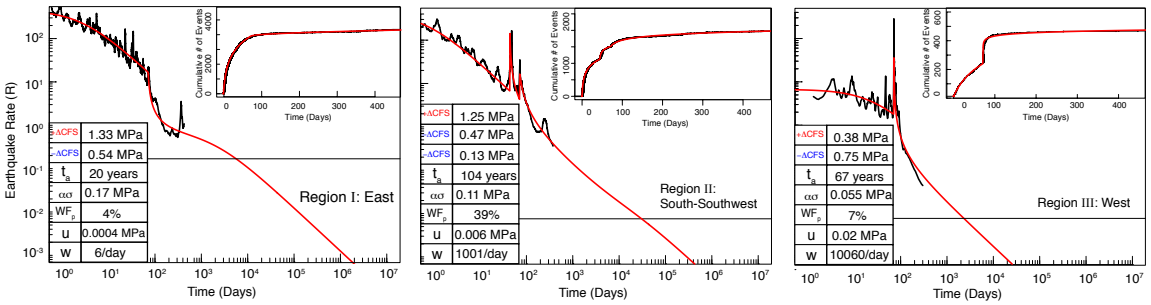

Figure 2.4: Seismicity rate, cumulative number of events, and best-fitting least-squares model in the western Yuha Desert. Inset lists the best-fitting model parameters. Inset lists the best-fitting model parameters. The modeled rate shows the delayed shutdown effect that results when a seismicity distribution is generated by earthquakes on faults of various orientation with a stressing rate that decays by the logarithm of time. Models with logarithmic stressing rates after OCO fit the observed seismicity than models with linear stressing rates or those with a step-like increase in stressing rate following OCO.

afterslip on the deep creeping extensions of the fault that ruptured during an earthquake. Application of logarithmic stressing conditions following a stress step may approximate deep bulk viscoelastic deformation near the earthquake rupture. Such logarithmic stressing conditions dominate at short times following a mainshock and the seismicity rate tends toward zero as post-seismic deformation continues to reduce stress. However, at long enough times, tectonic stresses overcome the post-seismic signal and seismicity rates begin to recover to background levels. In these cases, the time to recovery may be significantly longer than for linear stressing histories where rates return to background levels after a characteristic time, t_e. Models with logarithmic stressing histories outperform those with simpler linear stressing histories (Eq. 2.5), resulting in RMS residuals that are $\sim$20% lower. Furthermore, one can approximate logarithmic stressing histories, to the first-order, with a step-like increase in stressing rate coincident with a stress step. This approach results in model fits with RMS residuals that are $\sim 25\%$ higher than those with log stressing (Supplementary Figure 7).

2.2.7 Conclusion

In conclusion, we demonstrate the influence of static stress changes on the time-dependent rate of aftershock activity. The EMC earthquake induced positive static stress changes at the northern end of the rupture in the Yuha Desert California. Static stress changes led to increased seismicity in this region that was perturbed 71 days later by the M5.7 Ocotillo aftershock, which provides an ideal scenario to study the effects of static stress changes on earthquake rates in an area of complex faulting. An instantaneous seismicity rate increase is observed at the time of the M5.7 Ocotillo earthquake that correlates with Coulomb stress triggering zones in Region II. Furthermore, the rate of seismicity abruptly

decreases in regions I and II, beyond the natural Omori decay following the EMC. This shutdown of seismicity is consistent with Coulomb failure theory as it occurs in a stress shadow region. In Region III, the sudden increase in seismicity rate is followed by a decline $\sim$23 days later. We demonstrate that a modeling approach which incorporates ΔCFS with the rate-stateformulation is able to model post-seismic earthquake rates with considerable fidelity when assuming two populations of faults are simultaneously active and experience a stress change of opposite sign. The successful identification of a delay in the stress shadow effect suggests that observations of seismicity rate decreases in regions of negative stress change are rare because the stress shadow effect does not occur instantly, but may be delayed by weeks to months. The results presented here overcome the principal argument against static stress analysis, by demonstrating a decreased rate of seismicity in stress shadowed regions. Our analysis suggests that future investigation of seismicity rate changes in response to static stress changes should not be limited to ΔCFS on a single fault orientation or short time scales following the stress perturbation.

2.2.8 Appendix A: Seismicity Rate Calculation Methods

Earthquake rate equations describe the evolution of seismicity rate as a function of stressing history (Dieterich, 1994, 2007). The instantaneous earthquake rate due to a step change in CFS is given by,

$$R = R_0 \exp\left(\frac{\Delta CFS}{a\sigma}\right) \tag{2.4}$$

where R_0 is the steady-state background seismicity rate, a is the rate-state con-

stitutive parameter, and σ is the normal stress. The earthquake rate between stress steps, assuming a constant stressing rate is given by,

$$R(t) = \frac{1}{\frac{\eta}{\dot{S}} + \left(\frac{1}{r} - \frac{\eta}{\dot{S}}\right) \exp\left(\frac{-\dot{S}t}{a\sigma}\right)} \tag{2.5}$$

where η is the ratio of the reference stressing rate, $\dot{S}_r$ to the reference background seismicity rate, r; (*i.e.* $\eta = \dot{S}_r/\mathrm{r}$).

Following some earthquakes, post-seismic deformation mechanisms such as afterslip, poroelastic rebound, or viscoelastic relaxation such as those observed after OCO (Supplementary Figure 6) elevate aftershock production on logarithmic time scales. In the presence of post-seismic deformation, earthquake rates are related to logarithmic stressing histories such that,

$$R(t) = \frac{1}{R_0}(wt+1)^{-m} + \frac{\eta(wt+1) - (wt+1)^{-m})}{aw\sigma(m+1)^{-1}} \tag{2.6}$$

where $\mathrm{m} = u/\mathrm{a}\sigma$, u has units of stress, and w has units of 1/time. Equations 2.4, 2.5, and 2.6 can be combined to predict the observed aftershock activity given complex stressing histories.

To compute the weighted sum of earthquake rates (Figure 2.3; orange curve), we assume the stress changes associated with the EMC are positive in all regions and compute the rate as a function of time as follows: 1) compute rate (R1) assuming the stress step at the time of OCO is positive (e.g. +0.2 MPa), 2) compute rate (R2) assuming the stress step at the time of OCO equal in magnitude and opposite in sign (e.g. -0.2 MPa), and 3) find the sum of the weighted rates: R = W_p*R1 and [1-W$-p$]*R2 (W_p = Weight for

events with positive stress change). For solutions from EQ. 2.6, u is treated in the same manner as the stress step at the time of OCO; $+u$ is used to compute R1 and -u is used to compute R2. In Region II, the stress step due to the M4 event that occurs 44 days after the EMC mainshock, is treated similar to that of the OCO event such that the stress steps from both this event and the OCO are positive when computing R1 and both are negative when computing R2. The same [1-W_p] weighting factor is used for both stress steps when determining the weighted sum of the R1 and R2 earthquake rate distributions.

2.2.9 Supporting Information for "Delayed Seismicity Rate Changes Controlled by Static Stress Transfer"

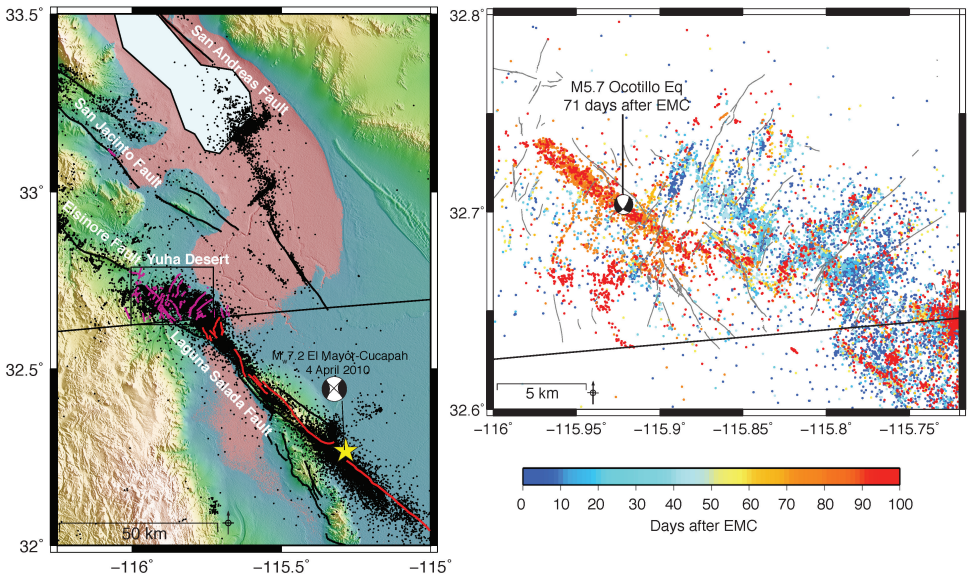

Figure 2.5: El Mayor-Cucapah mainshock rupture and aftershocks. Left) Surface rupture [red and magenta lines ((Fletcher et al., 2010))] of the EMC (yellow star and focal mechanism) along with aftershocks and regional seismicity that occurred through December 2010 (Hauksson et al., 2012). Right) Aftershocks of the EMC in the Yuha Desert region colored by time since the mainshock. The Ocotillo epicenter is shown by the focal mechanism. Early seismic activity occurs in the eastern Yuha Desert, while the majority of seismicity after Ocotillo occurs along that fault plane and to the SW in the triggering zone.

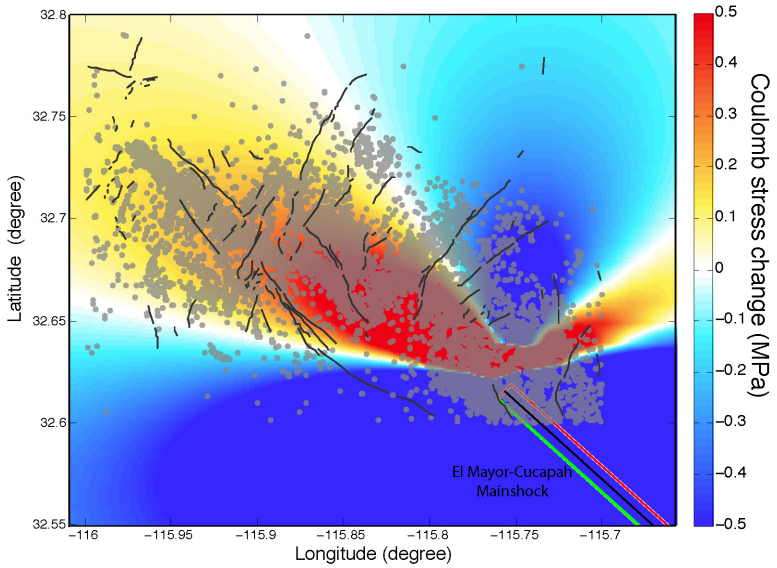

Figure 2.6: ΔCFS from the EMC event on the Yuha Desert. The EMC source fault is planar with an average tapered slip of 2.5 m. Seismicity (grey) after the EMC through December 2013.

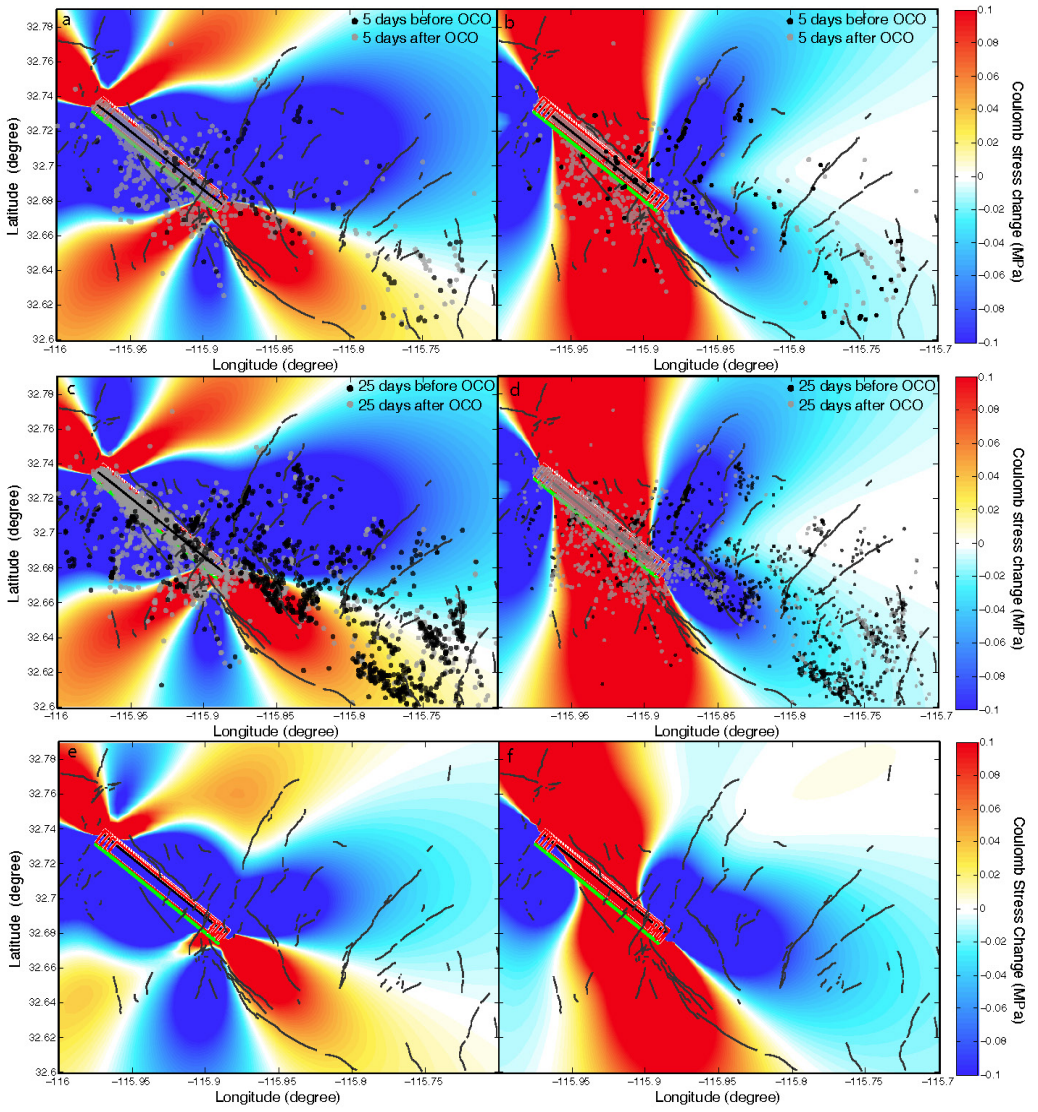

Figure 2.7: ΔCFS results for various receiver fault orientations. Left) Left-lateral receiver faults. Right) Normal receiver faults. Top and Middle Rows) Receiver fault orientation is that of Figure 1 (main article), but showing seismicity 5 and 25 days before (black) and after (grey) the Ocotillo event. Bottom Row) Receiver fault orientation from the mean of the left-lateral strike slip and normal faulting focal mechanisms.

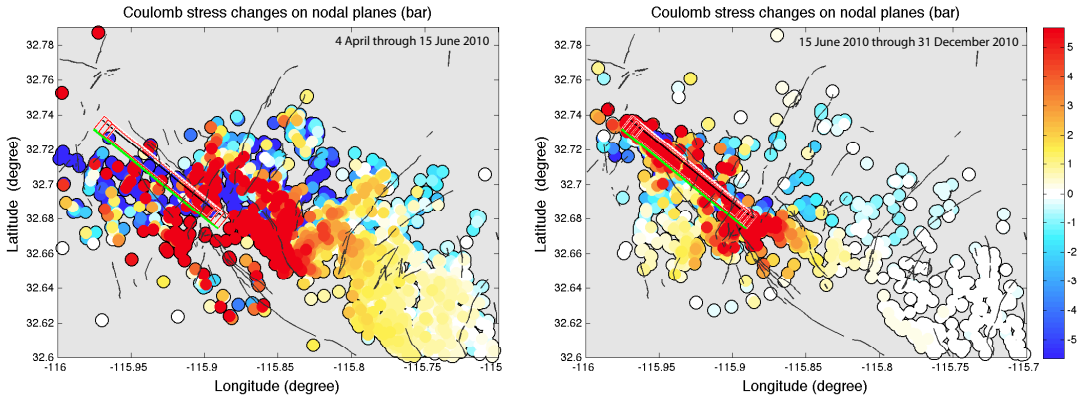

Figure 2.8: Maximum $|\Delta CFS|$ computed on either nodal plane of the focal mechanism. Left) Events that occurred between the EMC and Ocotillo events. Right) Events that occurred following the OCO earthquake through June 2011. Note predominately positive stress changes on events in the south-southwest and eastern Yuha Desert after the EMC and before the Ocotillo event (left panel), the negative stress changes in the eastern Yuha Desert, and the mix of positive and negative stress changes on events in the western Yuha Desert after OCO (right panel).

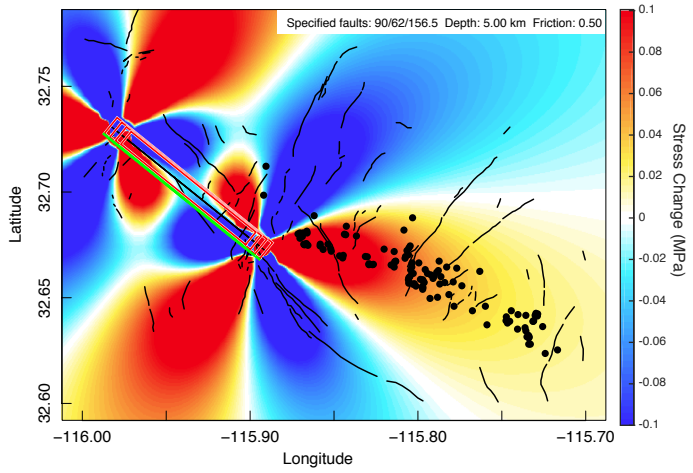

Figure 2.9: Coulomb stress change model assuming the OCO source and east-trending right-lateral receiver faults (strike = 90°, dip = 62°, and rake = 156.5°). The receiver fault orientation is based on the average focal mechanism of strike-slip events that occur in the stress shadowed Region I, but that have $+\Delta CFS$. All events but three events occur in the triggering zone for these receiver faults.

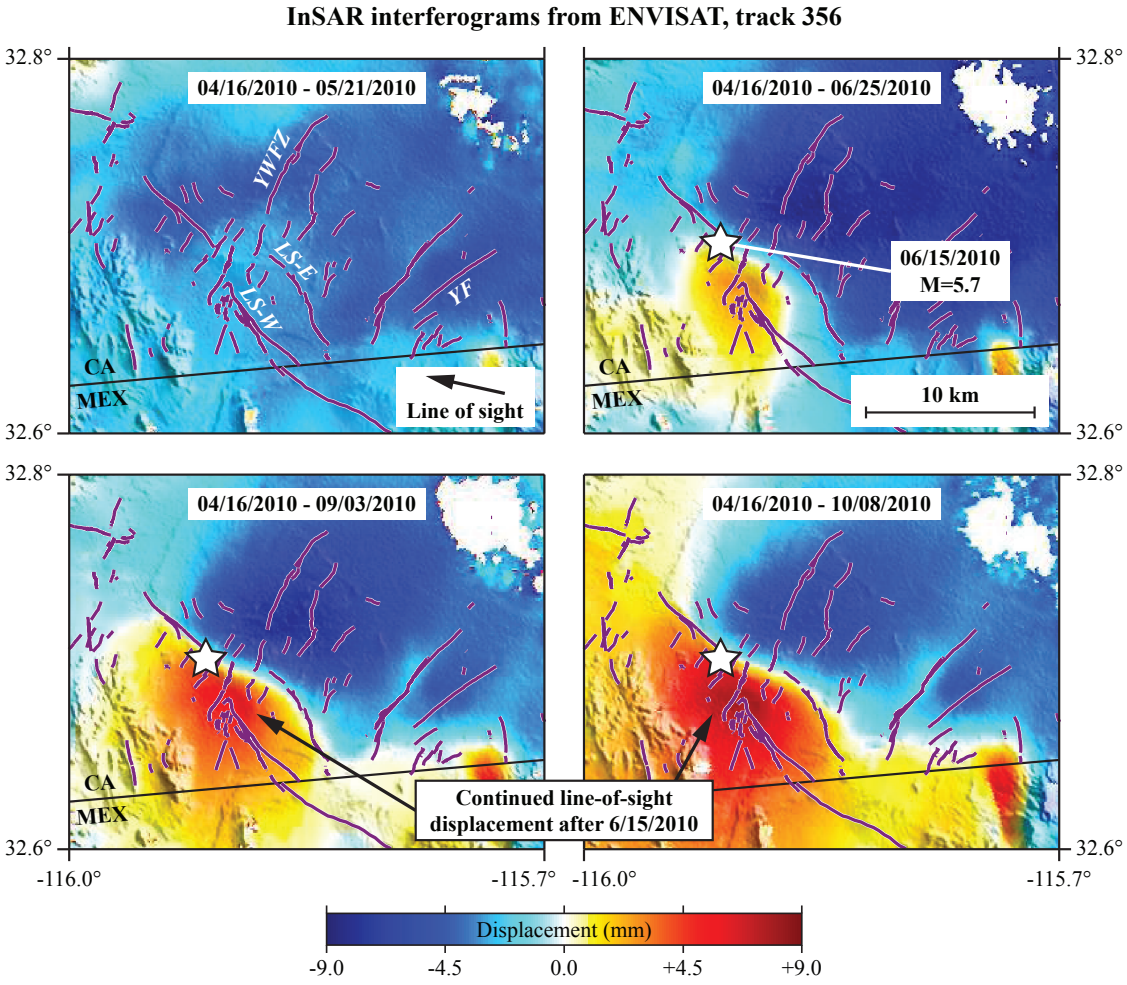

Figure 2.10: Interferograms of surface displacement constructed from ENVISAT SAR images (descending track 356) show right-lateral surface displacement aligned with the OCO source fault and the east branch of the Laguna Salada Fault both during and following the OCO earthquake. Pairs of dates indicated on each figure are the dates of the first and second image capture used to make the interferogram, respectively. LS-W: Laguna Salada Fault, west branch; LS-E: Laguna Salada Fault, east branch; YWFZ: Yuha Well Fault Zone; YF: Yuha Fault. (C. Rollins personal communication September 2015)

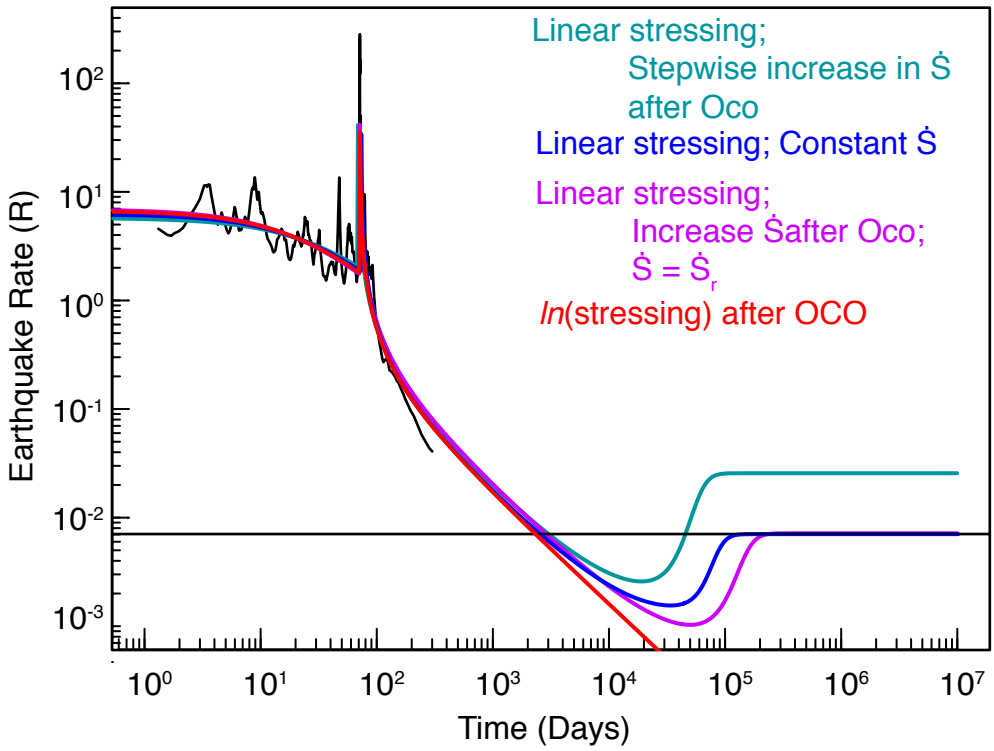

Figure 2.11: Rate-state earthquake models with linear and log stressing histories. Red curve shows best fitting model with logarithmic stressing presented in the main text for comparison. All other models incorporate linear stressing histories with various modifications. Blue curve shows the simplest rate-and-state model where the stressing rate, $\dot{S}$,is constant through time. The teal curve incorporates linear stressing, but also a step-like increase in the stressing rate at the time of the OCO event. This model recovers to a higher background rate due to the increase in $\dot{S}$. Lastly, the model shown in purple requires $\dot{S} = \dot{S}_r$, therefore the model recovers to the background seismicity rate prior to the EMC event. The minimum RMS residuals for these models are 18%, 25%, and 10% higher than that with log stressing for the blue, teal, and purple curves, respectively.

Part III

Numerical Earthquake Simulations of Fault Interaction

Chapter 3

3D Multi-Cycle Simulations of Earthquake Rupture Across Fault Stepovers

3.1 Abstract

Understanding earthquake rupture behavior along offset *en echelon* faults is critically important to properly quantify seismic hazards because earthquake rupture length (and associated parameters like earthquake moment and recurrence times) depends on whether a rupture jumps across or is arrested at fault stepovers. Previous numerical simulations of single event rupture propagation across fault stepovers have typically used homogeneous fault initial stresses. However, earthquake simulations are particularly sensitive to the initial stress conditions which, in the real earth, continuously evolve over multi-

ple earthquake cycles due to tectonic stressing, fault interactions, pore-fluid perturbations, and viscoelastic relaxation. Here, we investigate spontaneous rupture propagation across fault stepovers in multi-event simulations with evolved heterogeneous stresses. We employ the 3D, physics-based earthquake simulator, RSQSim, and the fully dynamic finite element code, FaultMod, to explore the effects of initial stresses on rupture propagation in both single-event simulations with homogeneous stresses and multi-event simulations with evolved stresses. Results indicate: 1) In single-event simulations with homogeneous initial stress conditions, the spatial pattern of re-nucleation locations on the receiver fault from RSQSim compare favorably with previous results and with FaultMod simulations, albeit with slightly shorter jump distances, 2) In multi-event simulations with heterogeneous evolved initial stresses, re-nucleation locations are controlled by the stress heterogeneity on the receiver fault, 3) Ruptures with evolved stresses occur at low stresses that preclude large rupture jumps and supershear ruptures, and 4) Rate- and state-dependent friction leads to time-dependent delayed nucleation effects where rupture across stepovers > 1 km are delayed by minutes to years.

3.2 Introduction

Assessments of earthquake hazards critically depend on how faults interact and how their activity varies in regions of geometric complexity, such as discontinuous fault offsets along *en echelon* strands. Successful earthquake rupture across a fault stepover increases the final rupture length and thus seismic moment. Understanding rupture behavior near fault stepovers is especially important in strike-slip faulting environments where the

magnitude of an earthquake predominately scales with rupture length. For example, the 1992 M_w7.3 Landers and 2010 M_w7.2 El Mayor-Cucapah earthquakes, two of the largest events in/near southern California 100 years, ruptured multiple *en echelon* fault strands and propagated through fault stepovers as mapped at the surface with rupture lengths of 75 km and 120 km, respectively (Sieh et al., 1993; Hauksson, 1994; Fletcher et al., 2014). Alternatively, rupture may be arrested at stepovers, resulting in shorter surface ruptures and thus smaller magnitudes, as observed after the M_w 6.4 1969 Borrego Mountain earthquake. This event ruptured a total 31 km of the Coyote Creek portion of the San Jacinto Fault, in three segments separated by <1.5 km compressional and extensional offsets (Sibson, 1986b). The northern end of the rupture terminated at 2.5 km compressional step-over between the northern Coyote Creek fault and a 7 km extensional step-over between the Clark fault (Wesnousky, 2006).

Studies of earthquake ruptures in *en echelon* fault systems include both observations of moderate to large earthquakes (e.g. Burchfiel and Stewart (1966); Crowell (1974); Sibson (1986a); Wesnousky (1988); Sieh et al. (1993); Lettis et al. (2002); Wesnousky (2006); Fletcher et al. (2014)) and dynamic rupture modeling (e.g. Andrews (1976); Segall and Pollard (1980); Harris and Day (1993, 1999); Duan and Oglesby (2006); Oglesby (2008); Lozos et al. (2012, 2014, 2015); Ryan and Oglesby (2014)). Wesnousky (2006) documented the end points of rupture for 22 historic strike-slip earthquakes ranging in magnitude from 6.1 $\leq M_w \leq$ 7.9. Of these events, 14 ruptured across compressional or extensional stepovers 3 to 4 km wide.

These maximum "jumpablee" distances appear to be consistent with the results

of 2D finite-difference simulations of earthquakes on planar faults with homogeneous initial stresses Harris and Day (1993). In rupture dynamics, initial stresses are often characterized in terms of the parameter, S, which decreases with increasing initial stress, and is defined as;

$$S = \frac{\tau_y - \tau_0}{\tau_0 - \tau_f} \tag{3.1}$$

where τ_y is the yield stress, τ_0 is the initial shear stress and τ_f is the dynamic sliding (frictional) stress (Andrews, 1976; Das and Aki, 1977). For 2D and 3D faults with homogeneous initial stresses, rupture propagation can transitions to supershear speeds when $S < 1.63$ and $S < 1.19$, respectively (Das and Aki, 1977; Dunham, 2007). Ruptures that propagate at supershear speeds are more energetic and tend to jump larger offsets (Harris and Day, 1993). Partially due to this subshear/supershear difference, the maximum jump distance in numerical simulations is highly dependent upon the initial stress conditions. For example, in 2D simulations earthquake ruptures can successfully jump stepovers 3 km and 5 km wide, for compressional and extensional offsets, respectively, when the initial stresses are high and well into the supershear regime ($S = 0.49$) (Harris and Day, 1993). However, the maximum jump distance decreases to 0.5 and 1km in compressional and extensional offsets, respectively, when initial stresses are low ($S = 1.65$) and in the sub-shear wave speed regime (Harris and Day, 1993). Dynamic rupture simulations in 3D further reduce the maximum jumpable distance to 0.75 km with moderate initial stresses (S= 1.61) that result in sub-shear wave speed ruptures (Harris and Day, 1999).

Numerical simulations of earthquake rupture propagation require *a priori* knowledge of fault geometry, material properties, fault friction, and initial stress conditions (Har-

ris, 2004). Each of these parameters may imprint its own signature on the earthquake process. For example, fault geometry can either aid or hinder rupture propagation (Sibson, 1986a; Wesnousky, 2006), bi-material interfaces along fault may lead to a preferred rupture propagation direction (Andrews and Ben-Zion, 1997), and differences in frictional properties influence modes of fault slip (e.g. stable-sliding versus stick-slip (Gu et al., 1984; Dieterich, 1992, 1994)). There are currently methods available to approximate all parameters except for the initial stress conditions (Harris, 2004). The geometry of faults can be mapped at the surface or with seismological methods similar to those used to measure the material properties of fault zones and the surrounding media (e.g. elastic constants and wave speeds determined through active and/or passive geophysical studies) (Bedrosian et al., 2002; Langenheim et al., 2004; Fay and Humphreys, 2005; Allam and Ben-Zion, 2012; Kroll et al., 2013). Frictional formulations used in rupture jump studies range from simple Coulomb failure with slip-weakening friction where friction decreases with slip distance to the rate- and state-dependent frictional formulation in which frictional sliding is dependent upon the slip rate as well as sliding history (Dieterich, 1978, 1979). Here, we use rate-state friction with laboratory-constrained values of the constitutive parameters including the characteristic slip distance (Dieterich, 1978). The *in situ* stresses on faults are the least understood of the initial conditions required for a numerical simulation, as they can not be measured directly. To further complicate matters, the stress field is certainly heterogeneous and continuously evolving due to the interaction of several sources including tectonic loading, fault geometry, fault interaction from co-seismic slip, fault creep, and post-seismic deformation mechanisms such as afterslip, viscoelastic relaxation, and pore-fluid diffusion.

Multi-cycle earthquake simulators provide a direct means for calculating the heterogeneous stress field at the onset of earthquake rupture and its event-to-event variability. Earthquake simulators use the physics of fault rupture processes and stress transfer in complex fault systems to simulate earthquake sequences over many earthquake cycles ($> 10^6$ years) (Tullis et al., 2012). Stresses evolve over all elements in the fault system due to fault interaction and the various external loading sources such as tectonic and the post-seismic deformation processes listed above. Thus, earthquake simulators can be employed to investigate the effects of evolved heterogeneous stresses on rupture propagation. While many previous numerical simulation studies have examined the effects of fault geometry, frictional, and material parameters on earthquake occurrence and fault interaction (cited above), few studies have investigated the effect of heterogeneous initial stresses on rupture propagation across offset *en echelon* faults (Duan and Oglesby, 2006; Lozos et al., 2015).

Here, we use the 3D, quasi-dyanmic boundary element earthquake simulator, RSQSim, and the fully dynamic finite element code, FaultMod, to explore how earthquake ruptures propagate along stepping faults in two circumstances, 1) artificially nucleated, single-event simulations with homogeneous initial stresses, but different frictional formulations, and 2) heterogeneous, evolved initial stresses from multi-cycle event simulations with rate- and state-dependent friction. Results from both studies are compared with the results of Harris and Day (1993). We find that RSQSim results are similar to FaultMod solutions for the single-event simulations, which suggests that RSQSim is a robust model capable of producing results similar to those of the fully dynamic model, in spite of the approximations of the governing equations. Multi-cycle event simulations show that the heterogeneous

initial conditions strongly affect rupture propagation and the ability of ruptures to jump. This includes quantification of the probability of successful rupture jumps as a function of overlap/underlap and offset distances, and effects of delayed rupture jumps resulting from time-dependent nucleation inherent to rate-state friction.

3.3 Methods

RSQSim is a 3D, quasi-dynamic boundary element earthquake simulator that employs the rate- and state-dependent frictional formulation. RSQSim is capable of simulating multiple types of earthquake slip phenomena including stick-slip, slow slip, tremor, creep, and afterslip and generates synthetic catalogs of $> 10^6$ earthquakes with characteristics similar to observed seismicity (Richards-Dinger and Dieterich, 2012; Tullis et al., 2012). Single-event RSQSim results have been validated against those of fully dynamic rupture models to ensure accurate implementation of computational approximations to elastodynamics (see Appendix) (Dieterich and Richards-Dinger, 2010; Richards-Dinger and Dieterich, 2012). For example, comparisons between RSQSim and Dyna3D show similar time histories, stress changes, and total slips for single-event ruptures on a planar fault. See Section 1.3 for details on the modeling method.

FaultMod is a 3D, fully dynamic, finite element, single-event earthquake rupture code (Barall, 2008, 2009) that calculates slip speeds, rupture velocity, and slip evolution at short time intervals during an event. FaultMod incorporates either slip-weakening (Ida, 1972; Palmer and Rice, 1973; Andrews, 1976) or rate- and state-dependent friction and is driven by pre-stress conditions on the fault (either homogeneous or externally derived

heterogeneous conditions). Earthquakes are artificially nucleated by either reducing the yield stress for slip-weakening friction, or the value of the state parameter (θ) for models that implement rate-state friction. For more details about FaultMod, we refer the reader to the following articles for a more complete discussion of the treatment of the governing equations, numerical method, validation, and applications: Harris et al. (2004, 2009); Barall (2008, 2009); Lozos et al. (2012, 2013, 2014, 2015); Ryan and Oglesby (2014). Simulations in this study assume a linearly elastic, homogeneous, isotropic solid described by the P- and S- wave speeds and density.

3.4 Results

In this study, we focus on the effects of initial stresses on rupture jumps at fault stepovers under two conditions. We first examine single-event rupture jump simulations with homogeneous initial stresses. In this phase of the study, we compare results from RSQSim with that of FaultMod to quantify possible differences in the simulation methods. In the second phase, we examine rupture jumps on faults with heterogeneous initial stresses that evolve over many earthquake cycles. These RSQSim simulations contain more than 3 million earthquakes that occur over 100,000 years. We examine the distribution of slip along strike, maximum slip per event, earthquake magnitude, and re-nucleation location on the receiver fault (*i.e.* the fault onto which rupture jumps) for events that rupture across the stepover.

3.4.1 Single-Event Simulations

Single-event simulations impose homogeneous initial stress conditions on two planar, 30 by 20 km, left-lateral strike-slip faults with 0.01 km^2 elements. The faults have a 10 km overlap, and offsets that vary from 0.1 to 10 km (Figure 3.1) for both compressional and extensional stepovers.

We prescribe the following uniform values of shear stress, normal stress, and seismic slip rate (slip rate is only prescribed for RSQSim simulations), respectively: 29.38 MPa, 60 MPa, and 0.72 m/s. Initial stresses and stress drop were matched such that the rupture stress parameter (Equation 3.1), $S \approx 1.42$. The FaultMod simulations use the slip-weakening friction law [which produces similar results in 2D dynamic rupture simulations of fault stepovers with similar fracture energies (Ryan and Oglesby, 2014)], RSQSim uses the rate- and state-dependent law including the effects of variable normal stress on the state variable given by,

$$\mu = \mu_0 + a \ln \left(\frac{V}{V^*} \right) + b \ln \left(\frac{V^* \theta}{D_c} \right), \tag{3.2}$$

where a and b are the constitutive parameters that describe the material, D_c is the characteristic slip distance over which the state variable (θ) evolves, τ and σ are the shear and normal stresses, μ_0 is the steady-state coefficient of friction at the reference slip speed, V^*, and V is slip speed during frictional sliding (Dieterich, 1979; Ruina, 1980, 1983). The strength of the effects of variable normal stress on the state variable are controlled by the parameter α (where α ranges from 0 to the nominal coefficient of friction, μ_0) in the state-variable evolution equation of the rate-state aging law (Linker and Dieterich, 1992)

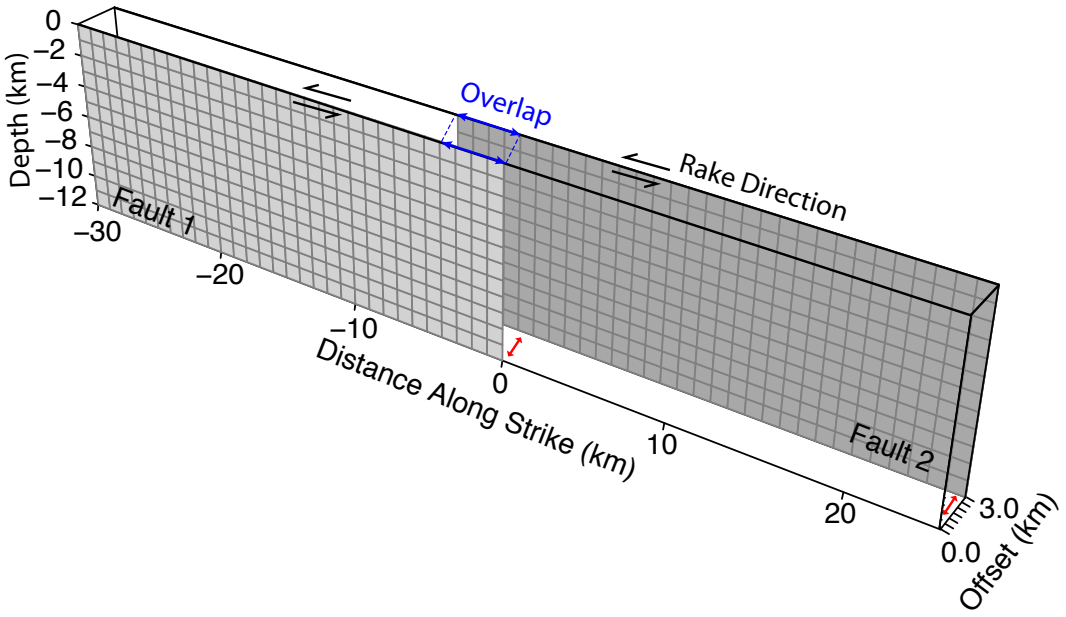

Figure 3.1: Example of a 3 km extensional offset of left-lateral faults used in these simulations. Fault 1 is held fixed and fault 2 is offset at various distances to form either a compressional or extensional step between the faults, with negative offsets defined to be compressional. We define the offset to be the perpendicular distance between the faults along strike. The fault overlap is the along-strike distance between the ends of both faults in the stepover region, where negative values indicate underlaps (*i.e.* gaps in faults along strike.

given by,

$$\dot{\theta} = 1 - \frac{\theta V}{D_c} - \alpha \left(\frac{\theta \dot{\sigma}}{b\sigma} \right). \tag{3.3}$$

Default values of the rate-state parameters for RSQSim are as listed in table 1.1. Note that the characteristic slip distance, D_c, in the rate- and state-dependent frictional formulation and the slip weakening distance, d_0, are the only non-constant parameters between RSQSim and FaultMod. Because the critical crack length (L_c in section 1.3) for the event nucleation scales with D_c and d_0, the size of the nucleation patch also scales with D_c and d_0 in RSQSim and FaultMod, respectively. Event nucleation in RSQSim must take place within a single element, however, the nucleation process is resolved over several elements in FaultMod. As a general rule for dynamic simulations each element must be $\sim \frac{1}{10} L_c$. Hence, vastly different values of D_c and d_0 are required because it would be too computationally expensive to resolve the nucleation process with laboratory values of D_c. Consequently, in these simulations D_c and d_0 can not be directly scaled and differ by several orders of magnitude (i.e 10 μm in RSQSim and $d_0 = 50$ cm in FaultMod) (see (Ryan and Oglesby, 2014) for further explanation). Although nucleation can occur spontaneously in RSQSim, we artificially nucleate events in both models in a circular region with 3 km radius by reducing the state-parameter in RSQSim and the yield stress in FaultMod such that rupture occurs instantaneously.

Simulation results of single earthquakes with prescribed homogeneous initial stresses are qualitatively similar between RSQSim and FaultMod. Figures 3.2(a,b) show the distribution of slip for one event that successfully jumps a 1 km compressional stepover in both

the RSQSim (Figure 3.2a) and FaultMod (Figure 3.2b) simulations. The pattern of slip in each model is qualitatively similar, with maximum slip occurring above the nucleation region of the source fault, and near the re-nucleation location on the receiver fault. Profiles of slip averaged over every down-dip column of elements along strike [inset Figure 3.2(a & b)] also display similar, roughly elliptical-shaped slip distributions. Slip is inhibited in the overlapping region in both simulations, but the summed slip across both segments creates the elliptical slip profile similar to that expected by a single through-going rupture. In this example, the maximum slip is 5.5 m and 7.2 m for RSQSim and FaultMod, respectively. Average slip, and thus earthquake magnitudes, are consistently higher, even for events with the same average stress drop, in FaultMod than RSQSim; in this example resulting in a M_w7.4 for FaultMod and M_w7.3 for RSQSim. Larger values of average slip may be due to differences in the frictional formulation, the characteristic slip distance, dynamic overshoot (in the dynamic model) and dynamic stress changes that RSQSim does not consider with the quasi-static formulation. The rupture time contours show that rupture propagates faster along strike than down-dip in both models and suggest faster rupture speed is in RSQSim than FaultMod. Propagation along the receiver fault differs somewhat between the models; rupture in the RSQSim event propagates slowly in the overlapping region, before it begins to rupture bilaterally. Receiver fault propagation in the FaultMod simulation fully stops near the overlapping region for a short time, before propagating toward the other end of the fault.

The maximum jumpable distances in the single-event simulations are based on models with low, homogeneous, initial stresses and subshear rupture propagation speeds

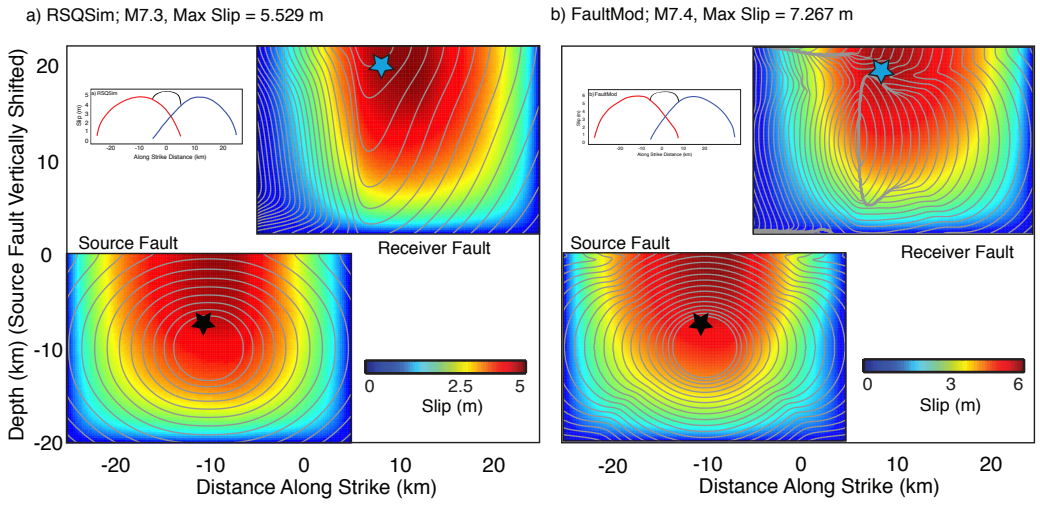

Figure 3.2: Slip distribution for a rupture that jumps across a 1 km compressional stepover from RSQSim (a) and FaultMod (b) for a single-event simulation with homogeneous initial stresses. Ruptures in this simulation were artificially nucleated in the 3 km circular region on the source fault, with the center of the region labeled by the black stars. Contours mark the front of the rupture at 0.2 second intervals and color is slip. In each case, the rupture re-nucleates on the receiver fault spontaneously at the element indicated by the blue star. Inset: slip averaged for every column of elements along strike.

and are consistent with results of several other dynamic models of stepovers using slip-weakening and rate- and state-dependent friction in 2D and 3D (*i.e.* (Harris and Day, 1993; Lozos et al., 2013, 2014; Ryan and Oglesby, 2014)). For $\alpha = 0.25$, the maximum jumpable distance for simulations with RSQSim are larger for compressional offsets than extensional offsets; at 1.9 km and 1.5 km, respectively. When $\alpha = 0$ (*i.e.* normal stress does not affect the state variable θ), ruptures in RSQSim jump 2.1 km offsets for both offset directions. These maximum jump distances from RSQSim are slightly smaller than those from FaultMod simulations where rupture propagated across 2.75 km compressional offsets and 2.25 km extensional offsets, which may be due to dynamic stress transfer or vastly different fracture energies.

The rupture re-nucleation locations on the receiver fault from models with low, homogeneous initial stresses are shown in Figure 3.3, for both compressional and extensional stepovers. This figure is comparable to that of results reported by Harris and Day (1993) (their Figures 6 and 7), however, note that their results are for 2D models with homogeneous initial stresses with $S = 0.49$ and 1.65 for their Figures 6 and 7, respectively. RSQSim results show a systematic moveout of re-nucleation locations similar to Harris and Day (1993) (their Figure 6), where re-nucleation locations move farther away from the end of the source fault faster as the offset increases for compressional stepovers and closer to the end of the receiver fault in the overlapping region for as offset increases for extensional stepovers. The re-nucleation locations in FaultMod simulations fall within the scatter of the RSQSim results.

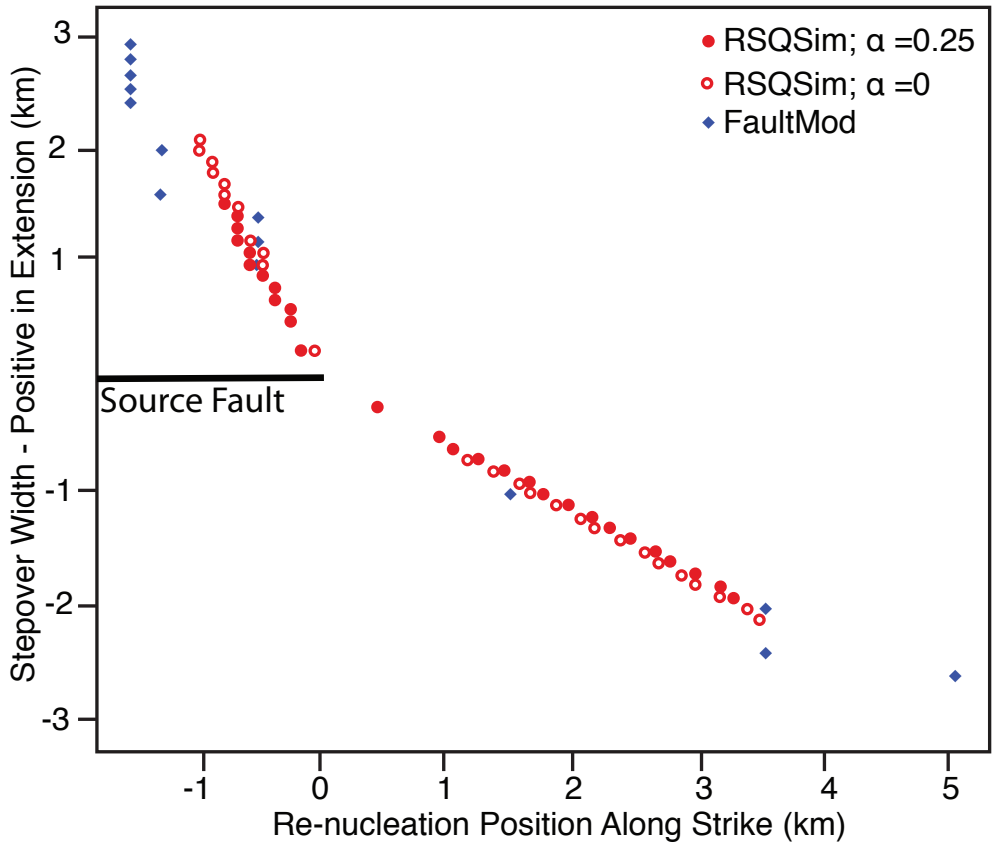

Figure 3.3: Re-nucleation locations on the receiver fault relative to the end of the source fault [comparable to Figure 6 from Harris and Day (1993)] from the single-event simulations with homogeneous initial stresses with RSQSim (red) and FaultMod (Blue). Solid red symbols are for simulations in RSQSim using a non-zero α which accounts for the effects of variable normal stress on the evolution of the state parameter, θ

.

3.4.2 Multi-Cycle Event Simulations

Multi-cycle earthquake simulators provide a means to estimate the continuously evolving, heterogeneous stress field along faults that can not be measured *in situ*. We use RSQSim to investigate the effects of a heterogeneous initial stress field on rupture propagation and specifically the ability to jump stepovers in 100,000 year synthetic catalogs of $>10^6$ earthquakes. In this section, we simulate rupture along the same fault geometry described in section 3.4.1, except that both faults extend 50 km along strike and 15 km with and are discritized with 1 km^2 elements (RSQSim) and 0.0625 km^2 node spacing (FaultMod), for offsets between 0.2 and 3 km and overlaps between -10 and 5 km (positive for underlapping models). We employ the rate- and state-dependent frictional formulation in both numerical simulation methods, but again with different values of D_c: 10 μm and 0.4 cm in RSQSim and FaultMod, respectively. All other initial parameter values of the rate-and state- formulation are listed in Table 1.1. Stresses in RSQSim are considered to be stably "evolved" after the model "spin-up" period, which consists of at least one full earthquake cycle where all elements have slipped at lease once ($\approx$ 1000 years in these models). After the spin-up period, the fluctuating stresses are a result of both fault interactions and backslip loading. The long-term average slip rate used for the backslip calculation in RSQSim is 5 mm/yr on all fault elements outside of the overlap region, and tapers linearly within the overlap region such that the across-strike sum of the slip rates on the two faults is 5 mm/yr everywhere.

We compile sub-catalogs of events that successfully propagate across the fault stepover for all simulations. We develop a set of criteria to automatically track the number

of successful versus failed jumps in 208 catalogs that are 100,000 years long, for 16 offsets (*i.e.* ±250 m, ±500m , ±1000 m, ±1250 m, ±1500 m, ±1750 m, ±2000 m, and ±3000 m; positive for extensional stepovers) and 13 over or underlaps (*i.e.* 0, ±1 km, ±2 km, ±3 km, ±4 km, ±5 km, -7 km, and -10 km; positive values indicate an underlap). Events are considered successful jumps if they meet the following set of criteria:

1. Source fault rupture area $\geq$ (fault width)^2.
2. 75% of the elements in the column adjacent to (but just outside) the overlapping region ruptures on the source fault.
3. Rupture area on receiver fault also exceeds (fault width)^2.

A rupture is considered a failed jump if conditions 1 and 2 are met but condition 3 is not. This automated method captures all but 1% of events that jump at a given offset and eliminates the need for visual inspection of 208 simulated catalogs with more than 3 million events in each (see Supplementary Figure 1 for more details).

Next, we select a representative event from the sub-catalog of jumping ruptures to compare events with fully dynamic simulations. We use the evolved parameter values just before the rupture in RSQSim as the initial conditions for a single-event rupture simulation with FaultMod. Parameter values include the evolved stresses, τ and σ, and the state variable, θ. An example of such evolved heterogeneous stresses expressed as the ratio of shear to normal stress before a successful jump is shown in Figure 3.4. Where possible, we use the same parameters for FaultMod simulations as we used for the RSQSim simulation, however, there are two exceptions. First, because the much larger D_c values lead to much greater fracture energy in the FaultMod simulations, ruptures cannot propagate unless the

heterogeneous shear stresses are everywhere increased by 10%. And secondly, the companion event simulated in FaultMod is artificially nucleated by reducing θ in a circular region with a 3 km radius that contains the hypocenter of the corresponding RSQSim event, whereas events in RSQSim nucleate spontaneously.

Synthetic earthquake catalogs computed with RSQSim that span ∼100,000 years and contain >3 million events for each offset and overlap examined here. The slip distribution for a representative RSQSim event, with a 5 km overlap and 1 km extensional offset, is shown in Figure 3.5a. The corresponding FaultMod event (Figure 3.5b) has a similar qualitatively similar slip distribution and re-nucleation location along strike of the receiver fault. The maximum slip in FaultMod solutions is roughly double that of the companion event from RSQSim, but approximately equal to the maximum slip in the results from both the RSQSim and FaultMod simulations with homogeneous initial stresses (Figure 3.2). This is probably due to the 10% increase in initial shear stress, as well as effects of dynamic stresses due to dynamic wave propagation, which is not accounted for in the RSQSim solution. The higher initial stresses result in higher maximum slip, and therefore seismic moment, magnitude, and stress drop for all ruptures computed with FaultMod. Source fault rupture in both simulations propagates at nearly the same speeds along strike, with slightly faster propagation observed near the edges of the area of maximum slip. This region represents the high stress boundary surrounding a previous $\approx M6.5$ event that occurred in RSQSim prior to the event shown. The 10% increase in shear stress prior to beginning the simulation, causes these elements rupture spontaneously upon start-up of FaultMod simulation and continuously re-rupture throughout the simulation. Again, both models produce roughly

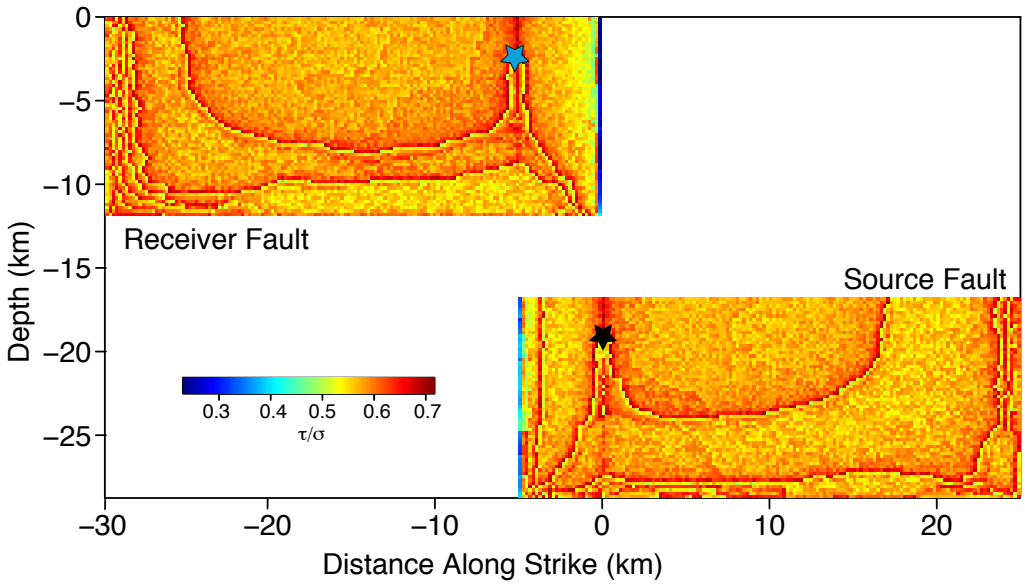

Figure 3.4: Example of the ratio of evolved shear to normal stress after ∼33,000 years, before the event that ruptured the 1 km extensional stepover in Figure 3.5. The future hypocenter and re-nucleation location are indicated by the black and blue stars, respectively.

elliptical slip profiles, however slip in the RSQSim model tapers more severely towards the fault edges [inset Figure 3.5(a,b)].

3.4.3 Rupture Re-nucleation Locations

Next, we investigate how heterogeneous initial stresses affect the location of rupture re-nucleation on the receiver fault for events that are able to propagate across the step. The distribution of re-nucleation locations on the receiver fault (Figure 3.6) are scattered and lack distinct moveout as seen for the single-event simulations in Figure 3.3. However, qualitatively, the mean of all re-nucleation locations for a given offset, tends to be further from the end of the source fault for compressional steps, while it is within the overlapping region and near the end of the source fault for extensional steps. This behavior is similar to

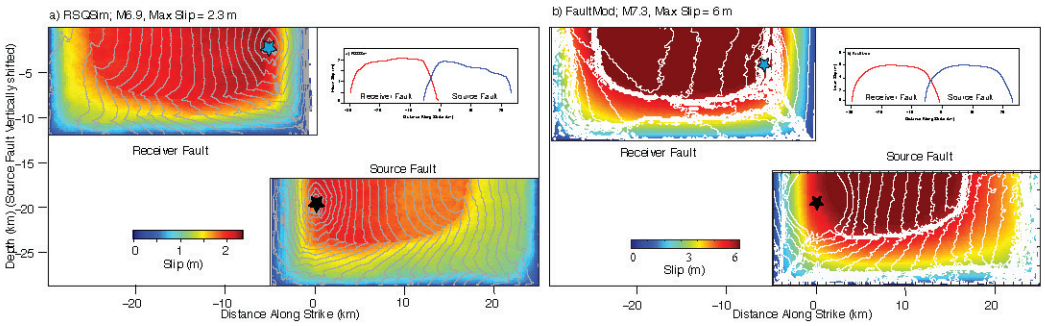

Figure 3.5: a) Slip distribution, rupture time contours, and slip profile for a representative example of a successful rupture jump from a multi-event simulations with a 1 km extensional stepover. b) Corresponding dynamic simulation with FaultMod using heterogeneous stresses and state-parameter values from RSQSim. Rupture in the FaultMod simulation is forced by decreasing θ in a 3 km circular nucleation region containing the RSQSim hypocenter. All other details are as described in Figure 3.2.

the results of the single-event simulations, however there is large scatter and weaker move-out. The majority of re-nucleation locations are confined to the overlapping region between the faults for all offsets in both offset orientations. However, some events re-nucleate over 4 km off the end of the source fault, in both offset directions. Note, we refer to the region between -5 and 5 km along strike of both segments, that contains all the re-nucleation locations, as the "re-nucleation zone" in the following sections.

To explore the effects of evolved, heterogeneous initial stress in dynamic simulations with FaultMod, we selected pre-rupture stresses from several representative examples from the RSQSim simulation whose re-nucleation locations span the range shown in Figure 3.6 The re-nucleation locations from the FaultMod simulations fall within the re-nucleation zone defined by the scatter in RSQSim re-nucleation locations (blue diamonds in Figure 3.6). For extensional offsets the FaultMod re-nucleation locations tend to be confined to the distance interval between -200 and +400 m along strike, whereas, for compressional

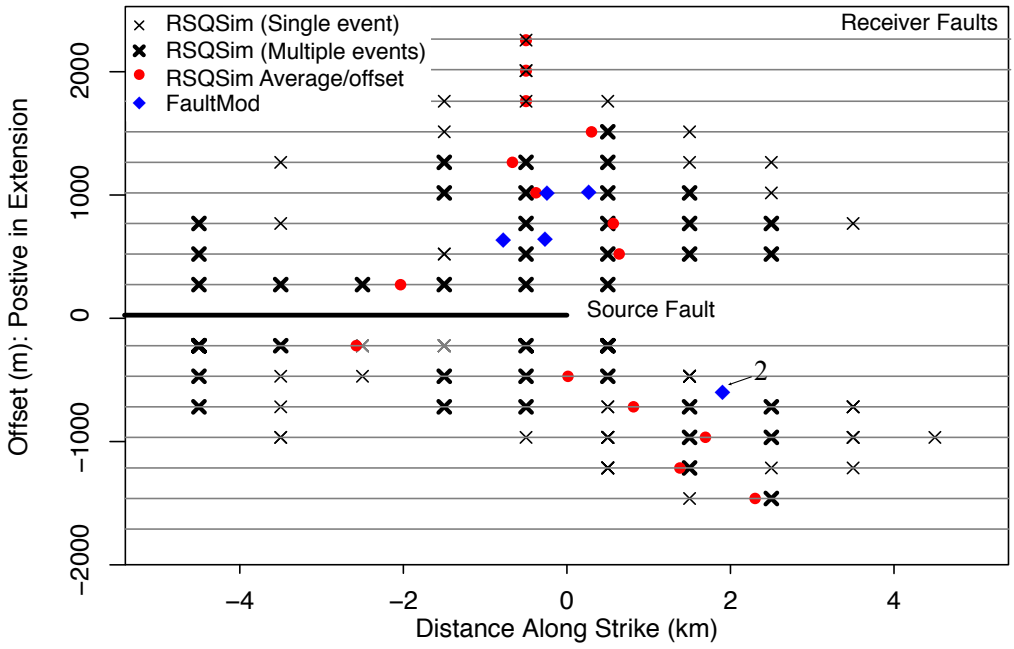

Figure 3.6: Re-nucealation locations with respect to the end of the source fault (as in Figure 3.3) for successful rupture jumps at the given offset for long-term multi-cycle simulations in RSQSim (black and red symbols). In these simulations, $\alpha = 0.25$, which is comparable to the closed red symbols in Figure 3.3. Bold black symbols indicate multiple events that re-nucleate at that distance along strike. The average re-nucleation location for all events that jump a given offset from RSQSim are shown in red. re-nucleation locations from the FaultMod companion event (blue) using the evolved stresses and state from RSQSim. Note; the two FaultMod simulations of rupture at 600 m compressional offsets, re-nucleated at the same position along strike, but are separated by 2.5 km down dip.

offsets, the re-nucleation locations are +1800 m away from the end of the source fault. Additionally, simulation of events with heterogeneous initial conditions for 1 km compressional offsets failed to rupture across the stepover, even with the necessary 10% increase in the value of shear stress. Results shown in Figure 3.6 indicate that the heterogeneous initial stress conditions lead to a large scatter of the preferred re-nucleation location on the receiver fault; a topic we discuss further in the following section.

Pre-stress Conditions

RSQSim results allow for analysis of the pre-rupture stress conditions of re-nucleation elements on the receiver fault. One might expect the re-nucleation locations to be controlled by the interaction of the stress transferred from slip on the source fault with the pre-event stresses on the receiving fault. To assess the importance of the latter, we define a stress ratio, M (eq: 3.5), as the average apparent coefficient of friction of the re-nucleation element of all events (N) that jump a given offset divided by the average apparent coefficient of friction of all elements in the re-nucleation zone averaged over all events that jump, such that;

$$\mu_{i,j} = \frac{\tau_{i,j}}{\sigma_{i,j}}, \tag{3.4}$$

where $\tau_{i,j}$ and $\sigma_{i,j}$ are the shear and normal stresses, respectively on the j^{th} element just before the i^{th} event. r_i is also defined as the re-nucleation element of the i^{th} event. Then,

$$M = \frac{\frac{1}{N_{ev}} \sum_i \mu_{i,r_i}}{\frac{1}{N_{ev}} \sum_i \frac{1}{N} \sum_j \mu_{i,j}} = \frac{\sum_i \mu_{i,r_i}}{\sum_i \frac{1}{N} \sum_j \mu_{i,j}}, \tag{3.5}$$

where the sums over i are over all the events that jumped in a given simulation, the sums over j is over all the elements in the re-nucleation zone, N is the number of elements in the re-nucleation zone, and N_{ev} is the number of events that successfully jump in a given simulation. In this construction, values of M >1 indicate that the apparent coefficient of friction (which is simply a measure of stress) on the re-nucleation element is higher than that of the re-nucleation zone, suggesting this region should be more susceptible to rupture. Results show M-values are greater than 1 for all offsets (Figure 3.7a). This indicates that the pre-stresses are higher on the re-nucleation element than elements in the surrounding re-nucleation zone for all offsets. This suggests that the resulting re-nucleation location governed by the pre-rupture stress conditions that evolve continuously over multiple earthquake cycles.

To further quantify the relative stresses, we compute percentiles for each re-nucleation element (r_i) with respect to the all other elements in the re-nucleation zone (μ_{rz}). Results in Figure 3.7b also indicate that the stress on the re-nucleation element is not significantly higher than for the remainder of the re-nucleation zone for offsets less than 1 km in compression or extension (*e.g.* for 750 m compressional offset, the r_i for one event is only greater than 20% of the other elements in the re-nucleation region). For offsets larger than ±1 km, r_i is generally larger than ∼85% of the other elements in the re-nucleation zone. Finally, we compute the average time to instability for the element that becomes the re-nucleation element assuming the source fault had not ruptured. We find that the time to instability is longer for smaller offsets (Figure 3.7c). The average time to instability (determined with the nucleation solutions from Dieterich (1992, 2007)) is 2.5 and 4.8 times

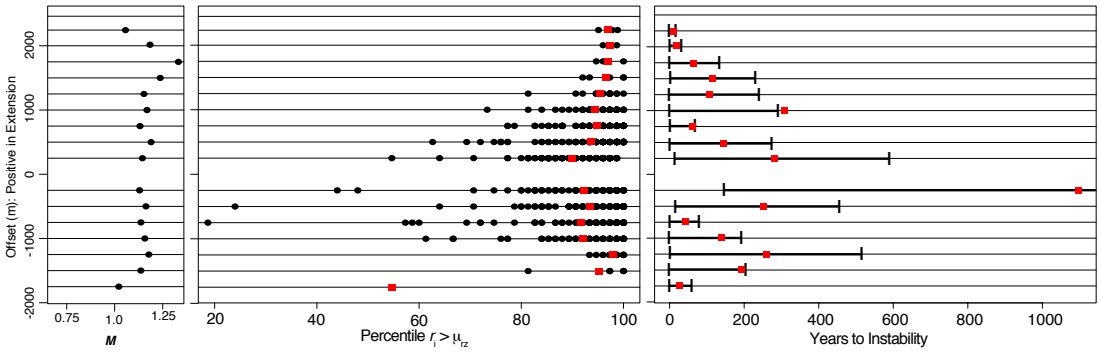

Figure 3.7: Properties of the re-nucleation element. a), M- ratio, b) Percentile of r_i of the re-nucleation element. The black circles give the percentile for each re-nucleation element with respect to all elements in the re-nucleation zone (μ_{rz}); the mean percentile is shown by the red squares. c) The time to instability for all elements that will become the re-nucleation element assuming the source fault had not ruptured. The mean time to instability is given by the red squares and the bars show the 68^{th} percentile. The M-ratio is systematically lower for offsets $\pm \leq$1 km indicating that the stresses on the re-nucleation elements are not higher than average in the re-nucleation zone. This is also supported by the percentiles shown in panel b, which indicate that some re-nucleation elements at small offset distances are only higher than 20% of the other elements in the re-nucleation zone. Conversely, the stresses on re-nucleation elements at offsets larger than 1 km are higher than those of the surrounding zone. Additionally, the time to instability (panel c) shows that elements that become the re-nucleation element are closer to failure for offsets larger than 1 km. These results indicate that the stress changes induced by source fault rupture control the re-nucleation location at closer offsets, while the pre-stress conditions dominate re-nucleation locations at larger offsets.

longer for compressional and extensional offsets > 1 km than ≤ 1 km, respectively. This demonstrates that as offsets increase, the future re-nucleation patches must be closer to failure for successful ruptures jumps to occur. Altogether, the results of Figures 3.7(a, b, and c) indicate there is a trade off between the factors that control the re-nucleation location; static stress changes induced by source fault rupture may play a larger role at small offsets, whereas the pre-stress controls the re-nucleation locations at larger offsets.

3.4.4 S-ratio

The S parameter (the measure of distance of the stress state from failure described earlier) just prior to large events is unknown for actual faults. Therefore dynamic rupture modelers typically must choose this somewhat arbitrarily, sometimes choosing to model a range of S that brackets the value that marks the transition between sub- and super-shear rupture. It is therefore of interest to examine the range of pre-event values of S that arise naturally in the long RSQSim simulations. Because these stresses are heterogeneous, we define an average S for an event that successfully jumps the stepover as:

$$S = \frac{\bar{\tau}_p - \bar{\tau}_0}{\bar{\tau}_0 - \bar{\tau}_f} \tag{3.6}$$

where $\bar{\tau}_p$, $\bar{\tau}_0$, and $\bar{\tau}_f$ are the peak, initial, and final shear stresses averaged over the elements that ruptured in that event. Median S values for successful rupture jumps for each offset are between 1.5 and 2.5 (Figure 3.8), systematically larger than the 1.19 sub-/super-shear threshold seen in previous 3D studies (Dunham, 2007). This indication of relatively low pre-rupture stresses may explain why ruptures do not simultaneously jump stepovers larger

than 2.25 km in our simulations. This suggests that S-values < 1.19 may be uncommon along real faults with evolved stresses. Thus, numerical simulations of rupture along faults with these initial conditions may be over-estimating the maximum jumpable distance due to unrealistically high stresses.

The maximum jump distance of 2.25 km in the simulations presents a paradox given that earthquakes have been observed to jump stepovers larger than 2.25 km (Wesnousky, 2006), yet in physics-based simulations heterogeneous pre-rupture stress conditions are relatively low and are thus, unable to reproduce this result. One possible explanation is that faults merge or coalesce with depth onto simpler, non-segmented structures than those seen at the surface. Such flower-like structures such as these have been observed along well-developed structures such as the San Andreas (Weldon et al., 2002), the North Anatolian (Bozkurt and Koçyiðit, 1996), and southern Alpine faults (Barth et al., 2013). Dynamic rupture models also show that rupture propagation is aided by dip-slip faults in the stepover regions that link the primary strike-slip faults (Oglesby, 2005). It is also possible that some observed ruptures do not jump instantaneously, but that rupture between the segments was delayed; a phenomena we elaborate on in the following section.

3.4.5 Maximum Jump Distances

The maximum jumpable distance in the RSQSim simulations is 1.75 km for compressional stepovers, and 2.25 km for extensional offsets. Ruptures occur at offsets >1.5 km less than 10% of the time in each catalog of ∼100,000 simulated years. At larger offsets, the source and receiver faults fail more frequently in as individual ruptures that are separated

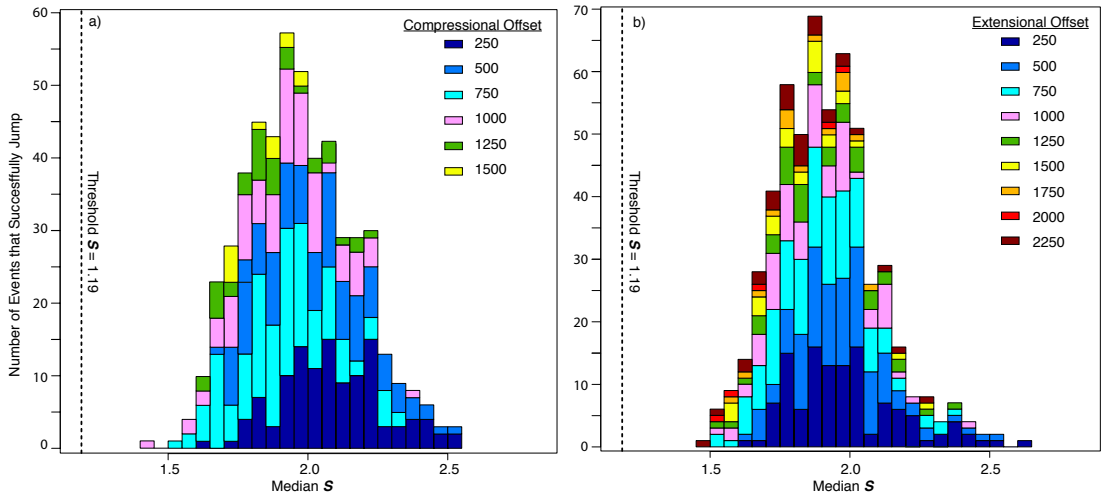

Figure 3.8: Stacked histograms of the median S-ratio for every event that successfully jumps a given offset for compressional (a) and extensional (b) stepovers. Colors indicate offset as given by the legend in each figure. The S-ratio is computed after calculating the mean τ_0, τ_p, and τ_f for every fault element that ruptures in the event. The S values over both faults in events that jump are systematically higher than threshold value of 1.19, below which, high initial stresses lead to more energetic and supershear rupture propagation speeds.

by a short time delay (*i.e.* separated by delay times between 1 minute and four years).

Probability of Rupture Jumping

Earthquake nucleation is largely a self-driven highly time-dependent process on faults governed by rate-state frictional properties. In the fault stepover setting, elements on the receiver fault that begin the nucleation process due to stress changes induced by rupture of the source fault, will eventually rupture after a time delay ranging from seconds to years. These events will range in magnitude, and therefore will be either aftershocks of the source fault rupture, or will be as large or larger than the primary rupture. Previous dynamic simulations of rupture across fault stepovers classify a successful rupture jump as one where the source and receiver fault either rupture simultaneously or within several

seconds of eachother (Harris and Day, 1993; Ryan and Oglesby, 2014). Previous studies also show that the time delay increases by a few seconds as offset distances increase (Harris and Day, 1993; Ryan and Oglesby, 2014). Classification of a successful rupture jump in nature depends on the perspective of the observer. For example, seismic instrumentation can discern between events that occur within seconds, yet, a person will experience continuous strong ground motions even if the events are separated by minutes. Furthermore, ruptures separated by delay times on the order of months to a few years would be indiscernible in a paleoseismic study (Field et al., 2014). Therefore, for the purposes of this analysis, we consider earthquake pairs (*i.e.* source and receiver fault ruptures) that either rupture simultaneously or that are separated by time-delays of up to four years.

Our long-term synthetic earthquake catalogs generated by RSQSim allow us to study the probability of rupture to jump a stepover in a variety of settings. In this study, we analyze a total of 208 catalogs that are 100,000 years long, for 16 offsets and 13 over or underlaps (Figure 3.9). We develop a criterion to determine the rupture jump probability at each of these offsets and overlaps for simultaneous jumps as well as jumps that are delayed by up to 4 years. The probability is defined as $P_j = \mathrm{J}_s/(J_s + J_f)$; where J_s and J_f are the total number of successful and failed jumps in a given simulation, respectively, from the criteria listed in the *Multi-Cycle Event Simulation* section above.

For simultaneous jumps (Figure 3.9), we find that a 4 km overlap results in the most successful jumps across compressional offsets (except for at 250 m compressional offsets, where the probability of jumping is marginally higher for 1 km overlaps). For extensional offsets, overlaps between 0 and 3 km result in roughly the same jumping probabilities.

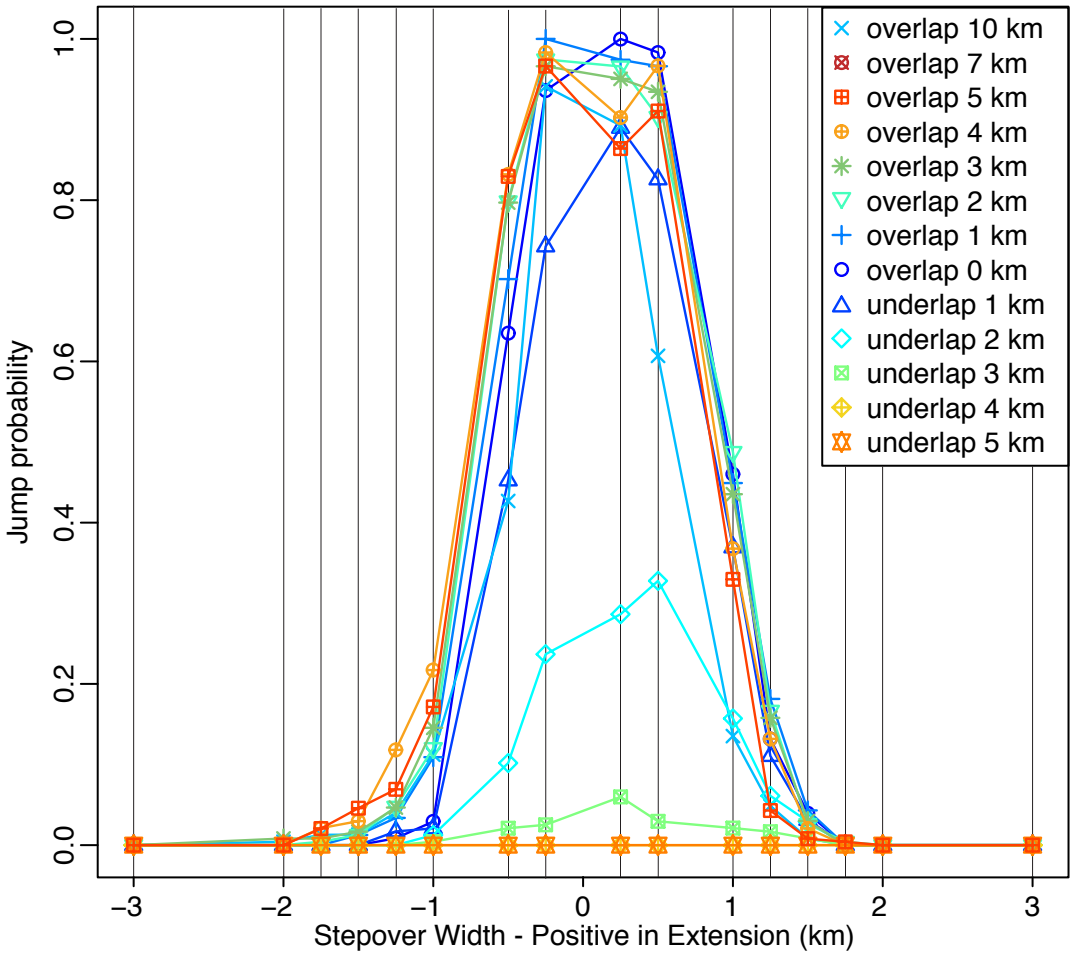

Figure 3.9: The probability of rupture jumping as a function of fault overlap length and offset. Underlaps refer to a gap along strike. The likelihood of rupture jumping is computed for 208 RSQSim runs over 13 overlap/underlap distances and 16 offsets. Rupture jumps 1.5 km compressional and extensional offsets <10% of the time in 100,000 year long simulations. Rare rupture jumps of extensional offsets greater than 1.5 km are observed in the 100,000 year synthetic catalogs (*i.e.* 3 events jump at 1.75 km offsets and 1 event jumps 2 and 2.25 km offsets. 4 km overlaps produce the highest probability of jumping, and 10 km overlaps seem to hinder, rather than aid rupture jumps.

Interestingly, larger overlaps (*i.e.* 10 km) hinder rather than aid in rupture propagation, resulting in fewer jumps than a 1 km underlap at the same offset. Ruptures successfully jump stepovers even with at 3 km underlap ∼30% of the time for offsets less than 1 km in either step direction. In these simulations, rupture is capable of simultaneously jumping stepovers as large as 1.75 km across both fault geometries ∼5% of the time.

We determine the rupture jump probability for each of the offsets and overlaps listed above, for increasing inter-event times between source and receiver fault ruptures (Figure 3.10). The probability of rupture jumping a 1 km stepover increases by ∼45% from <5%for overlaps between 1 and 7 km and delay times between 1 min and 4 years . Furthermore, rupture is also capable of jumping 2 to 2.25 km compressional offsets 15%-20% and 5%-10% depending on the overlap/underlap distance. Successful rupture jumps <2km occur more frequently for extensional offsets, between ∼18% and 30% depending on ovelap/underlap distance. Lastly, longer time delays between source and receiver fault ruptures increase the probability that rupture will jump onto faults with a larger gap along strike. For example, ruptures are not capable of immediately jumping across faults with 3 km offsets and 3 km of underlap, however, with delay times up to 4 years , the probability of a rupture jump increases to ∼10%.

3.5 Discussion

We use the multi-cycle earthquake simulator, RSQSim, and the fully dynamic rupture model, FaultMod, to compare how earthquakes propagate along *en echelon* strike-slip fault systems in two situations, 1) single-event simulations with homogeneous initial

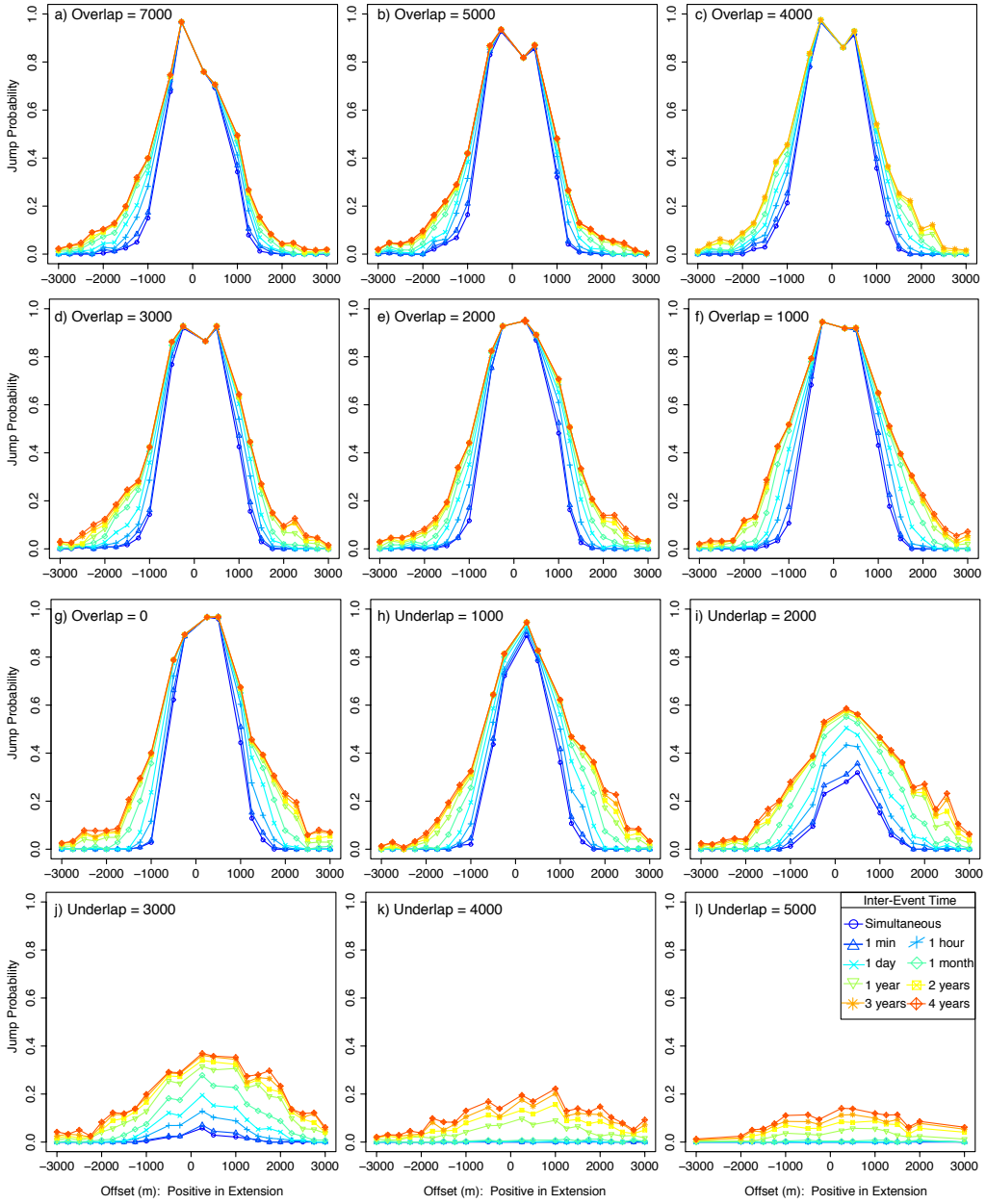

Figure 3.10: Jumping probabilities as a function of inter-event time for all offsets and overlaps. Probabilities are shown for event pairs (*i.e.* separate ruptures on source and receiver faults) that are separated by small periods of time. As the classification of a rupture as a "successful jump" depends on the perspective of the observer, inter-events times range from 1 minute to 4 years . All inter-event times are shown by the colors and symbols in the legend in panel l. The probability of a rupture jump increases by ∼45% for overlaps between 1 and 7 km for offsets ± ≤1 km and the maximum jump distance increases to 3 km for all overlap and underlaps when inter-event times of 4 years are considered.

stresses, and 2) multi-cycle simulations with heterogeneous stressing conditions. Several studies have demonstrated the effects of heterogeneous initial stresses on rupture propagation on single faults (Day, 1982; Olsen et al., 1997; Xia et al., 2004; Madariaga and Olsen, 2000; Ben-Zion et al., 2003; Lozos et al., 2015); however, those stress fields must be inferred since it is not possible to measure them directly. Stress distributions along faults modeled in RSQSim evolve based on the physics of stress transfer over multiple earthquake cycles due to slip during earthquakes plus external loading sources. Thus, RSQSim provides an idea, based on the physics believed to be important in the earthquake process, of how the heterogeneous stress field along natural faults might be distributed. Because RSQSim uses approximate analytical expressions, it is necessary to validate the model results against more rigorous, fully dynamic calculations of the rupture process. A previous comparison between RSQSim and Dyna3d for single-event simulations along a single, planar fault with homogeneous initial stresses show similar slip distributions, final total slips, and stress changes (Richards-Dinger and Dieterich, 2012). Our goals for continuing this type of comparison with FaultMod to include rupture along parallel, but offset faults both with homogeneous and heterogeneous initial stressing conditions are two-fold: 1) to investigate RSQSim's ability to accurately model rupture across fault stepovers, and 2) determine the effect of heterogeneous initial stresses on rupture propagation across those stepovers.

For single-event simulations with homogeneous initial conditions, we find that results from RSQSim (with rate- and state-dependent friction) and FaultMod (with slip-weakening friction) show a high level of agreement with respect to slip distribution, average slip, and qualitative rupture time pattern. Additionally, the pattern of re-nucleation loca-

tions on the receiver fault from RSQSim are similar to that shown in Figure 6 of Harris and Day (1993), despite the different friction laws and computational methods. The pattern of re-nucleation locations from RSQSim and Harris and Day (1993) correlates with the pattern of static stress change due to rupture on the source fault, where the Coulomb stresses are higher in the regions along strike where re-nucleation occurs for both compressional and extensional stepovers (Harris and Day, 1993). This suggests that static stress increases from slip on the source fault govern the re-nucleation location, at least on faults with initially homogeneous stresses. The maximum jumpable distances are 45% and 50% farther for compressional and extensional offsets in FaultMod versus RSQSim, respectively (Figure 3.3). When assuming constant normal stress effects on the state-parameter (*i.e.* $\alpha = 0$), jumps in RSQSim are 11% and 40% farther for compressional and extensional offsets, respectively, than when $\alpha = 0.25$, suggesting that the effects of variable normal stress on θ also play a role in rupture propagation. Non-zero values of α tend to counteract those of the direct effect of changes of normal stress on sliding strength (*i.e.* $\Delta\tau = \mu\Delta\sigma$. The maximum slip is nearly 25% higher for the FaultMod solution compared to the results from RSQSim. The larger jump distances and maximum slip of the FaultMod solution may be related to differences in the frictional formulation and/or to dynamic stress transfer generated by the passage of seismic waves that are not accounted for with the elastostatic calculations in RSQSim. Despite the lack of dynamic stress transfer, these results indicate that RSQSim performs quite well compared to fully dynamic models and can be used to investigate rupture propagation over multiple earthquake cycles in more complex settings characteristic of natural fault systems.

We also examine rupture along *en echelon* faults with heterogeneous initial stresses. For this analysis, both FaultMod and RSQSim use the rate- and state-dependent frictional formulation, although with different values of D_c due to computational differences with respect to event nucleation. This introduces a complication in that the heterogeneous shear stresses that evolve in RSQSim must be increased in order for rupture to propagate in the dynamic model. Thus, maximum/total/average slip, magnitude, and stress drop are expected to be larger for the corresponding FaultMod event. Therefore, we focus on the qualitative slip distribution and profile, the rupture time pattern, and the pattern of re-nucleation locations for this comparison. Qualitatively, the results from both models are similar. Both show maximum slip on the receiver fault in the area of the re-nucleation location and less slip on the source fault. Slip profiles demonstrate elliptical distributions, similar to that expected by rupture along a single fault segment, however, slip tapers faster in the overlapping region in the RSQSim model. The rupture begins slowly near the hypocenter on the source fault in the RSQSim model, differing from the FaultMod solution which is caused by the artificial manner in which the event is nucleated. The rupture picks up speed along the boundaries of the high slip zones. Stress is concentrated in these regions due to a previous, but smaller earthquake in the multi-cycle RSQSim model. After jumping, rupture is slow to begin propagation near the re-nucleation location in both models, before then propagating in a similar fashion to rupture on the source fault.

The re-nucleation locations for events with heterogeneous stresses are considerably different than those from simulations with homogeneous initial stresses. In the latter case, the re-nucleation locations are controlled by the pattern of static stress change, which is

similar to that of the time-dependent dynamic stress change. However, with heterogeneous initial stresses, the re-nucleation locations favor a position within the re-nucleation zone, but there is little correlation these locations and the pattern of Coulomb stress change. This suggests that the heterogeneous stresses prior to the event control the location of nucleation of the receiver fault rather than the static or dynamic stress changes induced by rupture of the source fault. Additionally, the maximum jumpable distance is 1.75 km in compression and 2.25 km in extension for RSQSim. This is consistent with the 2D homogeneous model results from Harris and Day (1993) when $S = 1.65$, and with the low-stress models of Ryan and Oglesby (2014). However, ruptures fail to jump offsets larger than 1 km in extension and 600 m in compression in the dynamic model comparison, even when increasing the shear stress everywhere on the faults.

Analysis of the pre-rupture stress conditions reveals that the median S-ratio for jumping events are never smaller than the threshold value, 1.19, below which more energetic, supershear ruptures occur. This suggests that rupture jumps across offsets larger than $\sim$2.5 km in previous numerical simulations are the result of unrealistically high pre-stresses. Therefore, mechanisms such as extreme weakening may be more important than initial stresses in observed earthquakes that transition to supershear rupture speeds. Rupture propagation across larger offsets may also be aided by a connecting fault segment at depth.

We are now able investigate the probability that earthquakes can propagate across a fault stepover with long-term, multi-cycle simulations. For the first time, we document the likelihood that rupture jumps occur immediately (*i.e.* in a single event) or as successive independent source and receiver fault ruptures, with relatively short inter-event times. Our

results indicate that both the maximum jump distance and the jump probability increase with increasing inter-event time. Results indicate that rupture is unable to immediately jump offsets > 1.5 km more than 5% of the time in both compression and extension. Instead, rupture jumps across offsets between 1.5 and 3 km are delayed in time. The likelihood of rupture jumping offset distances up to 3 km increases more than 10% when delay times of up to 4 years between source and receiver fault rupture are considered.

3.6 Conclusions

Our results indicate that the quasi-dynamic earthquake simulator, RSQSim, is capable of producing results comparable to those of fully dynamic earthquake rupture models despite the approximations of elastodynamics and use of analytical solutions of the governing physical equations. For single-event simulations with homogeneous initial conditions, RSQSim shows similar earthquake magnitudes, distributions of slip, and qualitative rupture time patterns. In our simulations, rupture jumped 50% farther with the fully dynamic method, presumably due to differences in the frictional formulation and/or stress changes due to the passage of the dynamic wave field. Re-nucleation locations from RSQSim models, however, agree with the spatial pattern shown by Harris and Day (1993), suggesting that static stresses govern the spatial pattern, at least for models with homogeneous initial stresses.

Investigation of rupture propagation along faults with evolved heterogeneous stresses over multiple earthquake cycles show dramatically different results. First, qualitative slip distributions and rupture time patterns are in general agreement between both simulation

methods, however computational differences with respect to earthquake nucleation require a 10% increase in initial shear stress for rupture to propagate with the dynamic method. This leads to increased slip, stress drop, and magnitude of the dynamic simulation. We speculate that this increase in initial shear stress may also lead to successful jumps at larger offsets that may be simply related to the higher stress rather than the physics of rupture propagation.

Pre-rupture stress conditions are such that the re-nucleation at small offsets is governed by static stress changes, while re-nucleation across larger offsets is highly dependent upon the pre-stress along the receiver fault. Additionally, the pre-rupture S-ratio ranges between 1.5 and 2.5, which indicates that evolved stress states are generally lower than those used in previous dynamic modeling studies.

Finally, our long-term multi-cycle earthquake simulations allow for statistical analysis of the likelihood that rupture is successful at jumping a stepover at various offset distances, and any dependence upon the length of the overlapping or underlapping region. We find that the probability of rupture jumping and the maximum jump distance both increase as the inter-event time between source and receiver fault ruptures increases. This previously undocumented result demonstrates the necessity of computationally efficient, long-term, multi-cycle earthquake simulations to understand the physics that control the earthquake rupture process and has direct implications for seismic hazard. Because RSQSim is capable of simulating earthquake occurrence along geometrically complex fault systems for millions of years, new statistical results based on physics, such as likelihood that rupture can jump a given stepover, can aid earthquake rupture forecasts of multi-segment ruptures

such as those produced in version 3 of the Unified California Earthquake Rupture Forecast (Field et al., 2014).

3.7 Supporting Information for "3D Multi-Cycle Simulations of Earthquake Rupture Across Fault Stepovers"

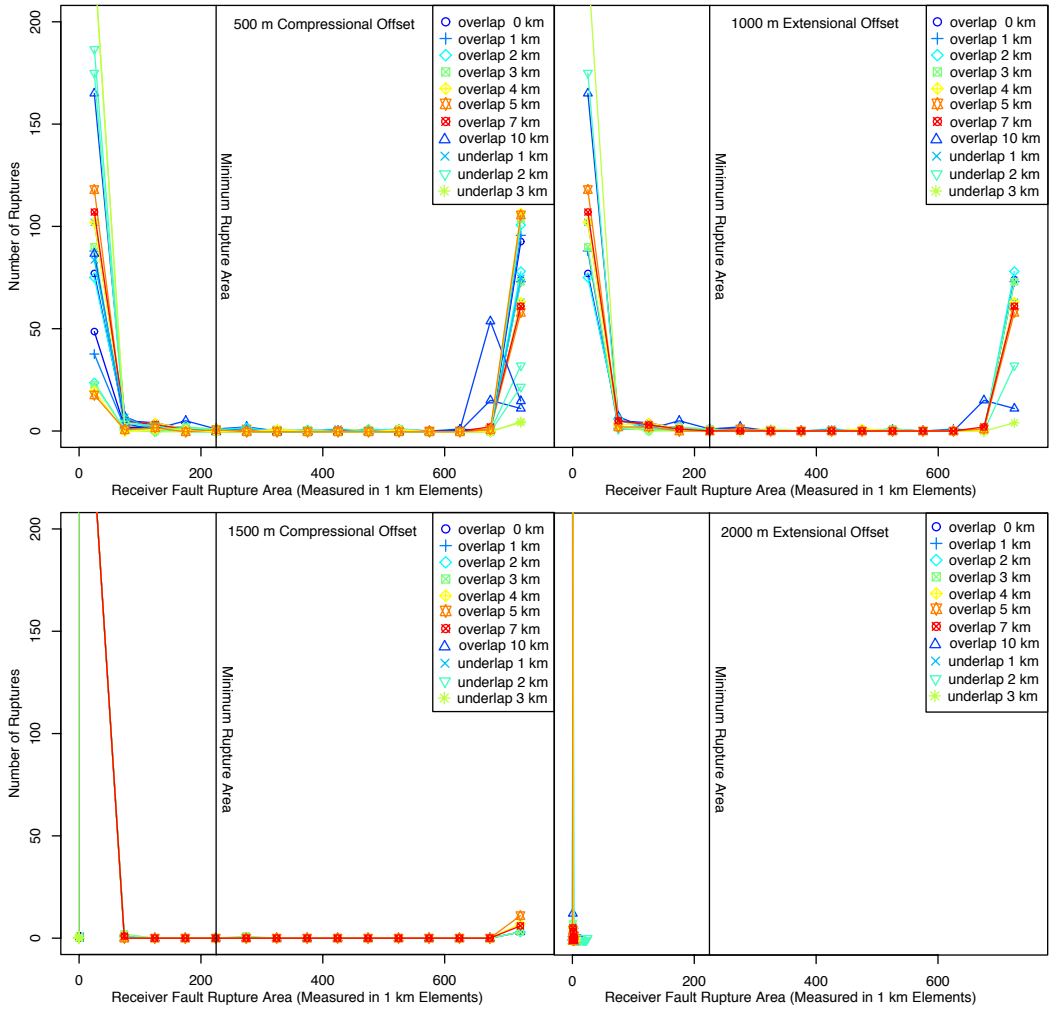

Figure 3.11: Receiver fault rupture area for all events that jump a stepover for representative offsets and 13 overlap and underlap distances. The receiver fault area is 750 km^2 (or 750 fault elements). Events that are classified as a "successful jump" by the criteria listed in the text must have receiver fault rupture areas larger than the minimum rupture area (black vertical line). This criteria is successful at automatically capturing all by 1% of the successful jumps without visual inspection of more than 200,000 earthquakes in 208 simulations.

Chapter 4

Simulating Induced Seismicity

4.1 Introduction

It has long been known that anthropogenic activities such as mining, reservoir impoundment, hydrofracturing, and extraction of fluids from the subsurface induce earthquakes (Healy et al., 1968; National Research Council, 2013; Ellsworth, 2013). The practice of injecting fluids into the subsurface to dispose of waste-water or to enhance petroleum production has received increased attention from the public following several recent earthquakes in the Central and Eastern, United States and in Western Canada (Horton, 2012; Gan and Frohlich, 2013; Holland, 2013; Keranen et al., 2013, 2014; Frohlich et al., 2011; Kim, 2013; Llenos and Michael, 2013; Frohlich et al., 2014; Rubinstein et al., 2014). The largest of the earthquakes possibly associated with waste-water disposal was the 2011 M_w5.7 Prague, Oklahoma event that was felt by large numbers of residents, caused damage to infrastructure, and resulted in personal injury (Keranen et al., 2013). Several well-documented cases of injection-induced seismicity have been identified since the 1960's. These include the Rocky

Mountain Arsenal, Colorado (Healy et al., 1968); Rangely, Colorado (Raleigh et al., 1976), Ashtabula, Ohio (Seeber et al., 2004), Paradox Valley, Colorado (Ake et al., 2005), Guy, Arkansas (Horton, 2012), and Youngstown, Ohio (Kim, 2013). In these instances, shallow seismicity began near the injection well and migrated away from the well at rates similar to those at which fluids diffuse within the injection interval. However, some recent cases of induced seismicity, including the Prague, Oklahoma sequence do not appear to follow this simple rule. In Prague, injection operations were carried out for $\sim$20 years before a sizeable earthquake occurred (Keranen et al., 2013). Yet in other circumstances, such as those at an enhanced geothermal plant in Basel, Switzerland, two M$\sim$2.5 earthquakes that occurred in 2008 were enough to trigger operational modifications which included termination of injection only 6 days after reservoir stimulation began. In this case, the largest magnitude event occurred just hours after shut-in and was followed by three additional M>3 events within the next month (Häring et al., 2008; Deichmann and Giardini, 2009).

The basic physical mechanisms that lead to induced earthquakes have been recognized for many decades. To the first order, for fluid injection to produce earthquakes, the region must be critically stressed and optimally oriented faults must be present (National Research Council, 2013). Terzaghi (1925) introduced the concept that increasing fluid pressures lead to decreases in the effective normal stress acting on a potential failure surface, which combined with the Coulomb failure criterion gives,

$$\tau \geq \mu(\sigma_n - p), \tag{4.1}$$

where τ is the shear stress, μ os the coefficient of friction, σ_n is the normal stress and p is the pore-fluid pressure change. Hence, shear failure will occur when the shear stress

overcomes the effective normal stress σ_{eff}, where $\sigma_{\text{eff}} \equiv (\sigma_n - p)$. This can be illustrated by a Mohr diagram which depicts the relation of Equation 4.1 to the maximum and minimum principal compressive stresses, σ_1 and σ_3, respectively. Frictional sliding occurs when the Mohr circle, defined by the differential stress $(\sigma_1 - \sigma_3)$, intersects the failure envelope defined by the coefficient of friction. A fault in a stable regime does not intersect the failure envelope, but can be brought to failure in two ways: 1) increases in the differential stress which increases the diameter of the Mohr circle, or 2) decreases in the effective normal stress which shifts the circle to the left on the Mohr diagram. Decreasing the effective normal stress may cause shear failure on faults at a variety of orientations, not just those that are optimally oriented in the present tectonic stress field, provided that the pre-existing shear stress is close enough to critical.

Increases in pore-fluid pressure are the most commonly cited cause of injection-induced seismicity, therefore many previous modeling studies have focused on the spatial distribution of fluid pressures (Hsieh and Bredehoeft, 1981; Shapiro et al., 2002; Shapiro and Dinske, 2009). However, this approach does not consider the time-dependent characteristics of fault yielding that are known to result in space-time clustering of earthquakes, which are no doubt important to investigations of induced earthquakes. Earthquakes that cluster in the form of foreshocks/aftershocks that are fundamental features of earthquake sequences that can be explained by the rate- and state-dependent constitutive formulation (Dieterich, 1994, 2007). Coupling geomechanical reservoir models with physics-based earthquake simulations can provides a basis for modeling the space-time characteristics of induced seismicity that, in turn, allows investigation of the relations amoung reservoir characteristics, injection

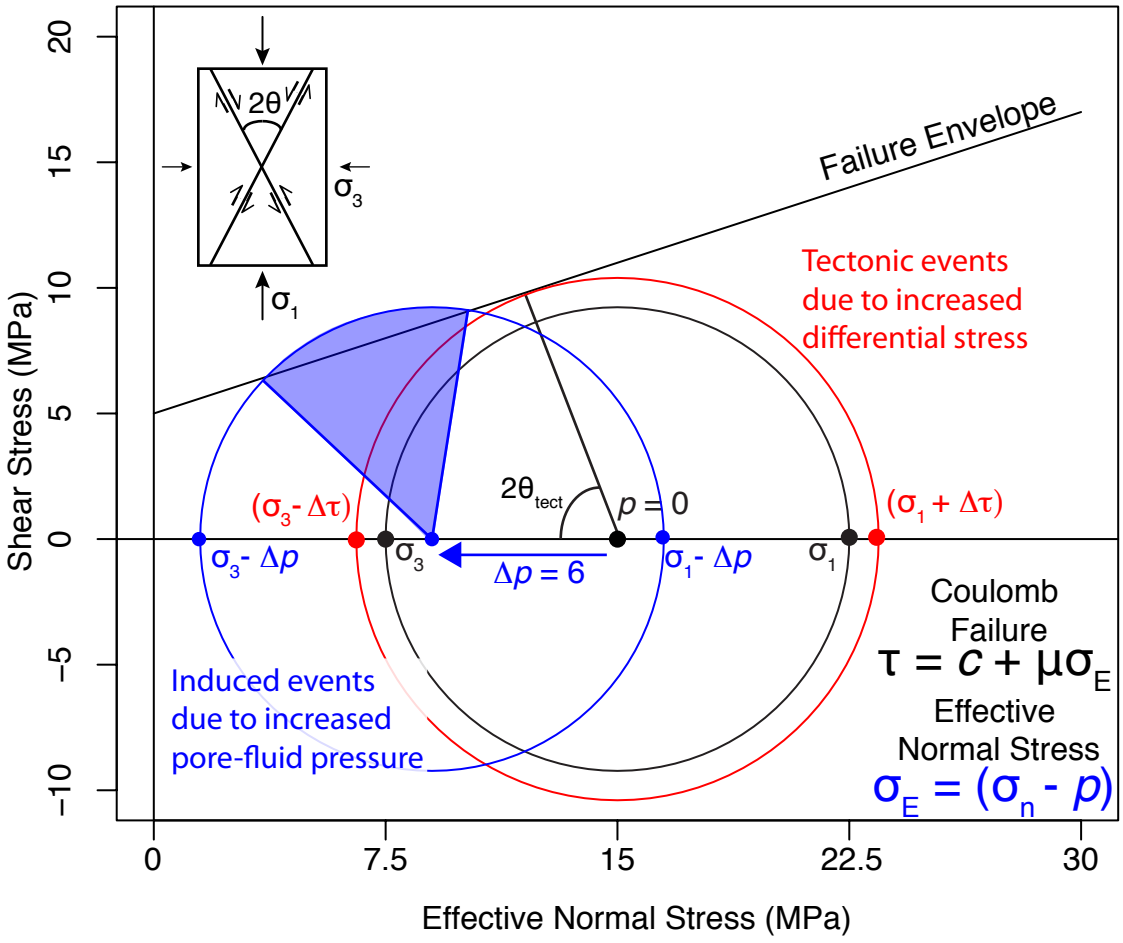

Figure 4.1: Cartoon Mohr diagram depicting the stress state for a stable fault (black), tectonic earthquakes caused increased shear stress (red circle) and induced earthquakes caused by increased pore-fluid pressure (blue circle). Shear failure occurs when the Mohr circle interests the failure envelope for fault orientations at an angle 2θ, the angle between the maximum principal stress and the pole to the plane upon which the stresses are acting. Increases in shear stress increase the diameter of the Mohr circle (*i.e.* the differential stress) which may lead to shear failure. Conversely, earthquakes induced by increases in pore-fluid pressure decrease the effective normal stress, therefore, do not require increases in the differential stress to cause shear failure. Note that compression is positive, and c is cohesion.

paramters, and seismicity.

Here, we couple a 3D, physics-based, quasi-dynamic earthquake simulation code, RSQSim, with a reservoir model that computes pressure changes on faults due to fluid injection. RSQSim incorporates rate-state fault properties that govern the space-time clustering characteristics of earthquake sequences. The computational efficiency of the code makes it feasible to explore the large parameter space inherent to induced seismicity which includes injection reservoir characteristics, pre-existing shear stress conditions, and the rate-state fault properties. We run multiple simulations, systematically varying each of these parameters to investigate their effect on injection induced earthquakes. Insight gained from this study will advance our ability to develop site-specific models of injection induced earthquakes, best-practice protocols for injection operations, and probabilistic hazard assessments.

4.2 Simulating Induced Seismicity with RSQSim

Simulations of injection induced earthquakes with RSQSim require the following: 1) external pore-fluid pressure histories, 2) an estimate of the pre-existing stress field on the modeled fault, and 3) the rate-state fault properties. Here, we explore the effects of the each of these on induced earthquake sequences.

4.2.1 Reservoir Model

External pore-fluid pressure histories provided to RSQSim may be computed with reservoir models of arbitrary complexity. Simple models may only incorporate the direct

effects of increased pore-fluid pressure on the effective normal stress, whereas sophisticated models may include more complicated effects such as fracture permeability or poroelasticity. Volumetric changes in the reservoir due to fluid injection modify the stress field surrounding the reservoir due to elastic coupling between the reservoir pressures and the host rock. This process leads to stress changes which affect the seismic response, however the stresses tend to be small compared to the pore-fluid pressure change (National Research Council, 2013; Segall and Lu, 2015). Note, while we do not consider them here, the poroelastic stress changes can easily be included in RSQSim models of injection induced earthquakes provided that the external reservoir model accounts for this effect. Additionally, because direct coupling between a reservoir model and RSQSim is difficult and has not yet been implemented, we also disregard the effects of permeability enhancement due to fault slip. Here, we focus our efforts on understanding the characteristics which lead to induced events related to the direct pore-fluid pressure change.

In this study, we employ a simple reservoir model that considers injection into an unbounded, uniform, isotropic half-space immediately below an impermeable layer (Wang, 2000). The nature of the unbounded reservoir causes the pressure perturbation to approach steady-state after long time periods of constant injection rate. Pore-fluid pressure at a given time and distance due to constant-rate injection that begins at time $t = 0$ at a point source is given by a simple analytic formula:

$$P(x,t) = \frac{Q}{2\pi\kappa\phi c} |x|^{-1} \operatorname{erfc} \sqrt{\frac{|x|^2}{4\kappa t}}, \tag{4.2}$$

where *x, t, Q, c*, ϕ, and κ are the distance from the injection point (m), time (sec), injection rate (m^3/s), total compressibility of the pore-fluid and the matrix (Pa^{-1}), porosity, and

diffusivity (m^2/s), respectively. The diffusivity, κ, is related to the permeability, k (m^2), fluid viscosity η (Pa·s), porosity, and the compressibility by $\kappa = k/\eta\phi c$. Pressures for more complicated injection histories are built up from this formula via superposition. From eq. 4.2, is it clear that the steady-state pore-fluid pressure is inversely proportional to the distance from the well, that it increases with increasing injection rate, and decreases with increasing diffusivity. In this work, we use typical values of these parameters listed in Table 4.1 Zoback (2007). The injection rate, Q, is similar to those in several locations where seismicity has been correlated with waste-water disposal including Paradox Valley, Colorado [$Q = 0.016$ $m^3/s \approx 0.356$ million barrels per month (mbm)], Dallas-Fort Worth, Texas ($Q = 0.014$ $m^3/s \approx 0.3$ mbm), Guy, Arkansas ($Q = 0.014$ $m^3/s \approx 0.394$ mbm), and Cleburne, Texas ($Q = 0.027$ $m^3/s \approx 0.6$ mbm) (Keranen et al., 2014). During simulations of injection induced earthquakes with RSQSim, the effective normal stress evolves with time due to slip on other fault elements and is reduced by the pore-fluid pressure acting on an element at a given time. The higher the hydraulic diffusivity, the more quickly the pore-fluid pressures respond to changes in injection. Thus, for low values of diffusivity, pore-fluid pressures will continue to rise, especially at large distances from the well, even well after the well has been shut-in before declining (Figure 4.2). Hence, diffusivity greatly effects the occurrence of post shut-in seismicity. We investigate this topic systematically later in this work (Section 4.3).

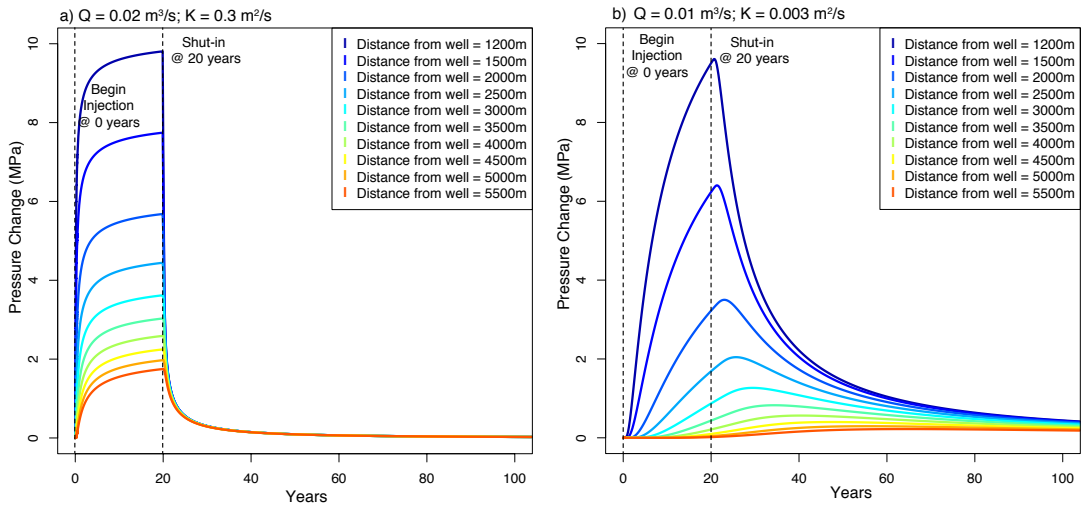

Figure 4.2: Pore-fluid pressure as a function of time for increasing distances from the well for injection beginning at 0 years and shut-in at 20 years. The well is located 1200 m from the closest fault element. The values of injection rate and diffusivity vary between the panels with all injection parameters are listed in Table 4.1. a) Pore-fluid pressure with time for $Q = 0.021$ m^3/s and a relatively high value of $\kappa = 0.3$ m^2/s, that shows a decrease of pressure nearly immediate following shut-in. b) Pore-fluid pressure for a low value of $\kappa = 0.003$ m^2/s. Here, the injection rate is decreased ($Q = 0.01$ m^3/s) such that the maximum pore-fluid pressure at the closest point to the well is nearly constant. Low diffusivity leads to increases in pore-fluid pressure for several decades after shut-in at large distances from the well (*i.e.* red curve for a point 5500 m from the well).

Q	0.01 - 0.03 m^3/s
κ	0.003 - 0.3 m^2/s
k	0.2 mD
ϕ	0.05
η	10^{-3} Pa·s
c	$5{\cdot}10^{-16}$ / MPa

Table 4.1: Default Injection Parameters

4.2.2 Effects of Pre-stress Along Modeled Faults on Induced Seismicity

The *in situ* stress field on a fault is probably the least well constrained of the parameters required to simulate earthquake occurrence. The *in situ* stress field can be characterized by the six independent components of the stress tensor, three which describe the principal stress directions, and three that describe the magnitudes of maximum ($\sigma_{\mathbf{1}}$), intermediate ($\sigma_{\mathbf{2}}$), and minimum stress ($\sigma_{\mathbf{3}}$). Near the earth's surface, one principal stress is typically oriented vertically ($\sigma_{\mathbf{v}}$) with a magnitude equal to the lithostatic stress. The remaining two principal stresses are then horizontal where the maximum horizontal compressive stress ($\sigma_{\mathbf{H}}$) can estimated with methods such as wellbore breakouts, focal mechanism analysis, or drilling induced fractures (Zoback and Zoback, 1989, 1980). However, stresses in the earth are necessarily heterogeneous and resolving an estimated *in situ* stress field into a realistic a pattern of stress on a fault is complicated. Additionally, faults are inherently complex features consisting of fractures at all scales of observation (Dieterich and Smith, 2010). The topography along fault surfaces have fractal-like characteristics which lead to

stress concentrations at asperities that are surrounded by regions of lower stress (Scholz and Aviles, 1986; Power and Tullis, 1991; Candela et al., 2009). We stochastically approximate this stress heterogeneity to explore its affect on induced seismicity. Here, we extend our previous modeling efforts that represent stress heterogeneities on the fault with smoothed Gaussian white noise (Dieterich et al., 2015) to include representations of the heterogeneous shear stress with a von Kármán autocorrelation function.

A 2-D von Kármán correlated random field is described by the power spectral density (PSD) such that;

$$PSD \propto \frac{1}{(1+k^2)^{H+1}}, \tag{4.3}$$

where k is the dimensionless spatial wavenumber given by $k = \sqrt{{a_x}^2{k_x}^2 + {a_y}^2{k_y}^2}$, H is the Hurst exponent, and a_x and a_y define the maximum correlation lengths. Decreasing the Hurst exponent increases the shorter wavelength roughness relative to the longer wavelengths and the a_x and a_y correlation lengths control the smoothing in that they determine the transition of the PSD from a flat spectra to power-law. Figure 4.3 shows examples of the von Kármán correlation field for various H, a_x and a_y values. Note that while it is possible to generate anisotropic random correlated fields with the same method, we only explore the effects of these parameters in an isotropic field.

We use the von Kármán method for generating correlated random fields to construct the pattern of pre-existing shear stresses on a planar fault surface used in simulations of injection induced seismicity. This stress heterogeneity is intended to represent stresses that might develop with rough faults under tectonic loading. In these simulations, however, the tectonic stressing rate is set to zero to ensure that all events in the simulation arise

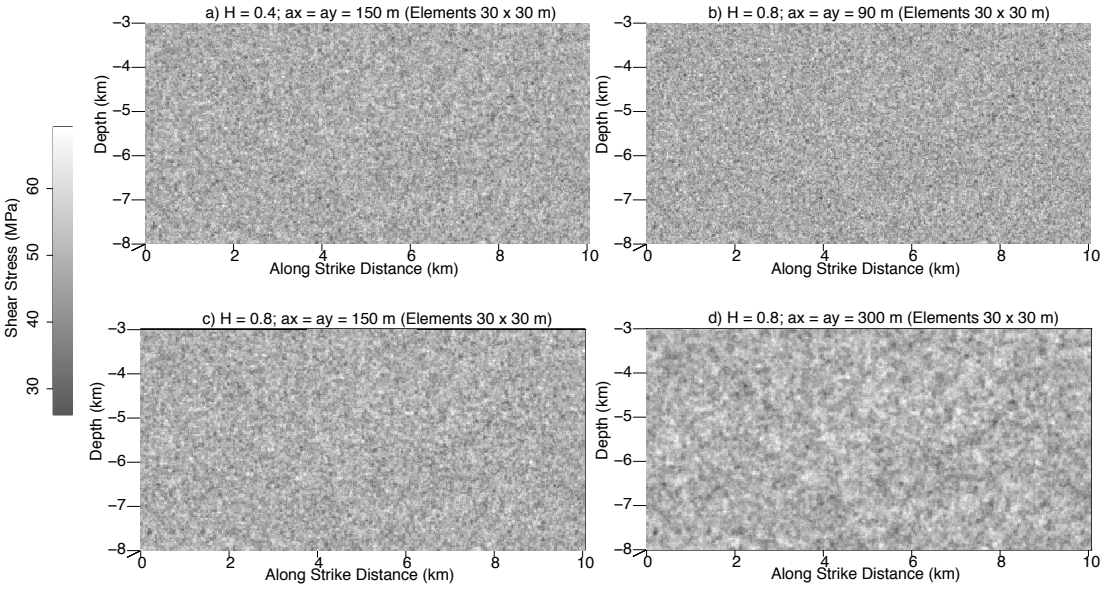

Figure 4.3: Pre-existing shear stress for one realization of the von Kármán correlated random fields, a mean of 54 MPa and a standard deviation of 5 MPa for various H numbers and correlation lengths. a) von Kármán correlated field for $H = 0.4$, $a_x = a_y = 150$ m (5 times the element length), b) $H = 0.8$, $a_x = a_y = 90$ m (3 times the element length), c) $H = 0.8$, $a_x = a_y = 150$ m (5 times the element length, d) $H = 0.8$, $a_x = a_y = 300$ m (10 times the element length); the color scale is constant for all panels.

due to changes in pore-fluid pressure. In this way, we represent regions that are no longer tectonically active, but where faults are close enough to critical stress levels that relatively small pore-fluid perturbations cause shear failure. The mean level of initial shear stress is selected such that the fault is near, but does not exceed, the critical stress for nucleating an earthquake τ_{max}.

RSQSim uses rate-state friction to describe conditions controlling fault slip. With rate-state earthquake nucleation occurs when stress exceed steady-state. In the absence of tectonic loading or pore-fluid pressure perturbations, earthquakes will still nucleate if the initial shear stress (τ_0) on any element is greater than the steady-state value (τ_{max}). The rate-state constitutive relationship (Dieterich, 1979; Ruina, 1983) is given by,

$$\tau = \sigma \left[\mu_0 + a \ln \left(\frac{V}{V^*} \right) + b \ln \left(\frac{\theta V^*}{D_c} \right) \right], \tag{4.4}$$

where a and b are the the rate-state coefficients that describe the material, μ_0 is the nominal coefficient of friction, D_c is the characteristic slip distance, V^* is the reference slip speed, θ is the state parameter, and τ and σ are the shear and normal stresses, respectively. The time-dependent evolution of state is given by the ageing law (Linker and Dieterich, 1992),

$$\dot{\theta} = 1 - \left(\frac{\theta V}{D_c} \right) - \alpha \left(\frac{\theta \dot{\sigma}}{b\sigma} \right), \tag{4.5}$$

where α describes the strength of the response of θ to variations in σ. In general, α (which ranges from 0 to μ_0) counteracts the direct effect of changes in effective normal stress. High values of α act to inhibit the effect increased pore-fluid pressure in an environment where a fault is brought to failure only by decreases in the effective normal stress. In

our simulations, α is set to low values, 0.05, such that these effects are minimized. At steady-state, $\theta = D_c/V$, therefore τ_{max} at steady-state is a simply;

$$\tau_{\max} \approx \sigma_0 \left[\mu_0 + (b-a) \ln \left(\frac{\theta_0 V^*}{D_c} \right) \right], \tag{4.6}$$

Conversely, if all elements of the fault system are below the value of the minimum critical shear stress (τ_{min}) earthquakes will never nucleate even at the maximum pore-fluid pressure due to injection. τ_{min} is given by;

$$\tau_{\min} \approx (\sigma_0 - P_{\max}) \left[\mu_0 + (b-a) \ln \left(\frac{\theta_0 \dot{\delta}^*}{D_c} \right) - \alpha \frac{b-a}{b} \ln \left(1 - \frac{P_{\max}}{\sigma_0} \right) \right], \tag{4.7}$$

where P_{max} is the maximum pore-fluid pressure change on any element (Dieterich et al., 2015). Thus, we only simulate injection induced earthquakes on faults with $\tau_{min} \leq \bar{\tau_0} \leq \tau_{max}$.

We simulate injection induced earthquakes on a planar, strike-slip, 10 km by 5 km fault buried at 3 km depth. The fault model consists of 56112, ∼30 m by 30 m rectangular elements. The injection well is located 1200 m out of the plane in Figure 4.3, 5000 m along strike, and at 5500 m depth. Assuming an injection rate, Q = 0.03 m^3/s, diffusivity, κ = 0.003 m^2/s, and all other injection and rate-and state-parameters listed in Tables 4.1 and 4.2, P$_{max}$ = 28.83 MPa for the element closest to the well. Thus, the values of τ_{min} and τ_{max} = 49.27 MPa and = 68.75 MPa, respectively, therefore we set $\bar{\tau_0}$ = 56 MPa, where $\bar{\tau_0} > \tau_{max}$ on less than 2% of all elements. The spatial distribution of the pressure change for these injection parameters is equivalent to that shown in Figure 4.2b, however the magnitude of the pressure change increases by a factor of 3, simply due to the increased injection rate.

To test the sensitivity of induced earthquake sequences to the von Kármán parameters, we perform multiple simulations modifying both the Hurst exponent (H = 0.4 and 0.8) and the correlation lengths ($a_x = a_y$ = 90 m, 150 m, and 300 m). Results are presented in Figures 4.4 and 4.5. Most importantly, we find that the Gütenberg-Richter b-value varies inversely with the correlation length (Figure 4.4a). Additionally, the maximum magnitude in each simulation and the total seismic moment appear to be weakly correlated to the correlation length (Figures 4.4b,c), however this result requires further simulations with different patterns of the pre-stress distribution before a conclusive statement can be made. The total number of events appears to be correlated with the maximum magnitude and total seismic moment for $H = 0.4$, and negatively correlated for $H = 0.8$. Figure 4.4e shows the total number of events greater than M_w4 is not affected by correlation length, however the number of events greater than M_w3 increases with increased correlation length. For larger correlation lengths we observe a greater number of M>3 but fewer smaller events resulting in a lower b-values.. Lastly, the total number of induced earthquakes that occur after the start of injection, but prior to the first sizeable event (*i.e.* an event with rupture area greater than 0.8 km^2), increases with increasing correlation length.

Figure 4.5 shows the hypocenter locations of all injection-induced earthquakes for representative simulations of various combinations of H and a_x and a_y. Hypocenters are colored by time since the beginning of injection at 0 years. There is a significant amount of seismicity that occurs after shut-in at 20 years. These results demonstrate two obvious characteristics: 1) von Kármán parameters do not appear to strongly affect the spatial distribution of seismicity, and 2) there is a consistent pattern of concentric circles formed

Parameter	Value
a	0.01
b	0.014
D_c	$1{\cdot}10^{-5}$ m
μ_0	0.6
σ_0	100
θ_0	1000 years
α	0.05
V^*	$1{\cdot}10^{-6}$ m/s

Table 4.2: Rate- and state parameters used in the initial simulations of induced earthquakes with the different von Kármán realizations of the initial shear stress shown in Figure 4.3

by small events (*i.e.* aftershocks) that occur along the edges of $M_w > 3$ ruptures. This spatial pattern is concerning because most observations of actual induced seismicity do not show this pattern but instead typically form a diffuse cloud of events whose outer boundary migrates outward at a rate given by that of the diffusion of fluids (Shapiro and Dinske, 2009; Keranen et al., 2014). Hence, this bullseye-like pattern is undesirable. We address this characteristic of the simulation results in the Section 4.2.3 through adjustment of the rate-state frictional parameters.

4.2.3 Effect of Rate- and State-parameters on Induced Earthquakes

The rate- and state-dependent constitutive law (Equations 4.4 and 4.5) includes several parameters that control earthquake nucleation, rupture propagation, and the time-

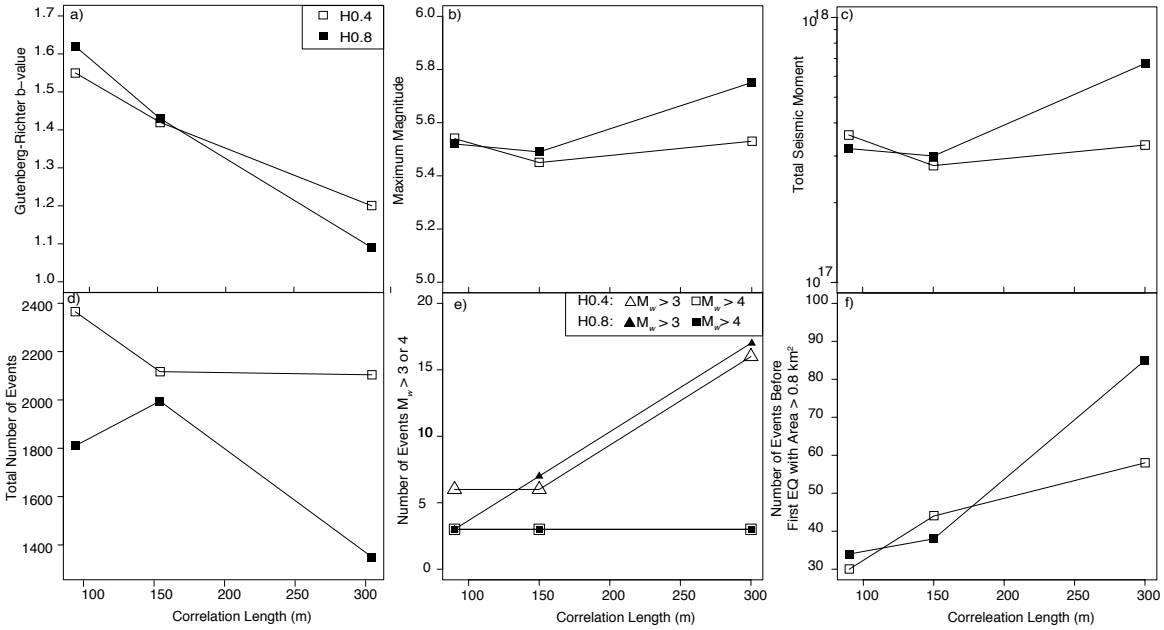

Figure 4.4: Catalog statistics for induced earthquakes by Hurst number as a function of the correlation length. a) Gütenberg-Richter b-value, b) Maximum earthquake magnitude, c) Total seismic moment, d) Total number of induced events, e) Number of events greater than M_w3 and M_w4, and f) Number of events before the first rupture of area greater than 0.08 km^2. All results for $H = 0.4$ as a function of correlation length $a_x = a_y = 90$ m, 150 m, and 300 m are given by the open squares and $H = 0.8$ by the filled squares [as in panel (a)], except for in panel (e) where results are given in the legend.

dependent earthquakes clustering phenomena such as aftershock and foreshock activity. The relevant parameters that we will consider include a, b, σ_0 and α. Combinations of some of the rate-states parameters appear in various equations that describe various aspects of earthquake behavior: $a\sigma$ in the earthquake rate equations (Dieterich, 1994, 2007) and $(b-a)$ in the approximate determination of earthquake stress drop $\left[i.e.\ \Delta\tau \approx \sigma(b-a)\ln\left(\frac{\theta_0 V^{EQ}}{D_c}\right)\right]$. Values of the constitutive parameters, a and b, constrained in laboratory experiments range from 0.01 to 0.02 (Dieterich, 1978). However, modeling of observed aftershock rates typically require very low values of the quantity $a\sigma$ (*i.e.* 0.05 MPa) in order to fit a rate- and state earthquake model to the observed sequences (Dieterich, 1994) [*i.e.* Section 2.2.5 of this

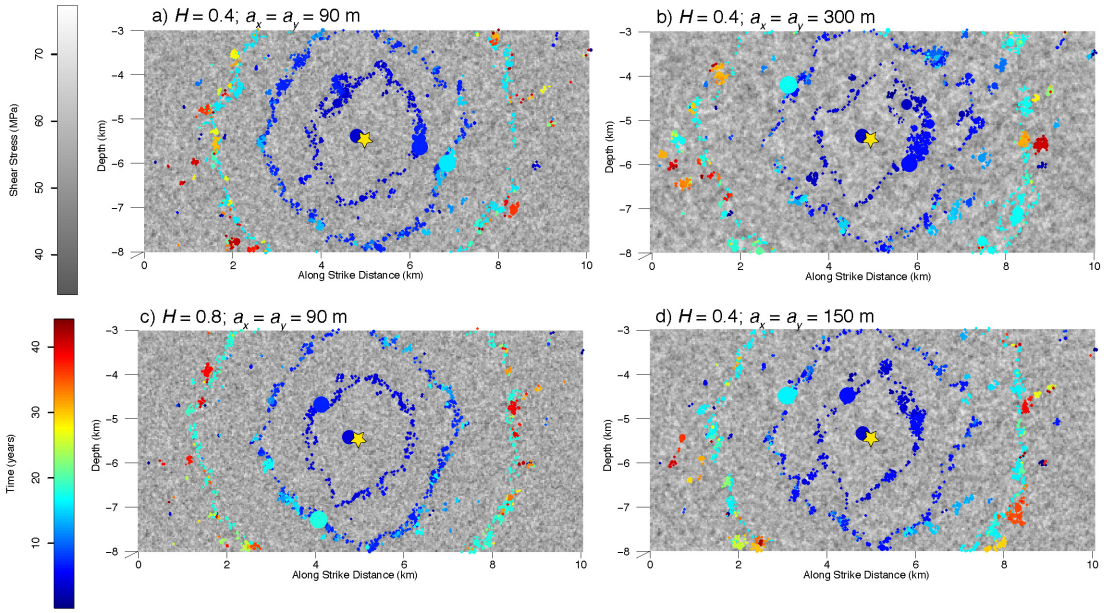

Figure 4.5: Hypocenter locations of induced earthquakes colored by time since injection began at 0 years . Shut-in occurs at 20 years. The well location is shown by the yellow star (1200 m out of the plane, 5000 m along strike, and -5500 m depth). Pre-stress is plotted in gray scale for values of the von Kármán correlated random field listed above each figure with a $\bar{\tau}_0 = 56$ MPa and a standard deviation of 5 MPa.

work, as well as Toda et al. (2005) and Kroll et al. (2013)]. In those studies, a may to be much lower than the laboratory derived value. If this condition is true, measurements of earthquake stress drop are also highly affected. Here, we show that simulations of injection induced earthquake sequences are extremely sensitive to variations in the quantity $(b - a)$ and σ.

Observations of injection induced earthquake sequences have demonstrated two important characteristics; 1) stress drops are reported to be a factor of 2-10 smaller than tectonic earthquakes (Reiter et al., 2012; Hough, 2014), and 2) seismicity often forms a diffusive cloud that migrates away from the wellbore in time with the pore-fluid pressure front generated by the injected fluid (Shapiro et al., 2002; Shapiro and Dinske, 2009; Kim,

2013; Keranen et al., 2014). To simulate induced seismicity sequences with characteristics that mirror the observations, we systematically vary the constitutive parameters, a and b, and the quantity $a\sigma$ (values are listed in Table 4.3) and test their effects on a set of metrics that characterize the simulated induced seismicity. These metrics include the following:

(a) Number of events during injection,

(b) Number of events post shut-in,

(c) Maximum earthquake magnitude during injection,

(d) The time of the largest event during injection,

(e) Maximum earthquake magnitude post shut-in,

(f) The time of the largest event post shut-in,

(g) Average earthquake stress drop (for $M_w > 2.5$),

(h) Cumulative seismic moment,

(i) The number of events before the first event with rupture area > 0.8 km^2,

(j) Magnitude of the first induced event,

Because we vary the initial normal stress in the simulations, the injection parameters must also be adjusted to avoid conditions where the pore-fluid pressure changes exceed the minimum compressive stress, which would lead to hydrofracturing can not be modeled by RSQSim. The complete set of injection parameters, normal stresses, and constitutive parameter values are listed in Table 4.3. For all simulations results shown in Figure 4.7, we use

a single realization of a von Kármán random stress field with $H = 0.8$, $a_x = a_y = 150$ m, to generate a pattern of pre-existing shear stress with a standard deviation of 1.5 MPa. However, we test the sensitivity to the random component of the initial stresses using two additional realizations of the pre-stress field with a somewhat higher standard deviation of 2 MPa (Figure 4.9). In all cases, we allow simulations to run for a period of 1000 years prior to beginning injection to allow any elements above steady-state, by definition in the process of spontaneously nucleating an earthquake, to continue the nucleation and then rupture. This ensures that all events that occur during the injection period would not have occurred in the absence of the pore-fluid pressure perturbations. We inject fluids at the specified injection rate from 1000 to 1020 years in the simulation. Figure 4.6 shows the pattern of pre-existing shear stress prior to the run and the evolved pattern after 1000 years of the simulation. In this example, $\bar{\tau_0} = 16$ MPa, $\tau_{max} = 19.37$ MPa, and there are 721 elements for which $\bar{\tau_0} > \tau_{max}$. Running the simulation for 1000 years results in 718 earthquakes that range in magnitude from $M_w 0.74$ to $M_w 2.79$. The last event to occur before the start of injection occurs 476 years prior to injection (524 years into the simulation). We set $\bar{\tau_0}$ to $\sim$85% of τ_{max} computed for the corresponding pore-fluid pressure history and the associated set of constitutive parameters. Results for the metrics listed above for each simulation are shown in Figures 4.7, 4.8, and 4.9.

In Figure 4.7 each of the 10 metrics listed above are plotted as both a function of the $(b - a)$ value where individual colored curves give results for various values of the quantity $a\sigma$. We find that the number of events during the injection and post shut-in

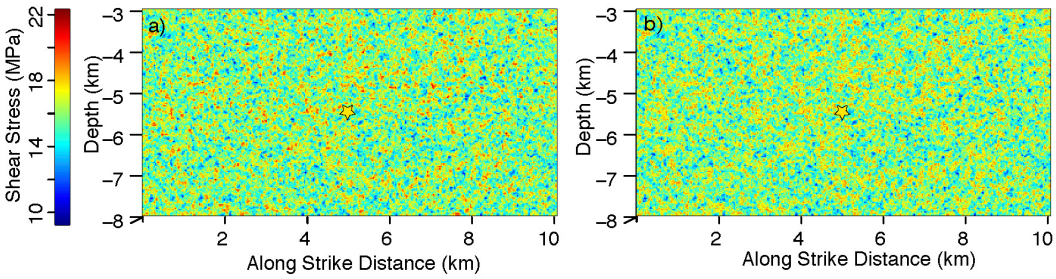

Figure 4.6: Shear stress on the fault surface. a) The pattern of pre-existing shear stress for one realization of the von Kármán field. Here, the shear stresses range from 9.27 MPa to 22.29 MPa with $\bar{\tau_0} = 16$ MPa. b) The pattern of shear stress after 1000 years of the simulated time prior to injection. $\bar{\tau_0}$ is still 16 MPa, however, now the range is 9.28 MPa to 19.47 MPa after 718 earthquakes. The well location is given by the yellow star.

σ (MPa)	a	Q (m^3/s)	P$_{max}$ (MPa)	τ_{min} (MPa)	τ_{max} (MPa)
30 MPa	0.002	0.01	9.6	13.02 to 14.29	18.92 to 20.62
30 MPa	0.003	0.01	9.6	12.99 to 14.25	18.92 to 20.62
30 MPa	0.005	0.01	9.6	12.95 to 14.20	18.92 to 20.62
30 MPa	0.007	0.01	9.6	12.93 to 14.17	18.92 to 20.62
30 MPa	0.01	0.01	9.6	12.91 to 14.14	18.92 to 20.62
60 MPa	0.001	0.02	19.2	26.18 to 28.67	37.8 to 41.25

Table 4.3: Rate- and state parameters, injections parameters, pore-fluid pressure change, τ_{min} and τ_{max} values. For each row in this table there is a series of runs in which b varies such that $b-a$ varies from 0.0014 to 0.0040. Injection parameters are specifically chosen to ensure a constant ratio of pore-fluid pressure change to initial normal stress. κ, ϕ, and c are held constant at 0.003 m^2/s, 0.05, and $5{\cdot}10^{-16}$ $/MPa$, respectively. These conditions were used to test the effects of $(b-a)$ and $a\sigma$ on simulated induced seismicity. Results are shown in Figures 4.7, 4.8, and 4.9.

periods decreases with increasing $(b-a)$ (Figures 4.7a & b), while the maximum magnitude during injection and the total seismic moment increase with increasing $(b-a)$ (Figures 4.7c & h). Furthermore, Figure 4.7g shows that the average stress drop for all events in a given

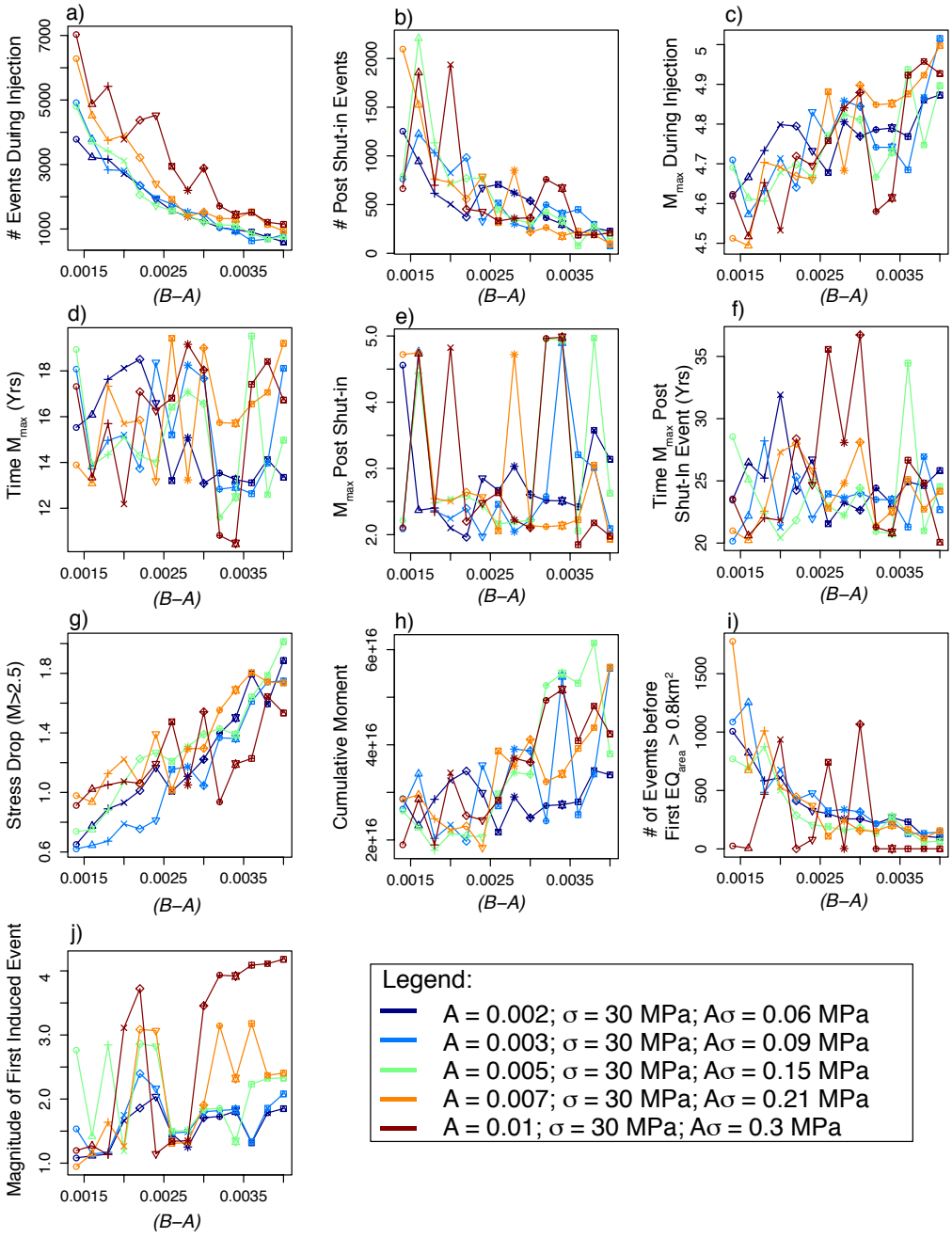

Figure 4.7: Ten metrics (listed in text) describing the induced earthquakes as a function of $(b-a)$ and $a\sigma$. Individual curves represent different values of $a\sigma$, listed in legend. We vary the $(b-a)$ term by increasing the value of the b parameter.

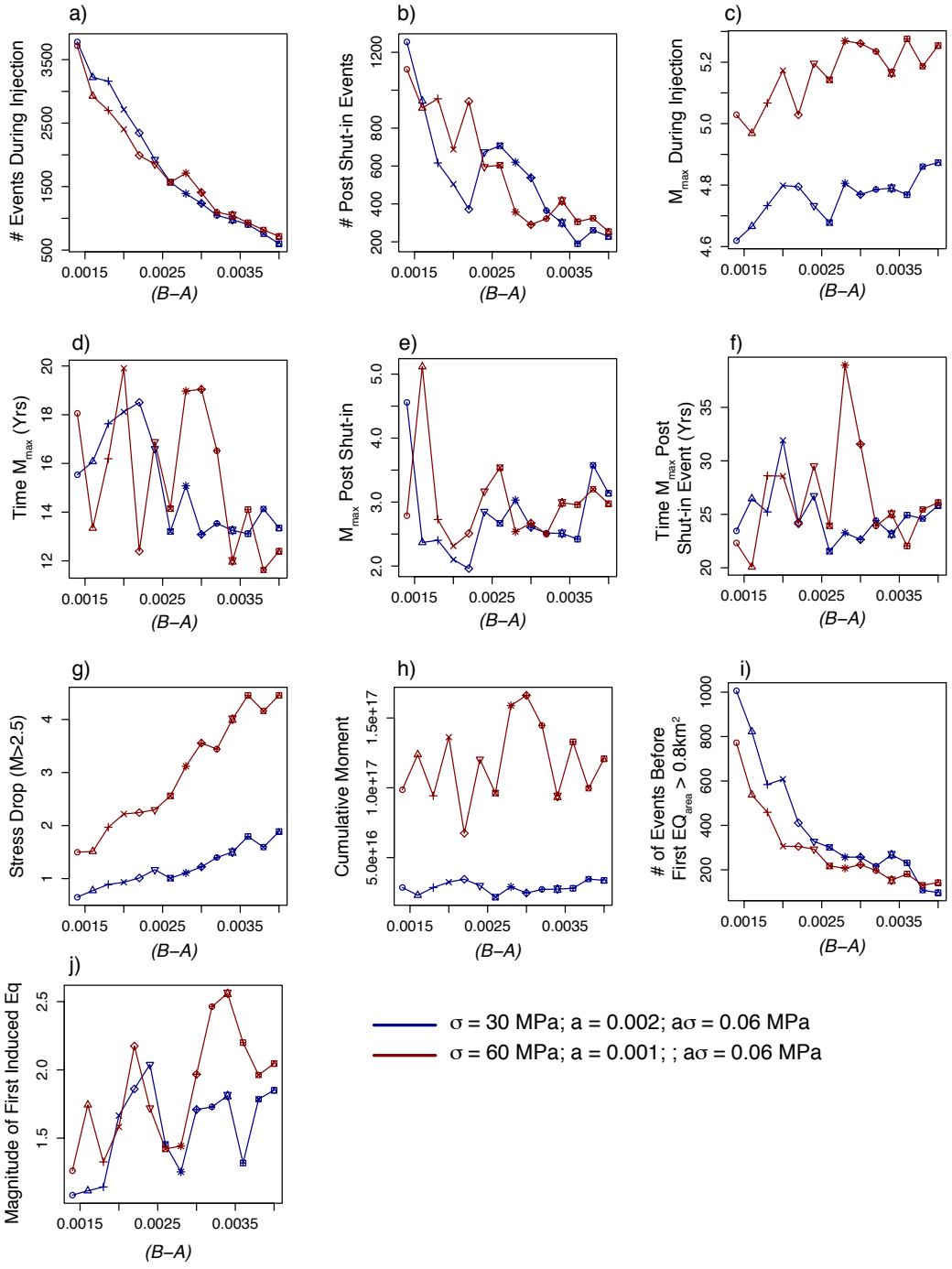

Figure 4.8: Ten metrics (listed in text) describing induced earthquakes as a function on $(b-a)$ for two different values of initial normal stress.

simulation greater than $M_w 2.5$ increases with increasing in $(b - a)$. The combination of increasing stress drop and increasing maximum magnitude with increasing $(b - a)$ acts to reduce the total number of events because it take a larger increase of fluid pressure (decrease of effective stress) to induce additional earthquakes.

Lastly, the spatial pattern of seismicity transitions between a diffusive cloud that migrates outward with time, to that of the bulls-eye pattern shown in Figure 4.5. We quantify this effect in terms of the number of events that occur prior to the first "sizeable" event. We define "sizeable" as an event with a rupture area larger than 0.8 km^2 (*i.e.* based on the area of a circular rupture with 500 m radius). Visually this transition occurs for $(b - a)$ values between 0.002 and 0.0026 (Figure 4.10). Graphically, this transition can be seen in Figure 4.7i, where the curves transition from a relatively steep slope, to the flat falloff, near $(b - a) = 0.002$. Lastly, Figure 4.7a suggests a modest dependency of the number of events during the injection period on the quantity $a\sigma$, though from these results, it is not clear whether this dependency is due to a or σ, specifically. Figures 4.7 d, e, f, and j show no obvious relationship with the value of $(b - a)$.

We explore the possible dependencies of the listed metrics to changes in initial normal stress with constant $a\sigma$ in Figure 4.8. Increasing the initial normal stress by a factor of 2, causes an approximately proportional increase of the stress drop (Figure 4.8g), the cumulative seismic moment (Figure 4.8h) and the maximum magnitude during injection increases by $\sim$0.4 magnitude units (Figure 4.8c). The other metrics show no obvious relationship to the initial normal stress.

Finally, we consider the dependencies of the metrics to random variations in the

pattern of initial shear stress, by considering two alternate realizations of von Kármán initial stress field and with a larger standard deviation of 2.0 MPa (compared to 1.5 MPa used for the above simulations). The simulation results are summarized in Figure 4.9. The number of events, maximum magnitude, stress drop, and number of events prior to the first sizeable event (panels (a), (b), (c), (g), (h), (i), in Figures 4.7 and 4.9) as a function of $(b-a)$ are consistent for the alternate realizations of the pre-stress pattern and with a larger standard deviation of the initial shear stress, in this case equal to 2 MPa. Again, there is no obvious relationship between the metrics in panels (d), (e), (f), and (i) and the value of $(b-a)$.

We select a set of preferred parameters from these experiments that explore the rate-state and von Kármán parameter space with which to further simulate injection induced seismicity. Our preferred parameters (Table 4.4) include those that produce results that mirror the observations of induced seismicity sequences which include: 1) spatially diffusive cloud-like distribution of seismicity that migrates away from the well with time along the pressure front, 2) a number of small magnitude events prior to the first sizeable event in the simulations, and 3) relatively low stress drops. In the following section (Section 4.3), we investigate the effects of the reservoir characteristics on injection induced seismicity.

4.3 Effects of Hydraulic Diffusivity on Post Shut-In Seismicity

Some regulatory agencies and energy companies have adopted the use of traffic light systems as a means of mitigating the hazard associated with injection operations.

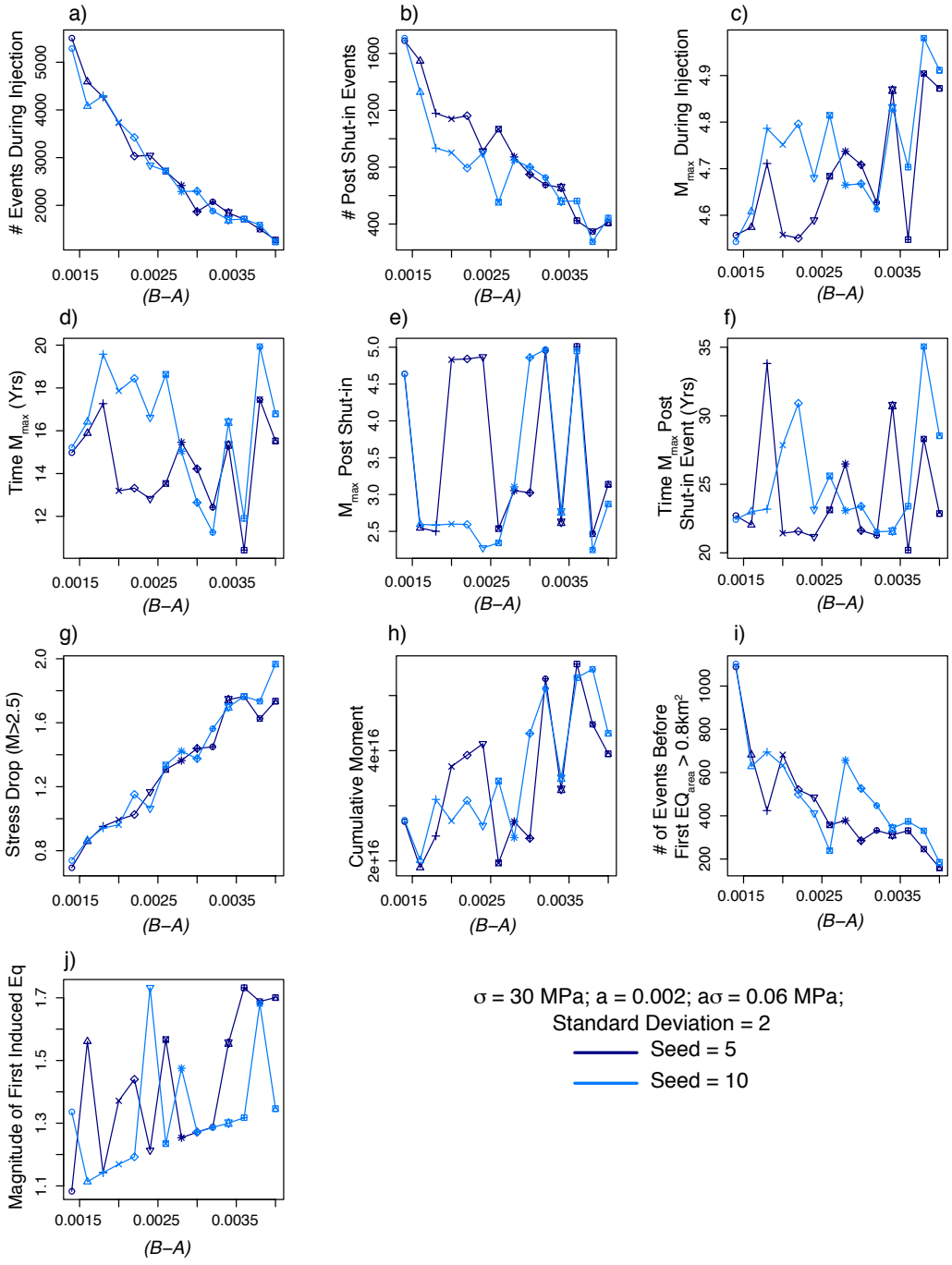

Figure 4.9: Ten metrics (listed in text) describing induced earthquake sequences as a function of $(b-a)$. The two different colored symbols and curves show results from simulations using initial shear stress distributions given by two different realizations of a von Kármán correlated random field, each with $H = 0.8$, $a_x = a_y = 150$ m, and a standard deviation of 2 MPa (33% higher than value used in Figure 4.7).

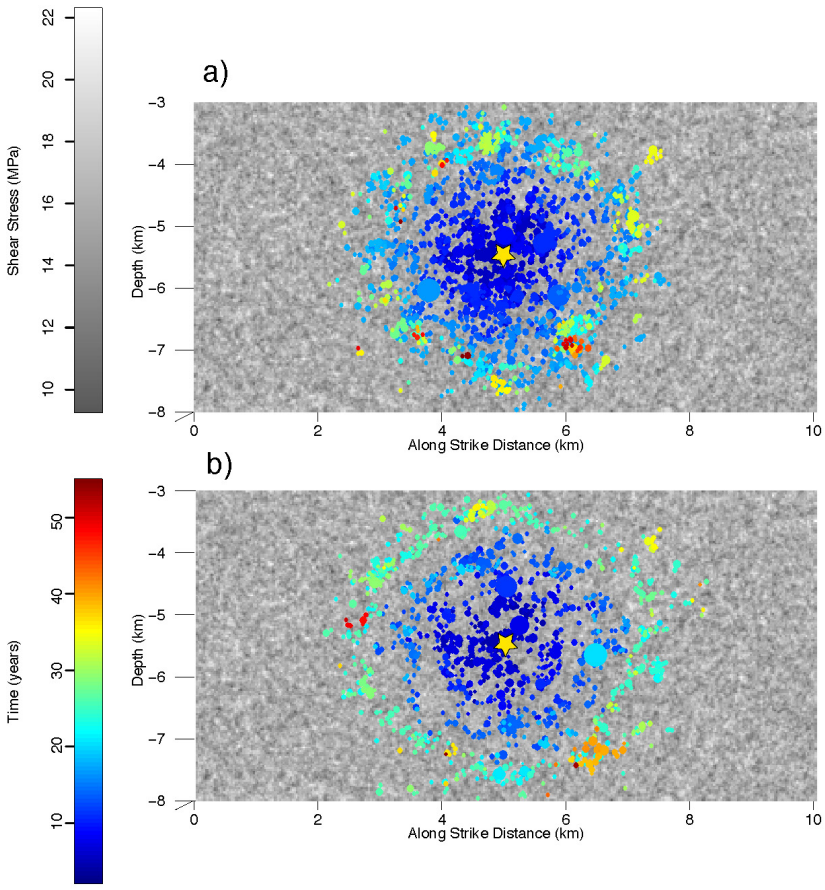

Figure 4.10: Hypocenter locations of induced earthquakes colored by time since injection began at 0 years and shut-in at 20 years. The well is located 1200 m out of the plane is given by the yellow star. Pre-stress is plotted in gray scale for von Kármán correlated random field with $H = 0.8$, $a_x = a_y = 150$ m, a $\bar{\tau_0} = 16$ MPa and a standard deviation of 1.5 MPa. a) Spatial pattern of events with $(b - a) = 0.002$ shows a diffusive cloud of seismicity, b) Spatial pattern of events with $(b - a) = 0.003$ demonstrating the transition to the bulls-eye pattern that persists at higher $(b - a)$ values $= 0.004$, such as those shown in Figure 4.5

Traffic light systems allow for low levels of seismic activity, but require the operator to modify injection operations if pre-established magnitude or ground motion thresholds are exceeded and halt injection completely if higher thresholds are exceeded (National Research Council, 2013). Enhanced geothermal operations in Basel, Switzerland provide a noteworthy (but unsuccessful) example of the use of a traffic light system. Because the area around the proposed geothermal field was known to be seismically active prior to beginning stimulation, the project operators installed seismic monitoring equipment and developed a traffic light procedure for the project. The beginning of stimulation operations were accompanied by a large increase in the number of small earthquakes including the occurrence of a M2.6 and a M2.7 event (Häring et al., 2008; Deichmann and Giardini, 2009). These events exceeded the tolerance threshold and the well was shut-in in accordance with the established traffic light protocol. Seismicity continued after the well was shut-in which lead operators to perform a bleed-off test, whereby pressure was decreased by production from the injection well. Within hours a M3.4 event occurred, the largest of the sequence, and was followed by three additional M>3 events in the coming weeks (Häring et al., 2008; Deichmann and Giardini, 2009). Although the operators followed the establish protocol including cessation of injection, these methods did not prevent further earthquakes. This phenomenon demonstrates that discontinuing injection operations or even producing fluid from a well in order to decrease pore-fluid pressure may not eliminate the hazard of post shut-in seismicity or even the occurrence of larger events than previously detected.

The occurrence of post shut-in seismicity is controlled by two factors: 1) reservoir characteristics and 2) delayed nucleation resulting from the rate-state properties of faults.

In the first case, the pore-fluid pressure may continue to rise at large distances from a well even after injection operations are terminated and the well is shut-in. This characteristic is controlled by the hydraulic diffusivity of the reservoir which is a function of the reservoir porosity, permeability, and compressibility and the fluid viscosity. As shown in Figure 4.2b, at distances of 4000 m or more, the pore-fluid pressure continues to rise for up to a decade or more after shut-in when the diffusivity is low. Alternatively, the pore-fluid pressure decays very quickly after shut-in for high diffusivity (Figure 4.2a).

The second factor controlling post shut-in seismicity involves time-dependent nucleation effects that are an inherent property of the rate-state constitutive law. This occurs when the stress rises above steady-state, it enters into the nucleation phase of the earthquake cycle (Equation 4.6). Nucleation phase is a largely self-driven process governed by accelerating slip leading to failure (Dieterich, 1992, 1994). The initial slip speed, which is determined by τ, σ and θ, controls the time to instability of an earthquake source (Dieterich, 1994). Slip speed during the earthquake nucleation phase remains very small until a short time prior to failure (Dieterich, 1994). Hence, an earthquake source may remain in the nucleation phase for quite some time before failure; this concept is known as delayed nucleation. It is typical of delayed nucleation with rate-and state-dependent friction to exhibit a power-law decay with a slope near -1 similar to that of the $1/t^p$ Omori-Utsu aftershock decay law (Dieterich, 1994; Dieterich et al., 2015).

We examine the effects the hydraulic diffusivity and the rate-state fault properties on post shut-in seismicity by performing a series of simulations, jointly varying the injection rate and diffusivity such that the maximum pore-fluid pressure change at the fault element

closest to the well remains approximately constant ($P_{max} \approx 9.6$ MPa). We simulate induced earthquakes on a fault with three different realizations of the von Kármán pre-existing shear stress field for the set of preferred parameters from the experiments presented in the previous sections (Table 4.4) and a suite of injection parameters in Table 4.5. Figure 4.11 demonstrates that the spatial distribution of events, the total number of events during injection, and the number of post shut-in events are consistent among the various patterns of pre-stress which indicates that the von Kármán Hurst exponent and correlation length affect the resulting seismicity rather than different realizations with the same parameters.

We separate the simulated post shut-in earthquakes into two populations based upon whether the pore-fluid pressure is increasing or decreasing on the nucleation element at the time of rupture (blue versus red events, respectively in Figure 4.11). Post shut-in events that occur while the post shut-in pore-fluid pressure is still rising may be due to the increased pore-fluid pressures, delayed nucleation, or some combination of those mechanisms. However, the post shut-in event that occur while the pore-fluid pressure is decreasing can only be explained by time-dependent nucleation. Note that while post shut-in pressures at points distant from the injection well, the rates of seismicity may be constant or even increasing before decreasing (Figure 4.11c, f, i). In contrast, if events that occur while the pore-fluid pressure is decreasing are to be considered aftershocks by the delayed nucleation principle inherent to rate-state friction, then their rate should exhibit an Omori-like decay by $1/t^{-p}$. Therefore, we determine the earthquake rate for both populations of events individually and compute the best fitting decay curve, estimating the p-value in the Omori-Utsu earthquake rate law [Earthquake rate = $K/(c+t)^{-p}$]. Figure 4.12 shows the

slope of the best fitting curve of the earthquake rates for each population of events [*i.e.* those that occur while the pore-fluid pressure is increasing (blues) and those that occur while the pressure is decreasing (reds)] vary as a function of diffusivity. If seismicity rates were reflecting only rate-state fault properties, the slope of the best fitting line should be near -1, consistent with p-values of the Omori aftershock decay law, for constant stressing rates. Decay rates steeper than -1 are observed with the stressing rate decreases rapidly (*e.g.* logarithmic decay) (Dieterich, 1994). Observations of this effect are presented in Section 2.2.5 of this work. These results can be classified into two distinct populations that both appear to follow a power-law decay; those that occur while the pore fluid pressure is increasing with a fairly constant and marginally decaying rate with a slope (on a log-log plot) of ≈ -0.5 and the remaining which occur while the pore-fluid pressure is decreasing and decay by approximately the inverse of time squared. The slope of ≈ -0.5 for post shut-in events that occur while pore-fluid pressure is still increasing is comparable to the slope of events that occur during the injection period, suggesting these events are caused by the same mechanisms, just as though they occurred during the injection period. The decay rate of population of post shut-in events that occur while the pressure is dropping, reflect multiple governing processes which are related to the effective stressing rates and time-dependent nucleation. It is likely that stressing histories related to decreased pore-fluid pressures may exhibit a a functional form that subsequently effects the rate of decay.

As in Section 4.2.3, we develop metrics through which to quantify the effects

H	0.8	$a_x = a_y$	150 m
ϕ	0.05	c	$5{\cdot}10^{-16}$ $/MPa$
a	0.002	b	0.004
σ_0	30 MPa	$\bar{\tau_0}$	16 MPa
τ_{max}	19.37 MPa		

Table 4.4: Preferred set of von Kármán, injection, and rate-state parameters for simulations of injection induced seismicity.

Q (m^3/s)	κ (m^2/s)	Q (m^3/s)	κ (m^2/s)
0.01	0.003	0.012	0.004
0.0142	0.005	0.0164	0.006
0.0185	0.007	0.021	0.008
0.041	0.03	0.064	0.08
0.21	0.3	0.48	0.8

Table 4.5: Range of injection rates and diffusivities used in simulations investigating characteristics of post shut-in seismicity.

the hydraulic diffusivity has on post shut-in seismicity. These metrics are presented in Figure 4.13 and include the following:

(a) The ratio of the total number of post shut-in events to the total number of events during the injection period,

(b) The total number of injection period and post shut-in events,

(c) Maximum earthquake magnitude during the injection and post shut-in period,

We find that the ratio of the logarithm of the number of post shut-in event to the logarithm of those that occur during the injection period is inversely related to the hydraulic diffusivity (Figure 4.13a). Additionally, the logarithm of the number of post shut-in events also various inversely with the logarithm of the diffusivity (Figure 4.13b). The maximum post shut-in event magnitudes shown in Figures 4.13c suggest that the largest events usually occur during the injection period, except for in three of the 30 simulations. We do not yet consider this a conclusive result, as the maximum post shut-in event magnitude may vary depending on a number of factors including the duration of the injection and value of the mean pre-existing shear stress, therefore, this topic requires further consideration. While it may seem intuitive that the largest magnitude events will occur during injection given the increased pore-fluid pressure, there have been observations of the largest event occurring post shut-in [*i.e.* Basel, Switzerland (Häring et al., 2008; Deichmann and Giardini, 2009)].

4.4 Discussion

We have presented results from a method that couples a geomechanical reservoir model with the 3-D physics-based earthquake simulator, RSQSim, to investigate the relationship between fluid injection and the resulting seismicity. Such methods provide a means to conduct experiments to investigate the effects of injection parameters, reservoir characteristics, and the physics that control earthquake occurrence on the spatio-temporal characteristics of injection induced seismicity. Insight gained from these models can aid in development of best practice protocols for injection operations, site-specific models of injection induced earthquakes, and probabilistic hazard assessments of potentially induced earthquakes.

In this work, we have systematically investigated the relationship between four model components and the resulting induced seismicity sequences. These components include 1) parameters that control the fractal distribution of pre-existing shear stress (H, a_x, and a_y), 2) the value of the rate-state constitutive parameters (a and b), 3) the initial normal stress σ_0, and 4) hydraulic diffusivity. Results indicate that the frequency-magnitude distribution of events is quite sensitive to the length scale of the pre-stress heterogeneity. For example, the number of M>3 events increases with increasing correlation length of the von Kármán field which results in fewer 1.5<M_w <2.5 events, thereby decreasing the Gütenberg-Richter b-value. Additionally, observed seismicity sequences have been shown to exhibit a diffusive behavior, migrating away from the well with time along the pressure front caused by injection. We find that this type of behavior is reproduced in our simulations if we use small values of $b - a$ and/or large correlation lengths in the pre-stress.

Specifically, we quantify this behavior in terms of the number of events prior to the first sizeable event in the simulation and find that this number increases with the von Kármán correlation length and decreases with $(b-a)$. This advancement since our initial modeling effort (Dieterich et al., 2015) is important because current mitigation procedures are based on the notion that small, premonitory earthquakes will occur before a larger, more widely felt, and potentially damaging earthquake.

We also investigate how other characteristics of injection-induced seismicity are affected by the rate-state properties on faults. Results indicate that earthquake magnitudes and stress drops are highly sensitive to $(b-a)$. Because earthquake stress drop scales directly with the quantity $\sigma(b-a)$, increasing $(b-a)$ leads to larger magnitude events with higher stress drops. In turn, this decreases the total number of events because most of the effective stress is released in the few large events and it takes longer for pore-fluid pressure to increase. Additionally, increasing the initial normal stress (σ_0) leads to a nearly linear increase in the stress drop.

Lastly, we investigate the effects of hydraulic diffusivity on post shut-in seismicity. It has been suggested that termination of injection operations by way of well shut-in may decrease the likelihood of future earthquakes. Our results support the hypothesis that post shut-in seismicity is highly sensitive to the hydraulic diffusivity of the reservoir. Pore-fluid pressures in a highly permeable reservoir respond quickly to applied stress, therefore the effective normal stress will also recover quickly after a well is shut-in, decreasing the likelihood of events directly related to increases in pore-fluid pressure. However, this does not preclude aftershocks of previously induced events which are caused by a delayed nucleation

mechanism inherent to the rate- and state properties of faults. Furthermore, for reservoirs with low diffusivity, the pore-fluid pressure will continue to rise at distant locations long after shut-in. Post shut-in seismicity controlled by the continued rise in pore-fluid pressure continues after shut-in at a rate similar to that during the injection period. However, seismicity related to the delayed nucleation mechanism decays at a rate closer to the inverse of time squared, faster than traditional Omori-like decay of aftershock sequences. The slope of the best-fitting curve of the seismicity rate increases toward -1 with increasing diffusivity. This suggests that an additional mechanism related to the decay of pore-fluid pressure drives the rate of event decay; which is a topic that requires further analysis. It may be that the recovery of normal stress while the pore-fluid pressure decreasing acts to clamp the fault and shutdown seismicity on the time scale related to the diffusivity of the reservoir. Additionally, further analysis is required to determine the relationship between hydraulic diffusivity and large post shut-in earthquakes.

4.5 Conclusions

The work presented here builds upon our initial investigation of seismicity related to fluid injection (Dieterich et al., 2015). We systemically investigate how several important parameters of the vast parameter space affect induced seismicity sequences on a single planar fault with a fractal distribution of pre-existing shear stress. We show that the Gútenberg-Ritcher b-value decreases with the maximum correlation length of the random stress field. Additionally, we find that the relationship between the rate-state constitutive parameters, a and b, significantly affects the spatial pattern of injection induced seismicity, where low

values of the quantity $(b - a)$ produce a diffusive cloud of seismicity that migrates away from the well with time. The number of events during the injection and post shut-in periods decrease with increasing $(b-a)$, however the stress drop, cumulative moment, and maximum magnitude increase with increasing $(b - a)$ and $a\sigma$. Through this analysis, we determine a set of preferred parameters that generate simulated seismicity with characteristics similar to that of observed induced seismicity sequences. We use the preferred parameters to investigate the effects of hydraulic diffusivity on post shut-in seismicity. Results show that two populations of events occur post shut-in which are related to post shut-in increases in pore-fluid pressure, time-dependent nucleation, or some combination of the two. This work represents a preliminary effort to determine the effects of diffusivity on post shut-in seismicity and many more experiments are required to fully understand this relationship. In particular, we are interested in exploring: 1) the possibility that characteristics of seismicity during the injection period may provide information about post shut-in events, 2) the efficacy of shut-in at preventing further seismic activity and 3) under what conditions this might be considered a useful tool to mitigate seismic hazard.

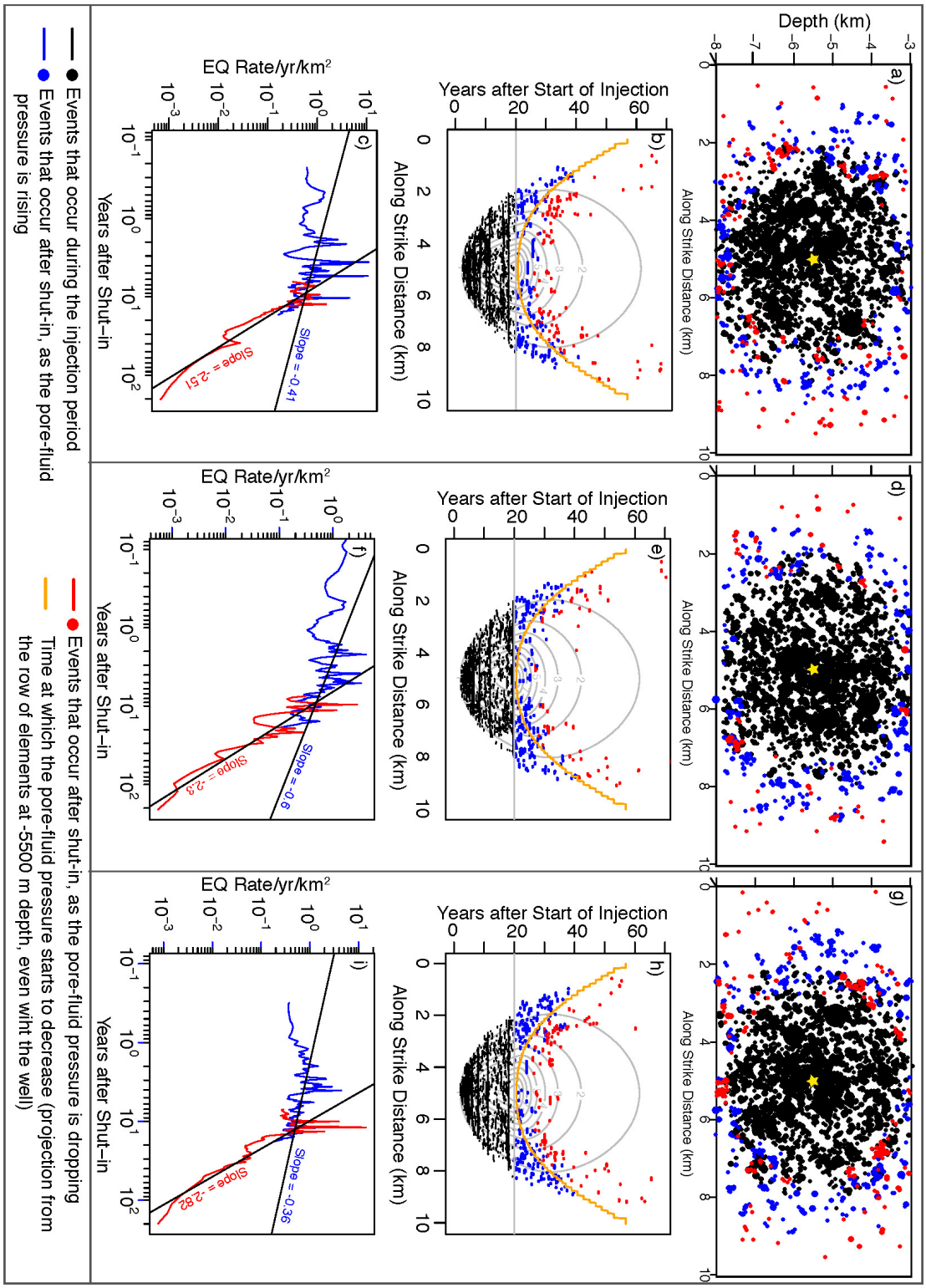

Figure 4.11: (Caption on following page)

Figure 4.11: (Previous page.) Hypocenter locations and rate of post shut-in seismicity for three realizations (panels $(a-c)$, $(d-f)$, $(g-i)$ of the von Kármán field of pre-existing shear stress ($H = 0.8$; $a_x = a_y = 150$ m; $\bar{\tau_0} = 16$ MPa; standard deviation = 1.5 MPa). All events are colored by the time at which they occur in the simulation with black symbols indicating an event that occurred during the injection period, blue symbols indicating an event that occurred post shut-in, but as the pore-fluid pressure was still rising on the hypocentral element, and red symbols indicating an event that occurred post shut-in, but as the pore-fluid pressure was falling on the hypocentral element. The well location is projected onto the fault surface in the location of the yellow star $a, d, g)$ Profile view of the fault surface with hypocentral locations of all events that occurred after the start of injection. Symbols are scaled with event magnitude. $b, e, h)$ Space-time plot showing the along strike extent of each rupture (colored horizontal lines). Shut-in occurs at 20 years after beginning injection (gray horizontal line). Gray contours show the pore-fluid pressure for the row of elements at -5500 m depth, level with the location of the well. Orange stepped line shows the time that the pore-fluid pressure began to decrease on each element in the same row. All events are projected onto the -5500 m surface, therefore some events in blue appear to occur after the pore-fluid pressure is decreasing (*i.e.* inside the orange curve), however the hypocenters of these events are simply up/down dip of the location of the well, but at a similar along strike distance [as shown in panels (a), (d), and (g)]. $c, f, i)$ The rate of post shut-in seismicity for events that occur while the pore-fluid pressure is rising (blue) and after the pore-fluid pressure begins to decrease (red) on the hypocentral element. Because the area of the fault affected by pressure increase or pressure decrease is constantly changing, the earthquake rates for each population are normalized by the corresponding fault area.

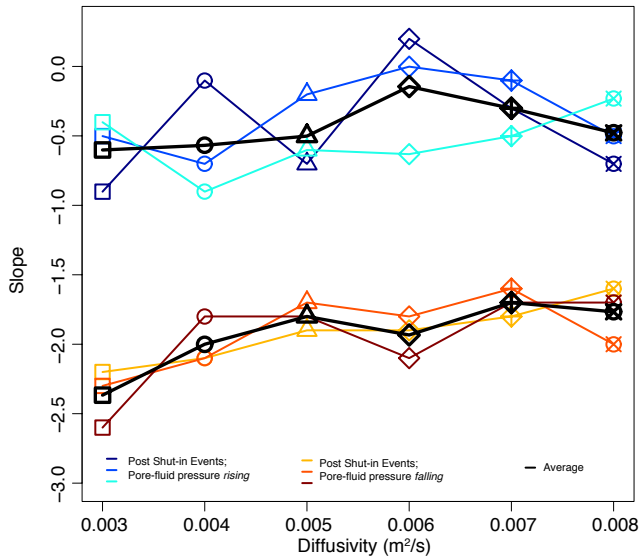

Figure 4.12: Slope of best-fitting curve to the rates of post shut-in earthquakes as a function of diffusivity. If the rate of seismicity were to obey Omori's law, the slope of the best fitting line is equivalent to the p-value in the modified Omori law for aftershock decay. Blue curves are slopes of the best-fitting line to rates of post shut-in events that occur while pore-fluid pressure is increasing on the hypocentral element, while the red curves are slopes of the best-fitting rates of post shut-in events that occur while the pore-fluid pressure is decreasing. The black curves represent the average slope for each measurement at a given diffusivity.

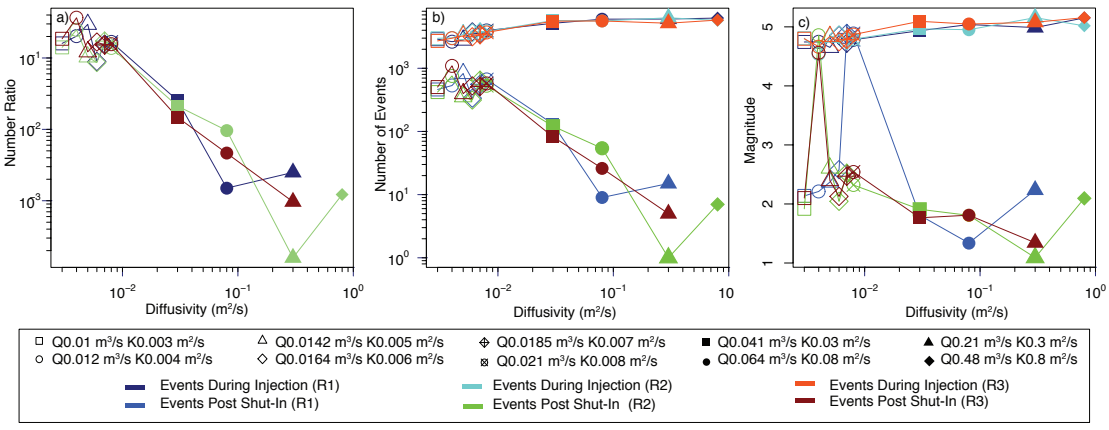

Figure 4.13: Three metrics (discussed in text) demonstrating the relationship between injection induced seismicity sequences and the hydraulic diffusivity. Results are from three different realizations of the von Kármán pre-existing shear stress field ($R1, R2$, and $R3$). a) Ratio of the number of post shut-in earthquakes to the number that occur during the injection period. b) Total number of events during injection and the total number of post shut-in events. c) Maximum event magnitude during the injection and post shut-in periods.

Bibliography

Ake, J., K. Mahrer, D. O'Connell, and L. Block (2005). Deep-injection and closely monitored induced seismicity at paradox valley, colorado. Bulletin of the Seismological Society of America 95(2), 664–683.

Allam, A. and Y. Ben-Zion (2012). Seismic velocity structures in the southern california plate-boundary environment from double-difference tomography. Geophysical Journal International 190(2), 1181–1196.

Andrews, D. and Y. Ben-Zion (1997). Wrinkle-like slip pulse on a fault between different materials. Journal of Geophysical Research: Solid Earth (1978–2012) 102(B1), 553–571.

Andrews, D. J. (1976). Rupture velocity of plane strain shear cracks. J. Geophys. Res. 81, 5679–5687.

Barall, M. (2008). FaultMod finite element code.

Barall, M. (2009). A grid-doubling finite-element technique for calculating dynamic three-dimensional spontaneous rupture on an earthquake fault. Geophys. J. Int. 178, 845–859.

Barbot, S., Y. Fialko, and Y. Bock (2009). Postseismic deformation due to the mw 6.0 2004 parkfield earthquake: Stress-driven creep on a fault with spatially variable rate-and-state friction parameters. Journal of Geophysical Research: Solid Earth (1978–2012) 114(B7).

Barth, N., C. Boulton, B. Carpenter, G. Batt, and V. Toy (2013). Slip localization on the southern alpine fault, new zealand. Tectonics 32(3), 620–640.

Bedrosian, P. A., M. J. Unsworth, and G. Egbert (2002). Magnetotelluric imaging of the creeping segment of the san andreas fault near hollister. Geophysical Research Letters 29(11), 1–1.

Belardinelli, M. E., M. Cocco, O. Coutant, and F. Cotton (1999). Redistribution of dynamic stress during coseismic ruptures: Evidence for fault interaction and earthquake triggering. Journal of Geophysical Research: Solid Earth (1978–2012) 104(B7), 14925–14945.

Ben-Zion, Y., M. Eneva, and Y. Liu (2003). Large earthquake cycles and intermittent criticality on heterogeneous faults due to evolving stress and seismicity. Journal of Geophysical Research: Solid Earth (1978–2012) 108(B6).

Bozkurt, E. and A. Koçyiðit (1996). The Kazova basin: an active negative flower structure on the Almus Fault Zone, a splay fault system of the North Anatolian Fault zone, Turkey. Tectonophysics 265(3), 239–254.

Burchfiel, B. and J. Stewart (1966). "Pull-apart" origin of the central segment of Death Valley, California. Geological Society of America Bulletin 77(4), 439–442.

Candela, T., F. Renard, M. Bouchon, A. Brouste, D. Marsan, J. Schmittbuhl, and C. Voisin (2009). Characterization of fault roughness at various scales: Implications of three-dimensional high resolution topography measurements. Pure and Applied Geophysics 166(10-11), 1817–1851.

Cattania, C., S. Hainzl, L. Wang, B. Enescu, and F. Roth (2015). Aftershock triggering by postseismic stresses: A study based on coulomb rate-and-state models. Journal of Geophysical Research: Solid Earth 120(4), 2388–2407.

Cochran, E., K. Richards-Dinger, K. Kroll, R. Harrington, and J. Dieterich (2013). Using an earthquake simulator to model tremor along a strike slip fault. In AGU Fall Meeting Abstracts, Volume 1, pp. 2452.

Colella, H. V., J. H. Dieterich, K. Richards-Dinger, and A. M. Rubin (2012). Complex characteristics of slow slip events in subduction zones reproduced in multi-cycle simulations. Geophysical Research Letters 39(20), n/a–n/a.

Colella, H. V., J. H. Dieterich, and K. B. Richards-Dinger (2011). Multi-event simulations of slow slip events for a Cascadia-like subduction zone. Geophys. Res. Lett. 38, L16312.

Cotton, F. and O. Coutant (1997). Dynamic stress variations due to shear faults in a plane-layered medium. Geophysical Journal International 128(3), 676–688.

Crowell, J. C. (1974). Origin of late Cenozoic basins in southern California.

Daniel, G., D. Marsan, and M. Bouchon (2006). Perturbation of the izmit earthquake aftershock decaying activity following the 1999 mw 7.2 düzce, turkey, earthquake. Journal of Geophysical Research: Solid Earth (1978–2012) 111(B5).

Das, S. and K. Aki (1977). A numerical study of two-dimensional spontaneous rupture propagation. Geophysical Journal International 50(3), 643–668.

Day, S. M. (1982). Three-dimensional simulation of spontaneous rupture: the effect of nonuniform prestress. Bulletin of the Seismological Society of America 72(6A), 1881–1902.

Deichmann, N. and D. Giardini (2009). Earthquakes induced by the stimulation of an enhanced geothermal system below basel (switzerland). Seismological Research Letters 80(5), 784–798.

Dieterich, James, H. (1978). Time-dependent friction and the mechanics of stick-slip. Pure Appl. Geophys. 116, 790–806.

Dieterich, James, H. (1979). Modeling of rock friction, 1. Experimental results and constitutive equations. J. Geophys. Res. 84, 2161–2169.

Dieterich, James, H. (1981). Constitutive properties of faults with simulated gauge. Mechanical Behavior of Crustal Rocks, Geophys. Monogr. Ser. 24, 103–120.

Dieterich, James, H. (1992). Earthquake nucleation on faults with rate- and state-dependent strength. Tectonophysics 211, 115–134.

Dieterich, James, H. (1994). A constitutive law for rate of earthquake production and its application to earthquake clustering. J. Geophys. Res. 99, 2601–2618.

Dieterich, James, H. and B. Richards-Dinger, Keith (2010). Earthquake recurrence in simulated fault systems. PAGEOPH.

Dieterich, J. (2007). Applications of rate-and state-dependent friction to models of fault slip and earthquake occurrence. Treatise on Geophysics 4, 107–129.

Dieterich, J. H., K. B. Richards-Dinger, and K. A. Kroll (2015). Modeling injection-induced seismicity with the physics-based earthquake simulator rsqsim. Seismological Research Letters.

Dieterich, J. H. and D. E. Smith (2010). Nonplanar faults: mechanics of slip and off-fault damage. In Mechanics, Structure and Evolution of Fault Zones, pp. 1799–1815. Springer.

Duan, B. and D. Oglesby, David (2006). Heterogeneous fault stresses from previous earthquakes and the effect on dynamics of parallel strike-slip faults. J. Geophys. Res. 111.

Dunham, E. M. (2007). Conditions governing the occurrence of supershear ruptures under slip-weakening friction. Journal of Geophysical Research: Solid Earth (1978–2012) 112(B7).

Ellsworth, W. L. (2013). Injection-induced earthquakes. Science 341(6142), 1225942.

Fay, N. P. and E. D. Humphreys (2005). Fault slip rates, effects of elastic heterogeneity on geodetic data, and the strength of the lower crust in the salton trough region, southern california. Journal of Geophysical Research: Solid Earth (1978–2012) 110(B9).

Felzer, K. R., T. W. Becker, R. E. Abercrombie, G. Ekström, and J. R. Rice (2002). Triggering of the 1999 mw7.1 Hector Mine earthquake by aftershocks of the 1992 mw7.3 Landers earthquake. Journal of Geophys. Res. 107, 2190.

Felzer, K. R. and E. E. Brodsky (2005). Testing the stress shadow hypothesis. Journal of Geophysical Research: Solid Earth (1978–2012) 110(B5).

Field, E. H., R. J. Arrowsmith, G. P. Biasi, P. Bird, T. E. Dawson, K. R. Felzer, D. D. Jackson, K. M. Johnson, T. H. Jordan, C. Madden, et al. (2014). Uniform California Earthquake Rupture Forecast, Version 3 (UCERF3)—The Time-Independent Model. Bulletin of the Seismological Society of America 104(3), 1122–1180.

Fletcher, J. M., T. K. Rockwell, O. Teran, M. E, G. Faneros, K. W. Hudnut, J. Gonzales, A. Gonzalez, R. Spelz, and K. J. Mueller (2010). The surface ruptuers associated with the El Mayor-Borrego earthquake sequence. Geological Society of America Abstracts.

Fletcher, J. M., O. J. Teran, T. K. Rockwell, M. E. Oskin, K. W. Hudnut, K. J. Mueller, R. M. Spelz, S. O. Akciz, E. Masana, G. Faneros, et al. (2014). Assembly of a large earthquake from a complex fault system: Surface rupture kinematics of the 4 April 2010 El Mayor–Cucapah (Mexico) Mw 7.2 earthquake. Geosphere 10(4), 797–827.

Freed, A. M. (2005). Earthquake triggering by static, dynamic, and postseismic stress transfer. Annu. Rev. Earth Planet. Sci. 33, 335–367.

Freed, A. M. and J. Lin (1998). Time-dependent changes in failure stress following thrust earthquakes. Journal of Geophysical Research 103(B10), 24393–24409.

Freed, A. M. and J. Lin (2002). Accelerated stress buildup on the southern san andreas fault and surrounding regions caused by mojave desert earthquakes. Geology 30(6), 571–574.

Frohlich, C., W. Ellsworth, W. A. Brown, M. Brunt, J. Luetgert, T. MacDonald, and S. Walter (2014). The 17 may 2012 m4. 8 earthquake near timpson, east texas: an event possibly triggered by fluid injection. Journal of Geophysical Research: Solid Earth 119(1), 581–593.

Frohlich, C., C. Hayward, B. Stump, and E. Potter (2011). The dallas–fort worth earthquake sequence: October 2008 through may 2009. Bulletin of the Seismological Society of America 101(1), 327–340.

Gan, W. and C. Frohlich (2013). Gas injection may have triggered earthquakes in the cogdell oil field, texas. Proceedings of the National Academy of Sciences 110(47), 18786–18791.

Gomberg, J., N. Beeler, M. Blanpied, and P. Bodin (1998). Earthquake triggering by transient and static deformations. Journal of Geophysical Research: Solid Earth (1978–2012) 103(B10), 24411–24426.

Gomberg, J., P. Bodin, and P. A. Reasenberg (2003). Observing earthquakes triggered in the near field by dynamic deformations. Bulletin of the Seismological Society of America 93(1), 118–138.

Gu, J.-C., J. R. Rice, A. L. Ruina, and T. T. Simon (1984). Slip motion and stability of a single degree of freedom elastic system with rate and state dependent friction. Journal of the Mechanics and Physics of Solids 32(3), 167–196.

Häring, M. O., U. Schanz, F. Ladner, and B. C. Dyer (2008). Characterisation of the basel 1 enhanced geothermal system. Geothermics 37(5), 469–495.

Harris, Ruth, A. and M. Day, Steven (1993). Dynamics of Fault Interaction: Parallel Strike-Slip Faults. J. Geophys. Res. 98, 4461–4472.

Harris, Ruth, A. and M. Day, Steven (1999). Dynamic 3D simulations of earthquakes on en echelon faults. Geophys. Res. Let. 26, 2089–2092.

Harris, R., R. Archuleta, B. Aagaard, J. Ampuero, D. Andrews, L. Dalguer, S. Day, E. Dunham, G. Ely, Y. Kase, et al. (2004). The source physics of large earthquakes-validating spontaneous rupture methods. In AGU Fall Meeting Abstracts, Volume 1, pp. 05.

Harris, R., M. Barall, R. Archuleta, E. Dunham, B. Aagaard, J. Ampuero, H. Bhat, V. Cruz-Atienza, L. Dalguer, P. Dawson, et al. (2009). The SCEC/USGS dynamic earthquake rupture code verification exercise. Seismological Research Letters 80(1), 119–126.

Harris, R. A. (2004). Numerical simulations of large earthquakes: Dynamic rupture propagation on heterogeneous faults. Pure and Applied Geophysics 161(11-12), 2171–2181.

Harris, R. A. and R. W. Simpson (1996). In the shadow of 1857-the effect of the great ft. tejon earthquake on subsequent earthquakes in southern california. Geophysical Research Letters 23(3), 229–232.

Hauksson, E. (1994). State of stress from focal mechanisms before and after the 1992 landers earthquake sequence. Bull. Seism. Soc. Am. 84, 917–934.

Hauksson, E., W. Yang, and P. M. Shearer (2012). Waveform relocated earthquake catalog for southern California (1981 to 2011). Bull. Seism. Soc. Am.

Healy, J., W. Rubey, D. Griggs, and C. Raleigh (1968). The Denver earthquakes. Science 161(3848), 1301–1310.

Hearn, E. H., R. Bürgmann, and R. E. Reilinger (2002). Dynamics of izmit earthquake postseismic deformation and loading of the düzce earthquake hypocenter. Bulletin of the Seismological Society of America 92(1), 172–193.

Helmstetter, A. and B. E. Shaw (2006). Relation between stress heterogeneity and aftershock rate in the rate-and-state model. Journal of Geophysical Research: Solid Earth (1978–2012) 111(B7).

Hill, D., P. Reasenberg, A. Michael, W. Arabaz, G. Beroza, D. Brumbaugh, J. Brune, R. Castro, S. Davis, W. Ellsworth, et al. (1993). Seismicity remotely triggered by the magnitude 7.3 landers, california, earthquake. Science 260(5114), 1617–1623.

Holland, A. A. (2013). Earthquakes triggered by hydraulic fracturing in south-central oklahoma. Bulletin of the Seismological Society of America 103(3), 1784–1792.

Horton, S. (2012). Disposal of hydrofracking waste fluid by injection into subsurface aquifers triggers earthquake swarm in central arkansas with potential for damaging earthquake. Seismological Research Letters 83(2), 250–260.

Hough, S. E. (2014). Shaking from injection-induced earthquakes in the Central and Eastern United States. Bulletin of the Seismological Society of America.

Hsieh, P. A. and J. D. Bredehoeft (1981). A reservoir analysis of the denver earthquakes: A case of induced seismicity. Journal of Geophysical Research: Solid Earth (1978–2012) 86(B2), 903–920.

Ida, Y. (1972). Cohesive force across the tip of a longitudianl shear crack from Griffith's specific surface energy. J. Geophys. Res. 77, 3796–3805.

Jaumé, S. C. and L. R. Sykes (1996). Evolution of moderate seismicity in the san francisco bay region, 1850 to 1993: Seismicity changes related to the occurrence of large and great earthquakes. Journal of Geophysical Research: Solid Earth (1978–2012) 101(B1), 765–789.

Keranen, K. M., H. M. Savage, G. A. Abers, and E. S. Cochran (2013). Potentially induced earthquakes in Oklahoma, USA: Links between wastewater injection and the 2011 mw 5.7 earthquake sequence. Geology 41(6), 699–702.

Keranen, K. M., M. Weingarten, G. Abers, B. A. Bekins, and S. Ge (2014). Sharp increase in central oklahoma seismicity since 2008 induced by massive wastewater injection. Science 345(6195), 448–451.

Kilb, D., J. Gomberg, and P. Bodin (2000). Triggering of earthquake aftershocks by dynamic stresses. Nature 408(6812), 570–574.

Kim, W.-Y. (2013). Induced seismicity associated with fluid injection into a deep well in youngstown, ohio. Journal of Geophysical Research: Solid Earth 118(7), 3506–3518.

King, G. C. P., R. S. Stein, and J. Lin (1994). Static Stress Changes and the Triggering of Earthquakes. Bull. Seism. Soc. Am 84, 935–953.

Kirby, S. and A. Kronenberg (1987). Rheology of the lithosphere: selected topics. Reviews of Geophysics 25(6), 1219–1244.

Kroll, K. A., E. S. Cochran, K. B. Richards-Dinger, and D. F. Sumy (2013). Aftershocks of the 2010 mw 7.2 el mayor-cucapah earthquake reveal complex faulting in the yuha desert, california. Journal of Geophysical Research: Solid Earth 118(12), 6146–6164.

Langenheim, V., R. Jachens, D. Morton, R. Kistler, and J. Matti (2004). Geophysical and isotopic mapping of preexisting crustal structures that influenced the location and development of the san jacinto fault zone, southern california. Geological Society of America Bulletin 116(9-10), 1143–1157.

Lettis, W., J. Bachhuber, R. Witter, C. Brankman, C. Randolph, A. Barka, W. Page, and A. Kaya (2002). Influence of releasing step-overs on surface fault rupture and fault segmentation: Examples from the 17 august 1999 izmit earthquake on the north anatolian fault, turkey. Bull. Seism. Soc. Am. 92, 19–42.

Lin, J. and R. S. Stein (2004). Stress triggering in thrust and subduction earthquakes and stress interaction between the southern san andreas and nearby thrust and strike-slip faults. Journal of Geophysical Research: Solid Earth (1978–2012) 109(B2).

Linker, M. F. and H. Dieterich, James (1992). Effects of variable normal stress on rock friction: Observations and constitutive equations. J. Geophys. Res. 97, 4923–4940.

Llenos, A. L. and A. J. Michael (2013). Modeling earthquake rate changes in oklahoma and arkansas: Possible signatures of induced seismicity. Bulletin of the Seismological Society of America 103(5), 2850–2861.

Lozos, Julian, C., H. Dieterich, James, and D. Oglesby, David (2014). The Effects of d_0 on Rupture Propagation on Fault Stepovers. Bull. Seism. Soc. Am. 104.

Lozos, Julian, C., D. Oglesby, David, and N. Brune, James (2013). The Effects of Fault Stepovers on Ground Motion. Bull. Seism. Soc. Am. 103, 1922–1934.

Lozos, Julian, C., D. Oglesby, David, N. Brune, James, and B. Olsen, Kim (2012). Small intermediate fault segments can either aid or hinder rupture propagation at stepovers. Geophys. Res. Let. 39.

Lozos, J. C., D. D. Oglesby, J. N. Brune, and K. B. Olsen (2015). Rupture and Ground–Motion Models on the Northern San Jacinto Fault, Incorporating Realistic Complexity. Bulletin of the Seismological Society of America 105(4), 1931–1946.

Ma, K.-F. and C.-H. Chan (2005). Response of seismicity to Coulomb stress triggers and shadows of the 1999 $M_w = 7.6$ Chi-Chi, Taiwan, earthquake. Journal of Geophys. Res. 110, B05S19.

Maccaferri, F., E. Rivalta, L. Passarelli, and S. Jónsson (2013). The stress shadow induced by the 1975–1984 krafla rifting episode. Journal of Geophysical Research: Solid Earth 118(3), 1109–1121.

Madariaga, R. and K. B. Olsen (2000). Criticality of rupture dynamics in 3–D. Pure and Applied Geophysics 157(11-12), 1981–2001.

Mallman, E. P. and T. Parsons (2008). A global search for stress shadows. Journal of Geophysical Research: Solid Earth (1978–2012) 113(B12).

Mallman, E. P. and M. D. Zoback (2007). Assessing elastic coulomb stress transfer models using seismicity rates in southern california and southwestern japan. Journal of Geophysical Research: Solid Earth (1978–2012) 112(B3).

Marone, C. (1998). Laboratory-derived friction laws and their application to seismic faulting. Annual Review of Earth and Planetary Sciences 26(1), 643–696.

Marone, C. J., C. Scholtz, and R. Bilham (1991). On the mechanics of earthquake afterslip. Journal of Geophysical Research: Solid Earth (1978–2012) 96(B5), 8441–8452.

Marsan, D. and S. S. Nalbant (2005). Methods for measuring seismicity rate changes: A review and a study of how the M_w7.3 landers earthquake affected the aftershock sequence of the M_w6.1 joshua tree earthquake. pure and applied geophysics 162(6-7), 1151–1185.

Meng, X. and Z. Peng (2014). Seismicity rate changes in the salton sea geothermal field and the san jacinto fault zone after the 2010 mw 7.2 el mayor-cucapah earthquake. Geophysical Journal International 197(3), 1750–1762.

Meng, X., Z. Peng, and J. L. Hardebeck (2013). Seismicity around parkfield correlates with static shear stress changes following the 2003 mw6. 5 san simeon earthquake. Journal of Geophysical Research: Solid Earth 118(7), 3576–3591.

National Research Council (2013). Induced Seismicity Potential in Energy Technologies. Washington,Dc: The National Academies Press.

Ogata, Y. (1981). On lewis' simulation method for point processes. Information Theory, IEEE Transactions on 27(1), 23–31.

Oglesby, David, D. (2008). Rupture Termination and Jump on Parallel Offset Faults. Bull. Seism. Soc. Am. 98, 440–447.

Oglesby, D. D. (2005). The dynamics of strike-slip step-overs with linking dip-slip faults. Bulletin of the Seismological Society of America 95(5), 1604–1622.

Okada, Y. (1992). Internal deformation due to shear and tensile faults in a half-space. Bull. Seism. Soc. Am. 82, 1018–1040.

Olsen, K., R. Madariaga, and R. Archuleta (1997). Three-dimensional dynamic simulation of the 1992 Landers earthquake. Science 278(5339), 834–838.

Palmer, C. A. and J. R. Rice (1973). The growth of slip ssurface in the progressive failure of overconsolidated clay. Proc. Roy. Soc. Lond. 332, 527–548.

Parsons, T. and D. S. Dreger (2000). Static-stress impact of the 1992 landers earthquake sequence on nucleation and slip at the site of the 1999 m= 7.1 hector mine earthquake, southern california. Geophysical research letters 27(13), 1949–1952.

Peltzer, G., P. Rosen, F. Rogez, and K. Hudnut (1998). Poroelastic rebound along the landers 1992 earthquake surface rupture. Journal of Geophysical Research: Solid Earth (1978–2012) 103(B12), 30131–30145.

Perfettini, H. and J.-P. Avouac (2004). Postseismic relaxation driven by brittle creep: A possible mechanism t reconcile geodetic measurements and the decay rate of aftershocks, application to the Chi-Chi earthquake, Taiwan. Journal of Geophys. Res. 109, B02304.

Pollitz, F. F. and I. S. Sacks (1997). The 1995 kobe, japan, earthquake: A long-delayed aftershock of the offshore 1944 tonankai and 1946 nankaido earthquakes. Bulletin of the Seismological Society of America 87(1), 1–10.

Power, W. L. and T. E. Tullis (1991). Euclidean and fractal models for the description of rock surface roughness. Journal of Geophysical Research: Solid Earth (1978–2012) 96(B1), 415–424.

Raleigh, C., J. Healy, and J. Bredehoeft (1976). An experiment in earthquake control at rangely, colorado. Science 191(4233), 1230–1237.

Reasenberg, P. A. and R. W. Simpson (1992). Response of regional seismicity to the static stress change produced by the loma prieta earthquake. Science 255(5052), 1687–1690.

Reiter, D., M. Leidig, S.-H. Yoo, and K. Mayeda (2012). Source characteristics of seismicity associated with underground wastewater disposal: A case study from the 2008 dallas-fort worth earthquake sequence. The Leading Edge 31(12), 1454–1460.

Rice, J. R. (1983a). Constitutive relations for fault slip and earthquake instabilities. PAGEOPH 121.

Rice, J. R, R. A. (1983b). Stability of steady frictional slipping. Journal of Applied Mechanics 50, 343–349.

Richards-Dinger, Keith, B. and H. Dieterich, James (2012). RSQSim earthquake simulator. Seis. Res. Letters 83, 983–990.

Rubinstein, J. L., W. L. Ellsworth, A. McGarr, and H. M. Benz (2014). The 2001–present induced earthquake sequence in the raton basin of northern new mexico and southern colorado. Bulletin of the Seismological Society of America 104(5), 2162–2181.

Ruina, A. (1983). Slip instability and state variable friction laws. Journal of Geophysical Research: Solid Earth 88(B12), 10359–10370.

Ruina, A., L. (1980). Friction laws and instabilities: A quasistatic analysis of some dry friction behavior. Brown University. PhD Dissertation.

Ryan, Kenny, J. and D. Oglesby, David (2014). Dynamic modeling fault step overs using various friction laws. J. Geophys. Res. 119, 5814–5829.

Rymer, M. J., J. A. Treiman, K. J. Kendrick, J. J. Linenkaemper, R. J. Weldon, R. Bilham, M. Wei, E. Fielding, J. L. Hernandez, B. P. E. Olson, P. J. Irvine, N. Knepprath, R. R. Sickler, X. Tong, and M. E. Siem (2011). Triggered surface slips in southern California associated with the 2010 El Mayor-Cucapah, Baja California, Mexico, earthquake, USGS Open-File Report 2010-1333. Technical report.

Sarkarinejad, K. and S. Ansari (2014). The coulomb stress changes and seismicity rate due to the 1990 mw 7.3 rudbar earthquake. Bulletin of the Seismological Society of America.

Savage, J. C. (1983). A dislocation model of strain accumulation and release at a subduction zone. Journal of Geophysical Research: Solid Earth 88(B6), 4984–4996.

Scholz, C. H. and C. Aviles (1986). The fractal geometry of faults and faulting. Earthquake source mechanics 37, 147–155.

Seeber, L., J. G. Armbruster, and W.-Y. Kim (2004). A fluid-injection-triggered earthquake sequence in ashtabula, ohio: Implications for seismogenesis in stable continental regions. Bulletin of the Seismological Society of America 94(1), 76–87.

Segall, P. and S. Lu (2015). Injection-induced seismicity: Poroelastic and earthquake nucleation effects. Journal of Geophysical Research: Solid Earth 120(7), 5082–5103.

Segall, P. and D. Pollard (1980). Mechanics of discontinuous faults. J. geophys. Res 85(38), 4337–4350.

Segou, M. and T. Parsons (2014). The stress shadow problem in physics-based aftershock forecasting: Does incorporation of secondary stress changes help? Geophysical Research Letters 41(11), 3810–3817.

Sevilgen, V., R. S. Stein, and F. F. Pollitz (2012). Stress imparted by the great 2004 sumatra earthquake shut down transforms and activated rifts up to 400 km away in the andaman sea. Proceedings of the National Academy of Sciences 109(38), 15152–15156.

Shapiro, S. and C. Dinske (2009). Fluid-induced seismicity: Pressure diffusion and hydraulic fracturing. Geophysical Prospecting 57(2), 301–310.

Shapiro, S. A., E. Rothert, V. Rath, and J. Rindschwentner (2002). Characterization of fluid transport properties of reservoirs using induced microseismicity. Geophysics 67(1), 212–220.

Sibson, Richard, H. (1986a). RUPTURE INTERACTION WITH FAULT JOGS. Geophysical Monograph Series 37.

Sibson, R. H. (1986b). Rupture interaction with fault jogs. Earthquake Source Mechanics 37, 157–167.

Sieh, K., L. Jones, E. Hauksson, K. Hudnut, D. Eberhart-Phillips, T. Heaton, S. Hough, L. Hutton, H. Kanamori, A. Lilje, S. Lindvall, S. McGill, J. Mori, C. Rubin, J. Spotila, J. Stock, H. Thio, J. Treiman, B. Wernicke, and J. Zachariasen (1993). Near-field investigations of the landers earthquake sequence, april to july 1992. Science 260, 171–176.

Sleep, N. H. (1995). Ductile creep, compaction, and rate and state dependent friction within major fault zones. Journal of Geophysical Research: Solid Earth (1978–2012) 100(B7), 13065–13080.

Stein, R. S. (1999). The role of stress transfer in earthquake occurrence. Nature 402(6762), 605–609.

Stein, R. S., A. A. Barka, and J. H. Dieterich (1997). Progressive failure on the north anatolian fault since 1939 by earthquake stress triggering. Geophysical Journal International 128(3), 594–604.

Stein, R. S., G. C. King, and J. Lin (1994). Stress triggering of the 1994 m= 6.7 northridge, california, earthquake by its predecessors. Science 265(5177), 1432–1435.

Stein, R. S. and M. Lisowski (1983). The 1979 Homestead Valley earthquake sequence, California: Control of aftershocks and postseismic deformations. Journal of Geophys. Res. 88, 6477–6490.

Terzaghi, K. (1925). Principles of soil mechanics, ivsettlement and consolidation of clay. Engineering News-Record 95(3), 874–878.

Toda, S., J. Lin, and R. S. Stein (2011). Using the 2011 m w 9.0 off the pacific coast of tohoku earthquake to test the coulomb stress triggering hypothesis and to calculate faults brought closer to failure. Earth, planets and space 63(7), 725–730.

Toda, S. and S. Matsumura (2006). Spatio-temporal stress states estimated from seismicity rate changes in the Tokai region, central Japan. Tectonophysics 417, 53–68.

Toda, S. and R. Stein (2003). Toggling of seismicity by the 1997 kagoshima earthquake couplet: A demonstration of time-dependent stress transfer. Journal of Geophysical Research: Solid Earth (1978–2012) 108(B12).

Toda, S. and R. S. Stein (2002). Response of the san andreas fault to the 1983 coalinga-nunez earthquakes: An application of interaction-based probabilities for parkfield. Journal of Geophysical Research: Solid Earth (1978–2012) 107(B6), ESE–6.

Toda, S., R. S. Stein, G. C. Beroza, and D. Marsan (2012). Aftershocks halted by static stress shadows. Nature Geoscience 5(6), 410–413.

Toda, S., R. S. Stein, P. A. Reasenberg, J. H. Dieterich, and A. Yoshida (1997). Stress transfered by the 1995 M_w= 6.9 Kobe, Japan, shock: Effect on aftershocks and future earthquake probabilities. USGS: Open File Report.

Toda, S., R. S. Stein, K. B. Richards-Dinger, and S. B. Bozkurt (2005). Forecasting the evolution of seismicity in southern California: Animations built on earthquake stress transfer. Journal of Geophys. Res. 110, B05S16.

Toda, S., R. S. Stein, V. Sevilgen, and J. Lin (2011). Coulomb 3.3 graphic-rich deformation and stress-change software for earthquake, tectonic, and volcano research and teaching - user guide. U.S. Geological Survey Open-File Report 1060, 63.

Tse, S. T. and J. R. Rice (1986). Crustal earthquake instability in relation to the depth variation of frictional slip properties. Journal of Geophysical Research: Solid Earth (1978–2012) 91(B9), 9452–9472.

Tullis, T. E., K. B. Richards-Dinger, J. H. Dieterich, E. H. Field, E. M. Heien, L. H. Kellogg, F. F. Pollitz, J. B. Rundle, D. L. Sachs, D. L. Turcotte, S. N. Ward, and M. B. Yikilmaz (2012). A Comparison among Observations and Earthquake Simulator Results for the allcal2 California Fault Model. Seis. Res. Letters 83.

Wang, H. F. (2000). Theory of Linear Poroelasticity. Princeton University Press.

Weldon, R., T. Fumal, T. Powers, S. Pezzopane, K. Scharer, and J. Hamilton (2002). Structure and earthquake offsets on the San Andreas fault at the Wrightwood, California, paleoseismic site. Bulletin of the Seismological Society of America 92(7), 2704–2725.

Wennerberg, L. and R. V. Sharp (1997). Bulk-friction modeling of afterslip and the modified omori law. Tectonophysics 277(1), 109–136.

Wesnousky, S. (1988). Seismological and structural evolution of strike-slip faults. Nature 335, 340–343.

Wesnousky, S. G. (2006). Predicting the endpoints of earthquake ruptures. Nature 444, 358–360.

Woessner, J., E. Hauksson, S. Wiemer, and S. Neukomm (2004). The 1997 kagoshima (japan) earthquake doublet: A quantitative analysis of aftershock rate changes. Geophysical research letters 31(3).

Wyss, M. and S. Wiemer (2000). Change in the probability for earthquakes in southern california due to the landers magnitude 7.3 earthquake. Science 290(5495), 1334–1338.

Xia, K., A. J. Rosakis, and H. Kanamori (2004). Laboratory earthquakes: The sub-Rayleigh-to-supershear rupture transition. Science 303(5665), 1859–1861.

Yang, W., E. Hauksson, and P. M. Shearer (2012). Computing a large refined catalog of focal mechanisms for southern california (1981–2010): Temporal stability of the style of faulting. Bulletin of the Seismological Society of America 102(3), 1179–1194.

Zoback, M. D. (2007). Reservoir Geomechanics. Cambridge University Press. Cambridge Books Online.

Zoback, M. L. and M. Zoback (1980). State of stress in the conterminous united states. Journal of Geophysical Research: Solid Earth 85(B11), 6113–6156.

Zoback, M. L. and M. D. Zoback (1989). Tectonic stress field of the continental united states. Geological Society of America Memoirs 172, 523–540.